

THE DEVELOPMENT OF MICRO-MECHANICAL MODEL OF KEVLAR FABRICS  
USED IN ENGINE CONTAINMENT SYSTEM OF AIRCRAFTS

by

Saurabh Kumar Bansal

A Thesis Presented in Partial Fulfillment  
of the Requirements for the Degree  
Master of Science

ARIZONA STATE UNIVERSITY

December 2007

THE DEVELOPMENT OF MICRO-MECHANICAL MODEL OF KEVLAR FABRICS  
USED IN ENGINE CONTAINMENT SYSTEM OF AIRCRAFTS

by

Saurabh Kumar Bansal

has been approved

November 2007

Graduate Supervisory Committee:

Subramaniam Rajan, Co-chair

Barzin Mobasher, Co-chair

Hanqing Jiang

ACCEPTED BY THE GRADUATE COLLEGE

## ABSTRACT

Woven fabric wraps are widely used in the propulsion engine containment systems to mitigate the damaging effects from fan blade-out events. Such containment systems are found to be cost-effective mainly because the fabrics have a high strength to weight ratio. This research builds on the constitutive model of Kevlar 49 fabric developed earlier in a variety of ways. First, the continuum model developed in previous research is improved. Multi layer fabric modeling is used that captures the interaction between the fabric layers. The aim is to improve the understanding of failure modes when fabric layer-to-layer interactions are involved during penetrator impact. In addition, a modified failure criteria and contact formulation are employed to obtain more realistic failure modes. The improved constitutive model was validated by LS-DYNA simulations of a suite of NASA Ballistic Tests. The results from these simulations show a closer match with the experimental tests compared to the previous constitutive model. Second, a finite-element based micromechanical model of Kevlar is developed. Micromechanical models are very effective in capturing yarn-yarn interaction and potentially they can be used for virtual testing of fabrics. In this research optical microscopy is used in capturing the geometry of the individual yarns under different strain levels. Using the material data obtained from single yarn quasi-static tensile tests, the constitutive model suitable for use with three-dimensional finite elements is developed. The material model for solid elements was incorporated into the LS-DYNA finite element program through a user defined material definition (subroutine) and was validated by comparing the single yarn and swath test simulations with experimental results.

## ACKNOWLEDGMENTS

I would like to thank my advisors and committee co-chairs, Dr. Subramaniam “Subby” Rajan and Dr. Barzin Mobasher, for giving me the opportunity to work on this project. Their guidance and constant motivation has been the major driving force for me in completing this research work. I am grateful for the comments and suggestions they have made in support of my research. I would also like to thank my committee member Dr. Hanqing Jiang for taking time to serve on my committee. I greatly appreciate the help provided by Dr. Dallas Kingsbury, Peter Goguen and Jeff Long in day to day laboratory work and Center for Solid State Science (CSSS) at Arizona State University for sharing their expertise in the area of Optical Microscopy. I would also like to thank my family and friends for their constant support and motivation. I am appreciative of Dr. Jeff Simons (SRI International) and Ion Vintilescu (Honeywell Engines) for sharing their knowledge and experience with LS-DYNA. I would also like to thank other members of the research team which include members from Honeywell and NASA-GRC for their technical insight and experimental contributions. Last but not least, I would like to thank Don Altobelli and Bill Emmerling of the Federal Aviation Administration for providing funding for this research.

## TABLE OF CONTENTS

	Page
LIST OF TABLES .....	IX
LIST OF FIGURES .....	XI
CHAPTER	
1. INTRODUCTION .....	1
1.1. Motivation for Research and Overview .....	1
1.2. Literature Review.....	4
1.2.1. Modeling Techniques for Fabrics and Fabric Composites .....	5
1.2.2. Experimental Procedures .....	11
1.2.3. Quasi-Static Simulations using Explicit Finite Element Code .....	14
1.3. Thesis Objectives .....	16
1.4. Thesis Overview .....	16
2. THEORETICAL BACKGROUND.....	18
2.1. Overview of Explicit Finite Element Analysis .....	18
2.2. General Solution and Algorithm for Explicit Analysis.....	22
2.3. Quasi-static simulations using Explicit Finite Element Analysis .....	26
3. KEVLAR GEOMETRY AND SINGLE YARN TENSILE TESTS .....	29
3.1. Introduction.....	29
3.2. Kevlar Geometry Computation.....	30
3.2.1. Sample Preparation .....	31
3.2.2. Vacuum Impregnation .....	33
3.2.3. Cutting and Polishing.....	33

CHAPTER	Page
3.2.4. Optical Microscopy.....	36
3.2.5. Image Analysis.....	39
3.2.6. Results and Discussion .....	44
3.3. Kevlar Single Yarn Tensile Tests .....	69
3.3.1. Specimen preparation and fixture details.....	69
3.3.2. Specimen Test Procedure.....	70
3.3.3. Results and Discussion .....	72
3.3.4. Weibull Analysis.....	81
4. MICRO-MECHANICAL MODEL OF KEVLAR.....	85
4.1. INTRODUCTION .....	<b>Error! Bookmark not defined.</b>
4.2. GEOMETRIC MODEL.....	85
4.2.1. Unit Cell Development .....	85
4.2.2. Swatch Model Generation.....	87
4.3. MATERIAL MODEL DESCRIPTION.....	88
4.3.1. Kevlar Yarn Constitutive Behavior .....	88
4.3.2. Determination of $E_{11}$ .....	90
4.3.3. Determination of other material properties.....	101
4.4. Verification of Micro-mechanical model.....	101
4.4.1. Single Yarn Simulations .....	101
4.4.2. Swath Tensile Test Simulations.....	107
5. CONTINUUM MODEL.....	115
5.1. Introduction.....	115

CHAPTER	Page
5.2. ASU Continuum Model .....	115
5.2.1. Improvements in Current Continuum Model.....	115
5.2.2. Analysis Parameters.....	120
5.2.3. Q A check for simulation.....	124
5.3. Single FE layer ballistic test simulations .....	126
5.3.1. Finite Element Model .....	126
5.3.2. Results and Discussion .....	127
5.3.3. Q A Check.....	131
5.3.4. Regression Model .....	133
5.3.5. Sensitivity Analysis .....	135
5.4. Multi FE layer ballistic test simulation.....	143
5.4.1. Finite Element Model .....	143
5.4.2. Results and Discussion .....	144
5.4.3. Q A Check.....	146
5.4.4. Regression Model .....	148
5.4.5. Sensitivity Analysis .....	150
6. CONCLUDING REMARKS AND FUTURE WORK .....	158
6.1. Conclusion .....	158
6.1.1. Micro-mechanical Model.....	158
6.1.2. Continuum Model.....	159
6.2. Future Work.....	161
REFERENCES .....	162

CHAPTER	Page
APPENDIX	
A.....	167
B.....	169



## LIST OF TABLES

Table	Page
3.1. Fill direction ellipse curve parameters.....	47
3.2. Fill direction sine curve parameters.....	54
3.3. Warp direction Elliptical curve parameters .....	60
3.4. Warp direction Sine curve parameters.....	66
3.5: Single yarn test plan.....	72
3.6: Single yarn test results .....	77
3.7: Single yarn test results .....	77
3.8: Single yarn test data.....	83
3.9: Weibull parameters .....	83
4.1: Geometry Parameters.....	86
4.2: Modified geometry parameters .....	87
4.3: Mesh Study – Single Yarn Simulations.....	103
4.4: Mass Scaling Study – Swatch Test Simulations.....	<b>Error! Bookmark not defined.</b>
5.1: Description of important control parameters used in Single layer and Multilayer model developed at ASU .....	123
5.2: Energy ratios and values used for QA check of simulations .....	126
5.3: Absorbed energy of fabric for experimental ballistic tests and simulations.....	128
5. 4: Statistics for absorbed energy % difference between simulations and experiments .....	129
5.5: Statistics for absorbed energy % difference between simulations and experiments for test cases LG433, LG434, LG444 and LG449 .....	130

Table	Page
5.6 Statistics for absorbed energy % difference between simulations and experiments after removal of test cases LG433, LG434, LG444 and LG449.....	130
5.7 QA check of single FE layer models .....	132
5.8 Variables used in regression analysis .....	133
5.9: Absorbed energy of fabric for experimental ballistic tests and simulations.....	145
5.10 Statistics for absorbed energy difference between simulations and experiments...	146
5.11 QA check of multi FE layer models .....	147
5.12 Variables used in regression analysis .....	148
A.1. Kevlar® 49 material constants used in material model .....	168

## LIST OF FIGURES

Figure	Page
1.1. Kevlar® 49 sample .....	2
1.2. Propulsion engine with containment system [courtesy, Honeywell Engines, Phoenix, AZ].....	3
1.3. (a) Weave architecture (b) RVE (c) quarter of the RVE .....	7
1.4. Division of quarter RVE into subcells using the four-cell method.....	8
1.5. Example of FE mesh of a plain woven fabric unit cell.....	9
1.6. Photomicrograph image of a fabric similar to Kevlar in cross section.....	10
1.7. Free body diagram of single fiber under compression load.....	11
1.8. Experimental set up of pendulum test on single fiber.....	12
2.1. Time increments using the central difference method.....	22
2.2. Schematic diagram showing three elements in a 2-D mesh .....	27
3.1. Micromechanical FE model of Kevlar® 49.....	29
3.2. Schematic of overall experimental procedure.....	30
3.3. Stress Strain curve of Kevlar during test .....	32
3.4. Sample held under constant strain level.....	32
3.5. Vacuum Apparatus.....	33
3.6. Polishing equipment.....	35
3.7. Finished Kevlar Samples .....	35
3.8. Optical Microscopy equipment.....	36
3.9 (a). Fill yarn longitudinal cross-section – undeformed geometry.....	37
3.9 (b). Fill yarn longitudinal cross-section under 1.0% Strain level .....	37

Figure	Page
3.9 (c). Fill yarn longitudinal cross-section under 1.5% Strain level .....	37
3.9 (d). Fill yarn longitudinal cross-section under 2.0% Strain level .....	37
3.11 (a). Warp yarn longitudinal cross-section – undeformed geometry .....	38
3.11 (b). Warp yarn longitudinal cross-section under 1.0% Strain level.....	38
3.11 (c). Warp yarn longitudinal cross-section under 1.5% Strain level .....	38
3.11 (d). Warp yarn longitudinal cross-section under 2.0% Strain level.....	38
3.12. Sin curve parameter estimation.....	40
3.13. curve fit through point cloud.....	41
3.14. Cross section approximation using ellipse.....	42
3.15: Ellipse fit through point cloud .....	43
3.16. Cross section approximation using step function .....	44
3.17. Fill cross-section (undeformed) ellipse curve fit through point cloud.....	45
3.18. Fill cross-section (1.0 % Strain) ellipse curve fit through point cloud .....	45
3.19. Fill cross-section (1.5 % Strain) ellipse curve fit through point cloud .....	46
3.20. Fill cross-section (2.0 % Strain) ellipse curve fit through point cloud .....	46
3.21. Comparison of Fill cross-section (ellipse) at different strain levels .....	48
3.22. Comparison of Fill cross-section (ellipse) at different strain levels .....	49
3.23. Comparison of Fill cross-section (ellipse) at different strain levels .....	50
3.24. Fill cross-section (undeformed) sin curve fit through point cloud .....	51
3.25. Fill cross-section (1.0% strain level) sin curve fit through point cloud.....	52
3.26. Fill cross-section (1.5% strain level) sin curve fit through point cloud.....	52
3.27. Fill cross-section (2.0% strain level) sin curve fit through point cloud.....	53

Figure	Page
3.28. Comparison of Fill cross-section (sine curve) at different strain levels .....	55
3.29. Comparison of Fill cross-section (sine curve) at different strain levels .....	56
3.30. Comparison of Fill cross-section (sine curve) at different strain levels .....	56
3.31. Warp cross-section (undeformed) ellipse fit through point cloud .....	57
3.32. Warp cross-section (1.0% strain) ellipse fit through point cloud .....	58
3.33. Warp cross-section (1.5% strain) ellipse fit through point cloud .....	58
3.34. Warp cross-section (2.0% strain) ellipse fit through point cloud .....	59
3.35. Comparison of Warp cross-section (ellipse) at different strain levels.....	61
3.36. Comparison of Warp cross-section (ellipse) at different strain levels.....	62
3.37. Comparison of Warp cross-section (ellipse) at different strain levels.....	62
3.38. Warp cross-section (undeformed) sin curve fit through point cloud .....	64
3.39. Warp cross-section (undeformed) sin curve fit through point cloud .....	65
3.40. Warp cross-section (undeformed) sin curve fit through point cloud .....	65
3.41. Comparison of Fill cross-section (ellipse) at different strain levels .....	67
3.42. Comparison of Fill cross-section (ellipse) at different strain levels .....	68
3.43. Single yarn test setup .....	70
3.44. Single yarn tensile test .....	71
3.45. Stress Strain curves for G.L. = 2 in.....	73
3.46. Stress Strain curves for G.L. = 5 in.....	74
3.47. Stress Strain curves for G.L. = 8 in.....	74
3.48. Stress Strain curves for G.L. = 11 in.....	75
3.49. Stress Strain curves for G.L. = 14 in.....	76

Figure	Page
3.50. Stress Strain curves for G.L. = 17 in.....	76
3.51. Peak Stress vs gauge length.....	78
3.52. Peak Stress vs gauge length.....	79
3.53. Young’s Modulus vs gauge length .....	80
3.54. Strain at peak stress vs gauge length.....	80
3.55. Comparison of cumulative failure probability vs peak stress for different gage lengths.....	84
4.1. Unit cell Model .....	86
4.2. Swatch Model .....	88
4.3. Stress vs strain curves of single yarn tensile tests for different gage lengths .....	91
4.4. Kevlar warp yarn experimental stress-strain curves with linear approximation.....	92
4.5. Kevlar® 49 yarn uniaxial stress-strain results with approximation for pre-peak and post-peak behavior .....	94
4.6. Strain rate effect on the stress-strain behavior of Kevlar® 49 yarns from Wang and Xia.....	96
4.7. Normalized peak stress as a function of strain rate for material strain rate model and experimental results .....	99
4.8. Strain rate effects on the yarn model .....	100
4.9. Single Yarn model .....	102
4.10. Mesh density effect on single yarn simulation .....	105
4.11. Preliminary single yarn simulation results.....	114
5.1. Fabric sample at end of warp direction tension test.....	116

Figure	Page
5.2. Kevlar® 49 warp (11) direction uniaxial stress-strain results with approximation for pre-peak and post-peak behavior .....	117
5.3. Kevlar® 49 fill (22) direction uniaxial stress-strain results with approximation for pre-peak and post-peak behavior .....	118
5.4. Kevlar® 49 warp (11) direction load curves used in ASU material model v1.0 and v1.1.....	119
5.5. Kevlar® 49 warp (11) direction load curves used in ASU material model v1.0 and v1.1.....	120
5.6. Comparison of Experimental and Simulation orientation for LG432 .....	124
5.7. Comparison of Experimental and Simulation orientation for LG449 .....	125
5.8. Single FE layer ballistic test model .....	127
5.10. Sensitivity of material model to $E_{11}$ .....	136
5.11. Sensitivity of material model to $E_{22}$ .....	136
5.12. Sensitivity of material model to $G_{12}$ .....	137
5.13. Sensitivity of material model to the coefficient of friction.....	138
5.14. Sensitivity of material model to failure strain.....	139
5.15. Sensitivity of material model to $G_{23}$ and $G_{31}$ .....	140
5.16. Multi FE layer ballistic test model.....	144
5.18. Sensitivity of material model to $E_{22}$ .....	151
5.19. Sensitivity of material model to $G_{12}$ .....	152
5.20. Sensitivity of material model to the coefficient of friction.....	153
5.21. Sensitivity of material model to the coefficient of friction.....	153

Figure	Page
5.22. Sensitivity of material model to the fail strain.....	154
5.23. Sensitivity of material model to G23 and G31 .....	155
B.1. Flow diagram for UMAT subroutine .....	170



# 1. INTRODUCTION

## 1.1. Motivation for Research and Overview

Woven fabric wraps are widely used in the propulsion engine containment systems that are designed to mitigate the effects from a fan blade-out event which occurs when fracture of a fan uses fan blades or portions of the fan blades to be ejected from the rotor. The containment system is designed so that the fan blade fragments do not cause any additional damage to the fuselage which would compromise the pilot's ability to safely navigate the aircraft. Such systems are found to be cost-effective for mitigating full structural and hydraulic failures engine debris during fan blade-out event. This is mostly because of its high strength per unit weight property no containment ability. Moreover it is more economical to manufacture such a containment system compared with the traditional metallic systems. To properly utilize this advantage, it is necessary to have a robust predictive tool based on fundamental characterization of response using finite element analysis modeling methodology for design tasks. A robust analysis methodology is also necessary for numerical design optimization and process automation.

Currently Kevlar<sup>®</sup>49 is the only woven fabric that has been approved by the Federal Aviation Administration (FAA) for use in engine containment systems. Kevlar was the first?? Most successful organic fibers with sufficient tensile strength and modulus to be used in advanced composites. Kevlar is an aramid, a term invented as an abbreviation for aromatic polyamide. The chemical composition of Kevlar is poly para-phenyleneterephthalamide, and it is more properly known as a para-aramid. Aramids belong to the family of nylons. Like nylons, Kevlar filaments are made by extruding the

precursor through a spinneret. The rod form of the para-aramid molecules and the extrusion process make Kevlar fibers anisotropic – they are stronger and stiffer in the axial direction than in the transverse direction.

A sample of Kevlar 49<sup>®</sup> fabric is shown in Figure 1.1. The longitudinal direction of the fabric is referred as the warp direction and direction perpendicular to the warp direction is referred as the fill direction. Each yarn of fabric consists of hundreds of single filaments. Kevlar 49<sup>®</sup> fabric tested in this program has 17 yarns per inch in both fill and warp direction.

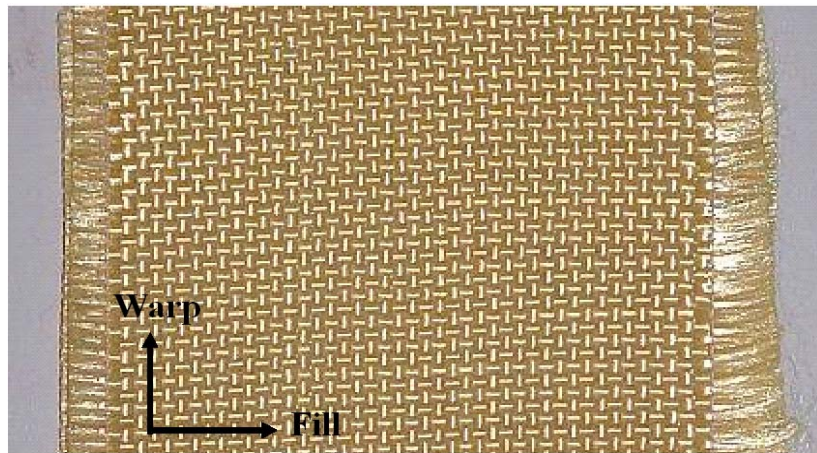


Figure 1.1. Kevlar<sup>®</sup> 49 sample

Figure 1.2 shows a typical propulsion engine with Kevlar<sup>®</sup>49 wrapped around a thin aluminum encasement covering rotor. The fabric is then covered with a protective layer.

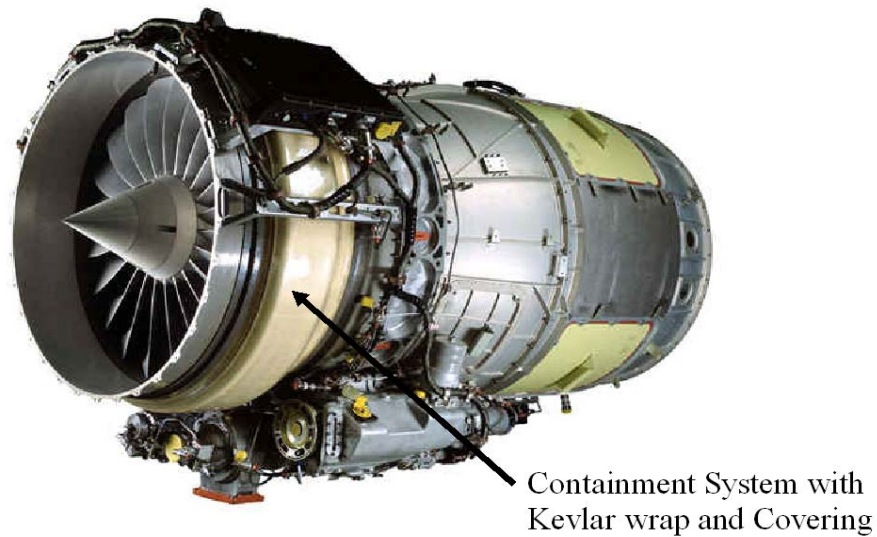


Figure 1.2. Propulsion engine with containment system [courtesy, Honeywell Engines, Phoenix, AZ]

Designing of the containment system consists of determining the number of fabric layers and fabric width required to successfully contain the debris of blade within the engine. Currently the FAA's design standards require that at least a single successful full scale test of fan blade out, in addition to bird ingestion tests certain number of experimental tests (Not really) must be completed to determine these design variables. The tests include projecting certain objects (bird) into a running engine that cause a fan blade-out event, (no explosive charges.) go to youtube and "type fan blade out" . If all fan blade fragments are contained by the fabric then the containment system is determined to be acceptable for the containment system. These tests are very expensive so the ability to perform numerical simulations of the experimental tests to either reduce or eliminate the

number of experimental tests required is attractive to the FAA and engine manufacturers. With today's advanced numerical techniques modeling a propulsion engine and simulating a fan blade-out event can be accomplished using finite elements and explicit finite element analysis. There are proven constitutive models which can simulate the behavior of most of the materials which compose a propulsion engine and containment system. The difficulty lies in fact that there is no publicly available mechanistic based constitutive model for Kevlar<sup>®</sup>49, or essentially any woven fabric, especially one that can be used to predict the fabric's behavior when subjected to impact loads. In previous research at Arizona State University (ASU), continuum model had been developed for Kevlar fabric. However, it was used only with single FE layer. Overall this model did quite well in predicting energy absorption in ballistic test but results for some of the test cases were not accurate. Being a continuum model it also carried inherent drawbacks of not able to simulate yarn to yarn interaction. So, although friction between yarns is considered to be very important parameter it was not considered in the continuum model. The primary focus of this research is to develop micromechanical model of the Kevlar fabric which can capture frictional effect between yarns and accurately predict Kevlar swatch behavior under various loading condition, improve current material model to get more consistent results and build multi FE layer model which can capture effect of friction between the fabric layers.

## 1.2. Literature Review

In recent years, many efforts have been given to the estimation of effective material properties of fabric composites and fabrics used as structural element. The approaches developed include the homogenization method, the finite element method, analytical model and experimental approach. The research outlined in this section deals with various analytical and numerical methods implemented to capture the behavior of the fabrics and fabric composites, experimental procedures to ascertain the properties of single yarn and quasi-static simulation using non-linear, explicit finite element code.

#### 1.2.1. Modeling Techniques for Fabrics and Fabric Composites

In the recent research at Arizona State University [Zack last name, 2007], continuum model of Kevlar fabric has been developed. Continuum models typically allow greater computational efficiency and are easily integrated into multi-component system models. However, the continuum models do not account for the effect of interactions between the yarn families. These interactions include 1) crimp interchange, a mechanism by which the fabric elongates along the direction of one yarn family with negligible yarn stretching, as the yarns of that family become less crimped (i.e. the yarn waves decrease in amplitude and increase in wavelength), while the fabric contracts along the direction of the other yarn family what do you mean family?, as the yarns of that family become more crimped; 2) locking, a mechanism by which the fabric resists deformations as the interwoven yarns jam against each other and 3) resistance to relative yarn rotation, which is the dominant mechanism for the response of fabric to inplane shear. These are important behaviors in many fabric applications. The omission of

potentially important behaviors makes traditional continuum models unsuitable for the general analysis of novel fabric systems where both the macroscopic behavior at the continuum level and the yarn interactions at the mesostructural level may be important.

Although creating finite element models of dry fabrics that include yarn geometry details (meso-scale) for use in the analysis of ballistic events may not be practical however, this model can be very useful in determining the fabric behavior under different loading conditions which in turn can be used to determine continuum properties. The difficulty in developing a model to simulate the effective properties lies in (1) determining accurately the yarn geometry in the fabric, and (2) simulating the yarn-yarn interaction and the yarn-matrix interaction (for composites). More recently very accurate descriptions of the yarn geometry have been made through the use of photomicrographs or scanning electron microscope (SEM) images. In the absence of these high resolution images, researchers have made reasonable assumptions for the fabric geometry. Currently there are several approaches being used in computing the effective properties - the Method of cells (MOC), variations of the MOC, finite element modeling with virtual testing, and classical lamination theory. With each method only a representative unit of material is considered due to the repetitive pattern in the composite material. The terms “representative unit cell (RUC)”, “unit cell”, or “representative volume element (RVE)” will be used interchangeably. An example of a repetitive unit cell for a plain weave fabric [Tabiei and Yi, 2002] is shown in Figure 1.3. Symmetric conditions are used to improve the computational efficiency - one quarter of the unit cell model is shown in the same figure.

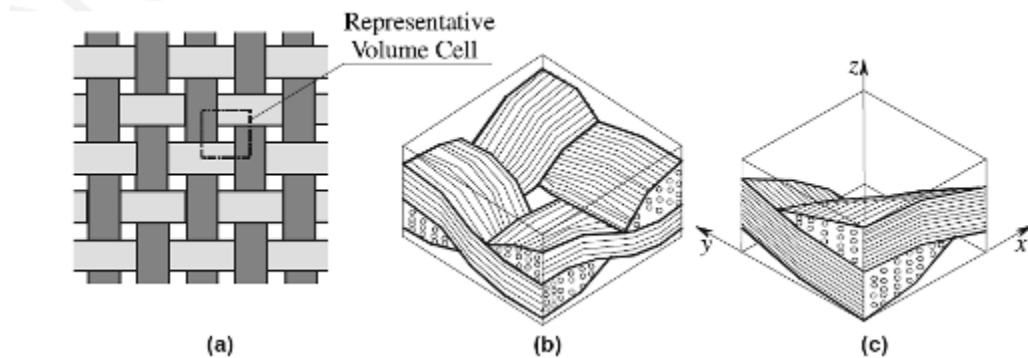


Figure 1.3. (a) Weave architecture (b) RVE (c) quarter of the RVE

Analytical methods including classical laminate theory (CLT) and MOC have been successful in determining effective material properties. Some of the earliest CLT models have been used to determine the elastic modulus of woven fabric composites [Ishikawa and Chou, 1982-1983; Ishikawa et al., 1985]. One of the more recent CLT models referred to as Mesotex [Scida et al., 1999] is general enough to capture the 3D elastic properties and the ultimate failure strengths of several types of fabric composites and is very computationally efficient. Models using the method of cells that have shown good correlation with experimental results [Jiang and Tabiei, 2000; Tabiei and Jiang, 1999; Tanov and Tabiei, 2001]. One of the approaches used is referred to as a four-cell model where the quarter cell RVE is divided into four subcells as shown in Figure 1.4 [Tabiei and Yi, 2002].

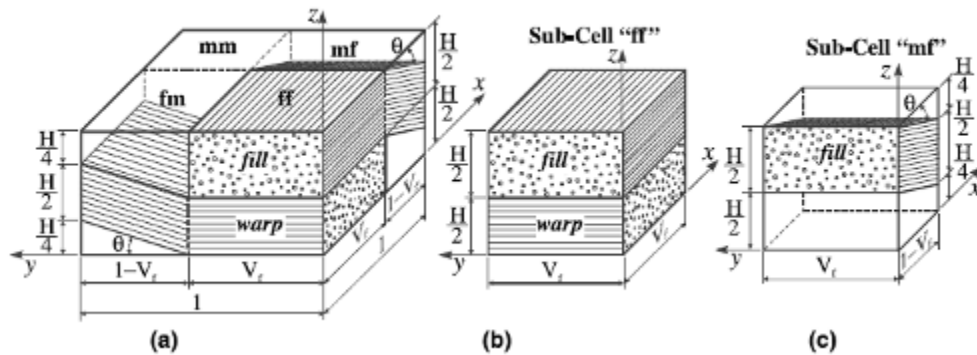


Figure 1.4. Division of quarter RVE into subcells using the four-cell method

Using four subcells allows the model to be computationally efficient compared to its similar counterparts. In these MOC models, iso-strain and iso-stress conditions are assumed and the constitutive equations are averaged through the thickness of the RVE. The unit cell is then divided into many subcells and an averaging procedure is then performed again by assuming uniform state of stress in the subcells. The stress-strain relations of each subcell can then be obtained and related to the effective stress-strain behavior of the unit cell. Tabiei and Yi [Tabiei and Yi, 2002] developed a simplified method of cells model and compared it to previously developed method of cells models, the four-cell model, and finite element solutions. They concluded that their simplified method could be used as a fast tool for predicting the material properties of fabric composites but they recommended the four-cell model for most structural analysis problems. Another model utilizing the method of cells technique was developed by Naik and Ganesh [Naik and Ganesh, 1996] and showed good correlation with experimental results. Vandeurzen and co-workers [Vandeurzen et al., 1996] developed what they refer



to as a combi-cell model where the complementary variational principle was used to obtain the stiffness matrix of the unit cell.

Another method for determining the effective material properties of the unit cell is through numerical, or finite element solutions. Typically this procedure involves modeling the actual yarn and matrix geometry of the unit cell with many elements. Then virtual tests are conducted by varying the loading and boundary conditions on the unit cell and the results are used to establish the effective material properties. An example of a finite element mesh of a woven fabric unit cell is shown in Figure 1.5 taken from [Peng and Chao, 2000].

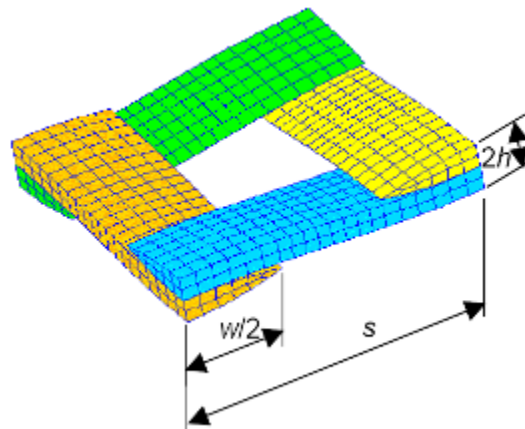


Figure 1.5. Example of FE mesh of a plain woven fabric unit cell

Using finite elements is more computationally expensive compared to using closed form methods. However it provides detailed stress-strain distributions. The most challenging aspect of this technique is obtaining the appropriate weave architecture of the fabric. Using high resolution images such as photomicrograph or SEM images provides a microscopic view of the yarn geometry. Researchers have been able to fit mathematical functions to these images to accurately model the weave pattern in three dimensions. An

example of a photomicrograph image of a fabric similar to Kevlar is shown in Figure 1.6 [Barbero et al., 2006].

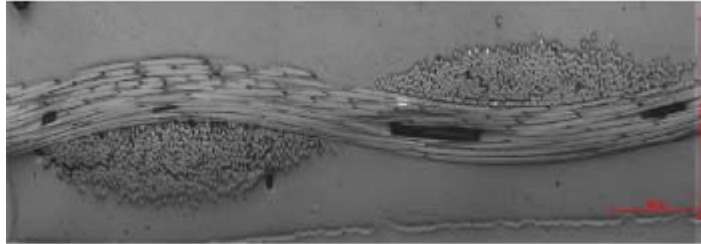


Figure 1.6. Photomicrograph image of a fabric similar to Kevlar in cross section [put the reference in here as well]

Barbero and co-workers create a 2D model of the RVE geometry by fitting a sinusoidal curve to the image. To create a 3D model, the researchers used the 2D fit along with the capabilities of an advanced commercial modeling program. The yarns were modeled with transversely isotropic solid elements and the effective elastic material constants were obtained by varying the boundary conditions and loading on the unit cell. The researchers reported good correlation with experimental values and values predicted from analytical methods. Peng and Chao [Peng and Chao, 2000] used a similar approach by conducting virtual tests on a finite element model of the unit cell. However, they went one step further by taking into account the non-linearity of the material and fitting the results to a shell element equal in size to the unit cell. They developed equations for the elastic modulus, shear modulus, and Poisson ratio as a function of strain. Sriregan and co-workers [Sriregan et al., 1997] proposed a global/local method that required two stages. First a macroscopic finite element model using a small number of elements and homogenized material properties is created. The results from the global analysis are then

used in a more detailed local analysis where a finite element model taking into account the weave geometry is used.

### 1.2.2. Experimental Procedures

The challenges in building the micro-mechanical model of Kevlar fabric is two folds. First, there is difficulty in obtaining Kevlar yarn geometry in the form which can be used to model 3-D geometry using modeling packages accurately. Second, it is difficult to ascertain all material properties at yarn level. Shockey and co workers [Shockey et al., 1999] and Vezemnieks J [Vezemnieks J, 2003] conducted single yarn tensile tests on Zylon yarns. There is very less literature available to compute other material properties of single yarn like shear modulus and poisson's ratio. One of the successful tests conducted to compute other parameters are explained by Cheng and co workers [Cheng et al., 2004]. Cheng computed tensile properties, shear properties and poisson's ratios for single fiber of Kevlar. The tensile properties of the single yarn are computed using Split Hopkinson's Tensile Bar (SHTB). To compute the poisson's ratio of Kevlar fiber a transverse load was applied as shown in Figure 1.7 while longitudinal load and deflection was constantly recorded.

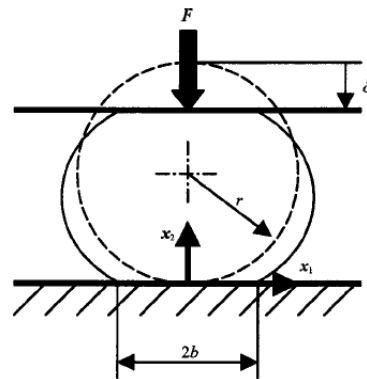


Figure 1.7. Free body diagram of single fiber under compression load

The shear modulus of the fiber was computed using torsion pendulum setup as shown in Figure 1.8. The shear modulus of the fiber is defined as

$$G_{13} = \frac{\pi M [8(D_o^2 - D_i^2) + \frac{32}{3} h^2] l f^2}{d^4} \quad (1.1)$$

where  $M$  is the mass of the washer,  $D_o$  and  $D_i$  are the outer and inner diameters of the washer, respectively,  $h$  is the thickness of the washer,  $l$  is the length of the fiber,  $f$  is the oscillation frequency of the torsional pendulum, and  $d$  is the diameter of the fiber.

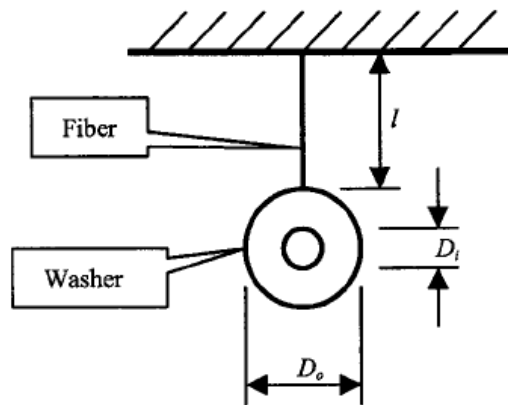


Figure 1.8. Experimental set up of pendulum test on single fiber

There is no known data is available for single yarn shear properties and poisson's ratios. [Duan and co workers, 2205] modeled Zylon fibers based on [Shockey et al., 1999] experimental data and by extending the experimental results by approximating shear and poisson's ratios. Duan considered the principle axis tensile modulus as computed by Shockey and out of plan tensile modulus were considered lower then principle axis tensile modulus by a factor of 50. Similarly the shear moduli were

approximated to out of plan tensile modulus. The poisson's effect was not considered for the simulations.

Other material parameter which is of interest is the strain rate dependence of Kevlar yarn tensile strength. One of the more successful techniques for conducting experimental strain rate testing is the Split Hopkinson bar (SHB) test. Wang and Xia [Wang and Xia, 1998, 1999] conducted strain rate tests on Kevlar<sup>®</sup> 49 yarns using the SHB test up to  $1350 \text{ s}^{-1}$  and found that the fabric had both temperature and rate dependence. The yarn's elastic modulus, peak stress, strain to peak stress, and failure strain each increased with an increase in strain rate. The same properties were shown to decrease with an increase in temperature as well. After conducting strain rate tests on Kevlar<sup>®</sup> KM2 yarns using the SHB, Cheng and co-workers [Cheng et al., 2005] concluded that the yarns were not rate dependent up to a strain rate of approximately  $2450 \text{ s}^{-1}$ . Rodriguez et al. [Rodrigues et al., 1996] conducted strain rate tests using the SHB on aramid and polyethylene fabrics up to a strain rate of about  $1000 \text{ s}^{-1}$ . They observed that both types of fabrics were rate sensitive with an increase in peak stress and a decrease in failure strain as the strain rate increased. Shim et al. [Shim et al., 2001] conducted strain rate tests using the SHB on Twaron<sup>®</sup> fabric up to a rate of approximately  $500 \text{ s}^{-1}$ . The authors observed that Twaron<sup>®</sup> fabric was very sensitive to loading rate with significant increases in the elastic modulus and peak stress values and a large decrease in the failure strain with an increase in strain rate. It should be noted that the test results are one of the few published where fabric samples not yarns are used in the test. The samples

were 5 mm wide with a 30 mm gauge length. The authors noted that Twaron<sup>®</sup> fabric is very similar to Kevlar<sup>®</sup>29 in both microstructure and mechanical properties.

### 1.2.3. Quasi-Static Simulations using Explicit Finite Element Code

Simulation of Quasi-static process using explicit finite element method often results in very large simulation time. This is due to the fact that the dynamic explicit method is conditionally stable. The stability limit for the explicit integration operator is that the maximum time increment must be less than a critical value of the smallest transition times for a dilatational wave to cross any element in the mesh. Thus this approach needs a very small time increment to do so and it leads to a huge amount of computational time. Therefore, to solve quasi-static problems, it is conventional to convert the real problem to a virtual problem with a different mass density and processing time by means of mass and time scaling.

Many researchers have studied the effect of mass and time scaling on the stability and inertial effect in quasi-static tests. Santosa and co workers [Santosa et al., 2000] have applied mass and time scaling technique to simulate analysis of foam filled sections. In order to reduce the total simulation time they have increased the velocity by a factor of 2000. The inertial effects in these simulations were minimized by using ramp function for the velocity and reducing density by appropriate factor. Further, to check if the simulation is quasi-static in nature, two checks were suggested. First, the total kinetic energy has to be very small compared to the total internal energy over the period of the

simulation. Secondly, the force-displacement response must be independent from the applied velocity.

Kim and co workers [Kim et al., 2002, 2003] compared the results from implicit and explicit finite element method to simulate the quasi-static hydro forming process. They utilized both time scaling and mass scaling to reduce the simulation time. In order to find a suitable scale factor, Belytschko and coworkers [Belytschko, 1997] suggested an energy error estimate which can identify if the dynamic effects are significant. This error criterion  $e(t)$  for dynamic effects can be expressed simply by the ratio of the change of kinetic energy to the plastic work as follows:

$$e(t) = \frac{1}{W_{\text{int}}^{\text{plastic}}(t)} \int_0^t \int_{\Omega} dE_k = \frac{E_k(t) - E_k(t_y)}{W_{\text{int}}^{\text{plastic}}(t)} \quad (1.2)$$

where  $W$  is a plastic internal energy and  $E_k$  is a kinetic energy.  $t_y$  is the time when the plastic deformation is being started. Thus, this criterion accounts for the ratio of the kinetic energy to the internal work and accounts for the transfer between the kinetic energy and the internal work, which is a measure of the deviation of the dynamic solution from the static solution. In order to identify good simulation case Kim used this criteria. They further suggested that the kinetic energy must be less than 10% of the internal strain energy, when searching for a suitable scaling factor.

### 1.3. Thesis Objectives

The objectives of this research are as follows:

- (1) To capture the geometry of Kevlar<sup>®</sup>49 fabric under different strain levels and build 3-D model of the fabric using 2-D images taken using Optical Microscopy.
- (2) Perform laboratory tests to ascertain tensile properties of Kevlar<sup>®</sup>49 single yarn and build constitutive material model.
- (3) Develop micro-mechanical model of the Kevlar<sup>®</sup>49 using 3-D model developed in (1) and constitutive model developed in (2).
- (4) To validate the material model using Single yarn and swath tensile tests conducted at ASU.
- (5) Improve current continuum material model developed at ASU and build multi FE layer model to simulate ballistic tests conducted at NASA-GRC.

### 1.4. Thesis Overview

Chapter 2 of this thesis describes the theory behind explicit finite element analysis, the standard method of numerical analysis for simulating the behavior of structures during ballistic events and use of mass and time scaling for quasi-static simulation using explicit finite element analysis. Chapter 3 explains the experimental part of this study which essentially includes the procedure used to capture Kevlar<sup>®</sup>49 geometry under different strain levels and single yarn tensile tests conducted at ASU. This chapter forms the basis of micromechanical modeling as geometric parameters



discussed in chapter used for solid modeling of the Kevlar fabric and single yarn tensile test data is used as material properties of the yarns. Geometric model along with material properties are combined to build micromechanical model of the fabric which is discussed in detail in chapter 4. Chapter 4 explains in detail about UMAT modeling in LS-DYNA and various material properties used to build constitutive relation of Kevlar yarn. The material model is validated using Kevlar single yarn and swatch tensile test simulations. Chapter 5 discusses the continuum model for the Kevlar<sup>®</sup>49 fabric and multi layer modeling approach developed. General discussions of the material model, validation of the results, and future improvements that can be made are presented in Chapter 6.

## 2. THEORETICAL BACKGROUND

### 2.1. Overview of Explicit Finite Element Analysis

The type of solution technique used to analyze the problem depends on the type of phenomena that is of interest in the study. Structures and solids problems can be categorized into two classes – those for which the stress wave propagation is of engineering importance and those for which the duration of the load is large relative to the time required for a wave to propagate through the structure. Both types of problems are governed by the same set of physical equations but have solutions obtained using different numerical techniques. The first type of problem, also known as transient analysis (explicit dynamics), uses a solution technique which is described as explicit time integration where differential equations are solved explicitly in time. The second type of problem, also known as static analysis, uses a solution technique which is described as implicit integration where differential equations are solved implicitly in time. In general, explicit integration refers to the solution at any step,  $N^{t+\Delta t}$  being solved by using information from the previous step's solution,  $N$  whereas implicit integration refers to the solution at any step,  $N^{t+\Delta t}$  being obtained by solving a system of equations and iterating many times within that step [Zack, 2005].

Some of the advantages of an explicit technique over an implicit technique are as follows.

- (1) Explicit technique is suitable for modeling brief, transient dynamic events, such as impact and blast problems, and is also very efficient for highly nonlinear problems involving changing contact conditions, such as forming simulations

[ABAQUS, 2006]. Material degradation and failure often lead to severe convergence difficulties in implicit analysis programs (because the material stiffness can become negative) but can be solved by explicit technique.

(2) Relatively, much fewer computations and computer memory storage are required per time step since the system equations are not stored, assembled and solved.

(3) The algorithm is simple. For example, the most striking feature of the explicit method is the lack of a global tangent stiffness matrix, which is required with implicit methods. Since the state of the model is advanced explicitly, iterations and tolerances are not required [ABAQUS, 2006].

The only disadvantage is to the explicit technique is that the solution is only conditionally stable. The time step must often be very small to ensure stability and the total number of time steps may be many to obtain the solution. The stability of the explicit integration procedure is dependent on the highest eigenvalue of the system [ABAQUS, 2006]. For an undamped system, the stable time step is determined by

$$\Delta t = \frac{2}{\omega_{\max}} \quad (2.1)$$

where  $\omega_{\max}$  is the highest frequency of the system. With damping the stable time step is determined by

$$\Delta t = \frac{2}{\omega_{\max}} \sqrt{1 + \xi^2} - \xi \quad (2.2)$$

where  $\xi$  is the fraction of critical damping in the highest mode. In finite elements the stability equation expressed in (2.1) can be rewritten as

$$\Delta t = \min \left( \frac{L_{(e)}}{c_d} \right) \quad (2.3)$$

where  $L_{(e)}$  is the characteristic element dimension and  $c_d$  is the dilatational wave speed of the material. The critical time step is the equivalent to the smallest value of time for the dilatational wave to travel through an element. The characteristic element length is a function of the element type and element dimensions and the dilatational wave speed is a function of the material properties [ABAQUS, 2006].

The governing equations for explicit finite element analysis are the equivalent to those used for all non-linear finite element problems [Belytschko and Hughes, 1983]:

- (1) Conservation of mass.
- (2) Conservation of energy.
- (3) Conservation of momentum.
- (4) A measure of deformation which relates strain to displacement.
- (5) A constitutive equation which relates the measure of deformation to stress.

The conservation of mass is stated as

$$\rho J = \rho_0 \quad (2.4)$$

where  $\rho_0$  is the density in the reference configuration,  $\rho$  is the density in the current configuration, and  $J$  is the determinant of the deformation matrix. Conservation of energy states

$$\rho \dot{U} = \boldsymbol{\sigma} : \mathbf{D} - \frac{\partial \mathbf{q}}{\partial x} + \rho s \quad (2.5)$$

where  $\dot{U}$  is the rate of internal work,  $\mathbf{D}$  is the symmetric part of the velocity gradient or rate of deformation,  $\mathbf{q}$  is the heat flux, and  $s$  is the power supplied by a heat source. In a purely mechanical process this equation reduces to

$$\dot{U} = \boldsymbol{\sigma} : \mathbf{D} \quad (2.6)$$

which states that the internal rate of work or power is equivalent to the outer product of the Cauchy stress and the rate of deformation [ABAQUS, 2006]. From this it is determined that the Cauchy stress is conjugated in power to  $\mathbf{D}$  and thus any measure of stress must be conjugated to a specific measure of strain. Conservation of momentum produces the momentum equation which is expressed as

$$\frac{\partial \boldsymbol{\sigma}}{\partial x} + \rho \mathbf{b} = \rho \ddot{\mathbf{u}} \quad (2.7)$$

where  $\boldsymbol{\sigma}$  is the Cauchy stress,  $\mathbf{b}$  is the body force per unit mass, and  $\ddot{\mathbf{u}}$  is the body acceleration. A weak form solution to the momentum equation is the principle of virtual work. After discretizing the domain into a number of elements the discrete approximation to this solution can be written as

$$\mathbf{M} \ddot{\mathbf{u}} = \mathbf{f}^{ext} - \mathbf{f}^{int} \quad (2.8)$$

where  $\mathbf{M}$  is the mass matrix of the system,  $\mathbf{f}^{ext}$  is a vector of external nodal forces, and  $\mathbf{f}^{int}$  is a vector of internal nodal forces. These equations are a system of  $N^{DOF}$  ordinary differential equations where  $N^{DOF}$  represents the number of degrees of freedom or the number of nodal acceleration/velocity components. After nodal accelerations are

obtained, the nodal velocities, the rate of deformation and finally stresses are computed in that order [Belytschko, Liu, and Moran, 2000].

## 2.2. General Solution and Algorithm for Explicit Analysis

The explicit solution to (2.8) generally uses the central difference technique [Belytschko, Liu, and Moran, 2000]. Recognizing that the time step  $\Delta t$  changes as the continuum deforms the time increments are defined as shown in Figure. 2.1.

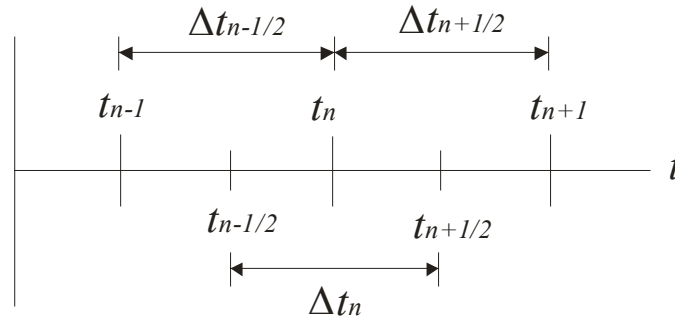


Figure 2.1. Time increments using the central difference method

Thus the time increment at step  $n$  can be written as

$$\Delta t^n = t^{n+1/2} - t^{n-1/2} \quad (2.9)$$

where

$$t^{n+1/2} = \frac{1}{2}(t^{n+1} + t^n) \quad (2.10)$$

And the partial time increment can be written as

$$\Delta t^{n+1/2} = t^{n+1} - t^n \quad (2.11)$$

The central difference formula for the acceleration is written as

$$\ddot{\mathbf{u}}^n = \left( \frac{\dot{\mathbf{u}}^{n+1/2} - \dot{\mathbf{u}}^{n-1/2}}{t^{n+1/2} - t^{n-1/2}} \right) \quad (2.12)$$

Rearranging and recognizing that  $t^{n+1/2} - t^{n-1/2} = \Delta t^n$  gives the following expression for velocity at the partial step.

$$\dot{\mathbf{u}}^{n+1/2} = \dot{\mathbf{u}}^{n-1/2} + \Delta t^n \ddot{\mathbf{u}}^n \quad (2.13)$$

which can be rewritten by braking into two substeps by

$$\dot{\mathbf{u}}^{n+1/2} = \dot{\mathbf{u}}^n + (t^{n+1/2} - t^n) \ddot{\mathbf{u}}^n \quad (2.14)$$

where

$$\dot{\mathbf{u}}^n = \dot{\mathbf{u}}^{n-1/2} + (t^n - t^{n-1/2}) \ddot{\mathbf{u}}^n \quad (2.15)$$

The central difference formula for the velocity at the half step is written as

$$\dot{\mathbf{u}}^{n+1/2} = \left( \frac{\mathbf{u}^{n+1} - \mathbf{u}^n}{t^{n+1} - t^n} \right) \quad (2.16)$$

Rearranging and recognizing that  $t^{n+1} - t^n = \Delta t^{n+1/2}$  gives the following expression for the displacement at the next step.

$$\mathbf{u}^{n+1} = \mathbf{u}^n + \Delta t^{n+1/2} \dot{\mathbf{u}}^{n+1/2} \quad (2.17)$$

Using these equations the solution to (6) for the nodal velocities can be expressed as

$$\dot{\mathbf{u}}^{n+1/2} = \dot{\mathbf{u}}^{n-1/2} + \Delta t^n \mathbf{M}^{-1} (\mathbf{f}^{ext} - \mathbf{f}^{int}) \quad (2.18)$$

where  $(\mathbf{f}^{ext} - \mathbf{f}^{int})$  can be computed using the strain-displacement equations. If  $\mathbf{M}$  is a diagonal matrix, often referred to as the lumped mass matrix, then the above expression does not require the solution of any equations. Determining the nodal velocities only requires a single computation hence, the efficiency of the explicit integration technique [Belytschko, Liu, and Moran, 2000].

The following is a general algorithm for the solution of non-linear finite element problems using the explicit integration technique. The algorithm is based on the algorithm presented by [Belytschko, Liu, and Moran, 2000].

Step 1. Set the initial conditions

$$\text{Set } n=0, t=0, \mathbf{u}^{n=0} = 0.$$

$$\text{Set initial velocities, } \dot{\mathbf{u}}^{n=0}.$$

$$\text{Set initial stresses, } \sigma^{n=0}.$$

$$\text{Set } \dot{\mathbf{u}}^{n-1/2} = \dot{\mathbf{u}}^{n=0}.$$

Step 2. Compute the diagonal lumped mass matrix  $\mathbf{M}$ .

Step 3. Compute nodal forces (*COMPUTE\_FORCE Procedure*).

Step 4. Compute initial nodal accelerations

$$\ddot{\mathbf{u}}^n = \mathbf{M}^{-1}(\mathbf{f}^n)$$

Step 5. Update time

$$t^{n+1} = t^n + \Delta t^{n+1/2}, t^{n+1/2} = \frac{1}{2}(t^n + t^{n+1})$$

Step 6. Update nodal velocities at half step

$$\dot{\mathbf{u}}^{n+1/2} = \dot{\mathbf{u}}^{n-1/2} + (t^{n+1/2} - t^n)\ddot{\mathbf{u}}^n$$

Step 7. Enforce velocity boundary conditions.

Step 8. Update nodal displacements

$$\mathbf{u}^{n+1} = \mathbf{u}^n + \Delta t^{n+1/2}\dot{\mathbf{u}}^{n+1/2}$$

Step 9. Compute nodal forces (*COMPUTE\_FORCE Procedure*).



Step 10. Compute  $\ddot{\mathbf{u}}^{n+1}$

$$\ddot{\mathbf{u}}^{n+1} = \mathbf{M}^{-1}(\mathbf{f}^{n+1})$$

Step 11. Update nodal velocities at next step

$$\dot{\mathbf{u}}^{n+1} = \dot{\mathbf{u}}^{n+1/2} + (t^{n+1} - t^{n+1/2})\ddot{\mathbf{u}}^{n+1}$$

Step 12. Check energy balance at time step  $n+1$

Step 13. Update step counter

$$n = n + 1$$

Step 14. Create output. If  $t^{n+1} < t^f$  go to step 5.

### ***COMPUTE\_FORCE Procedure***

Step 1. Initialize  $\mathbf{f}^n = (\mathbf{f}^{ext} - \mathbf{f}^{int}) = 0$ ,  $\Delta t_{crit} = \infty$ .

Step 2. Compute global external nodal forces,  $\mathbf{f}_n^{ext,n}$ .

Step 3. Loop over all elements.

Step 3.1. Get element nodal displacements  $\mathbf{u}_e^n$  and velocities  $\dot{\mathbf{u}}_e^n$ .

Step 3.2. Set the internal nodal forces for the element  $\mathbf{f}_e^{int,n} = 0$ .

Step 3.3. Loop over all integration points.

Step 3.3.1. If  $n = 0$ , go to step 3.3.4

Step 3.3.2. Compute measure(s) of deformation

$\mathbf{D}^{n-1/2}$  - Rate of deformation tensor

$\mathbf{F}^n$  - Deformation gradient

$\mathbf{E}^n$  - Lagrangian/Green strain

Step 3.3.3. Relate deformation to stress  $\sigma^n$  through constitutive equation.

Step 3.3.4. Relate stress to internal forces and add to sum  $\mathbf{f}_e^{\text{int},n}$

Step 3.3.5. End integration point loop.

Step 3.4. Compute external forces on element,  $\mathbf{f}_e^{\text{ext},n}$ .

Step 3.5. Compute,  $\mathbf{f}_e^n = (\mathbf{f}_e^{\text{ext}} - \mathbf{f}_e^{\text{int}})$ .

Step 3.6. Compute new critical time step for element,  $\Delta t_{crit}^e$

If  $\Delta t_{crit}^e < \Delta t_{crit}$  then set  $\Delta t_{crit} = \Delta t_{crit}^e$ .

Step 3.7. Construct element forces  $\mathbf{f}_e^n$  into global nodal forces  $\mathbf{f}^n$ .

Step 3.8. End loop over elements.

Step 4. Set  $\Delta t^{n+1/2} = \beta \Delta t_{crit}$ , where  $\beta$  is a reduction factor that is typically used to prevent instabilities.

There are also many additional topics related to explicit finite element analysis that were not covered in this section but are typically considered by most commercial codes. These include contact/impact algorithms, damping forces, hourglass resistance, inclusion of artificial bulk viscosity etc.

### 2.3. Quasi-static simulations using Explicit Finite Element Analysis

As discussed earlier the dynamic explicit approach has the drawback that it is conditionally stable. The stability limit for the explicit integration operator is that the maximum time increment must be less than a critical value of the smallest transition

times for a dilatational wave to cross any element in mesh. Figure 2.2 shows schematic of a 2-D mesh with three elements.

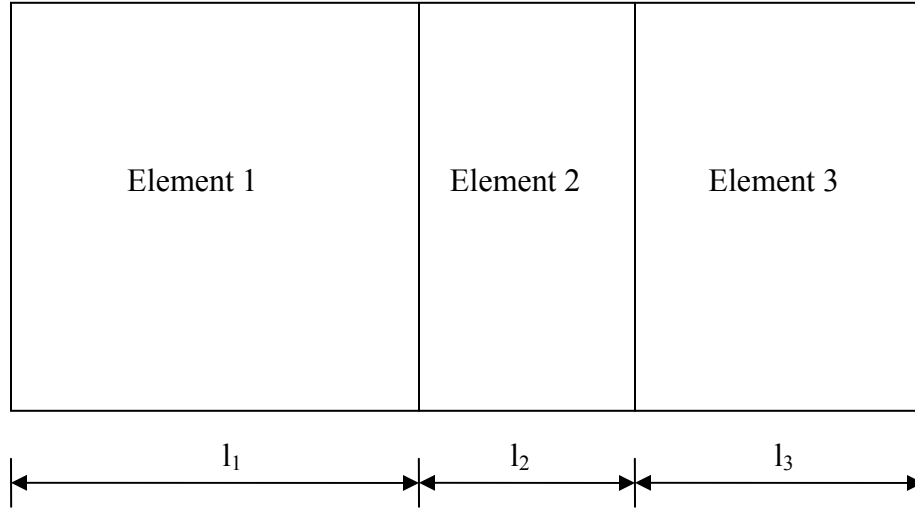


Figure 2.2. Schematic diagram showing three elements in a 2-D mesh

As shown in figure 2.2 element 2 has lowest length so, the global time step will be governed by this element. The global time step will be given by

$$\Delta t = \frac{l_{\min}}{c} = \frac{l_2}{c} \quad (2.19)$$

$$\text{Where, } c = \sqrt{\frac{E}{(1-\nu^2)\rho}} \quad (2.20)$$

Since, the time step is dependent on the density of the material, so the density can be adjusted to achieve the desired time step.

$$\left( \frac{\Delta t_{\text{specified}}}{l_i} \right)^2 = \frac{(1-\nu^2)\rho_i}{E} \quad (2.21)$$

$$\rho_i = \frac{(\Delta t_{\text{specified}})^2 E}{l_i^2 (1 - \nu^2)} \quad (2.22)$$

As explicit finite element approach needs very small time increment so, it leads to a huge amount of computational time in case of quasi-static analysis. Therefore, to solve quasi-static problems, it is conventional to convert the real problem to a virtual problem with a different mass density and processing time by means of mass and time scaling as explained below.

- 1) Time scaling is a term referred to the increase in the speed of the process by increasing loading rate e.g. increase in stroke displacement rate in case of simple tensile test and
- 2) Mass-scaling is a term that is used for the process of scaling the element's mass or density in explicit simulations to adjust its time step.

### 3. KEVLAR GEOMETRY AND SINGLE YARN TENSILE TESTS

#### 3.1. Introduction

As discussed in Chapter 1, there are several techniques for modeling the fabric using finite elements. A micromechanical approach captures the actual fabric geometry by modeling each individual yarn and its weave pattern with solid finite elements. Figure 3.1 shows an example of a micromechanical finite element model of Kevlar<sup>®</sup>49.

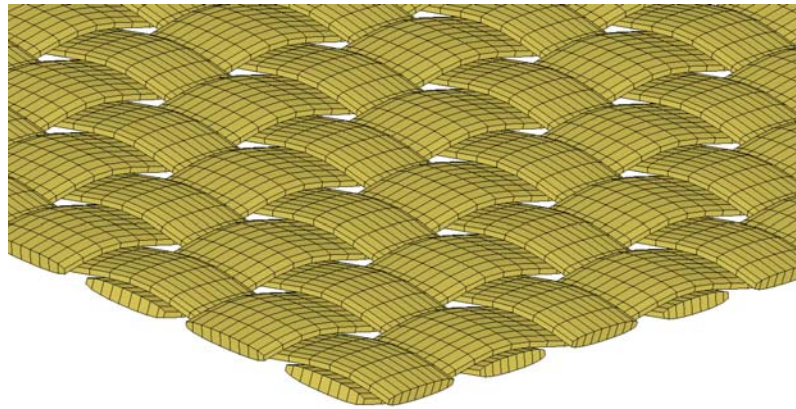


Figure 3.1. Micromechanical FE model of Kevlar<sup>®</sup>49

To enable the explicit finite element modeling of Kevlar fabric, the Kevlar geometry and material properties of single yarn needs to be determined. An experimental procedure is developed to capture the geometry of Kevlar woven fabric both in undeformed and deformed states. The geometry at the undeformed state was used to build the micromechanical model whereas the deformed geometry was used to validate the model. The Kevlar yarn material model was implemented via user defined subroutine (UMAT) in LS-DYNA. This material model is based on the single yarn tensile tests and other properties available in the literature.

### 3.2. Kevlar Geometry Computation

Schematic of overall procedure used to capture the Kevlar geometry is shown in Figure 3.2. Tensile tests were conducted to load the specimens to predefined strain. To provide good strength to samples and avoid any distortion during processing, samples were potted into epoxy. They were then cut and polished for good surface finish. These finished samples were observed using Optical Microscopy and images of cross-section were taken. These images were digitized and parameters associated with the geometry were computed. These steps are explained in detail in following sections.

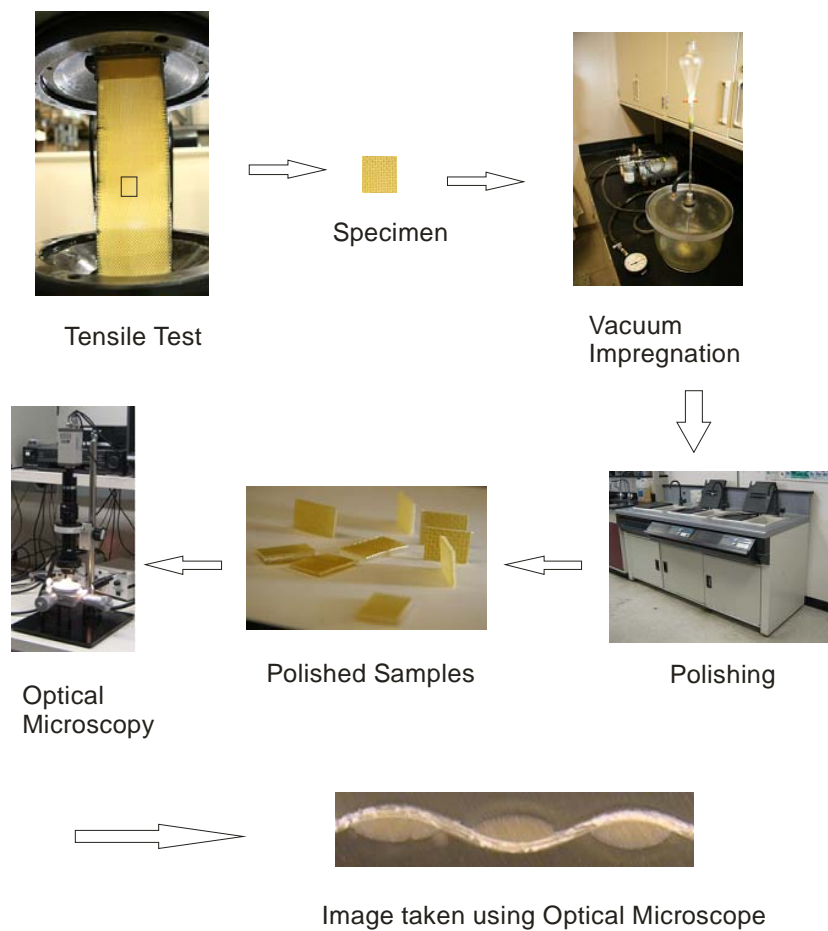


Figure 3.2. Schematic of overall experimental procedure

### 3.2.1. Sample Preparation

In order to capture the geometry of the Kevlar fabric, it is essential to cut the Kevlar samples with minimum distortion. However, it is difficult to cut a section of a fabric without unraveling the filaments near the cut. So, the samples were potted in the epoxy (EPOTEK 301). EPOTEK 301 has low viscosity and good optical properties. The function of epoxy is to provide good strength to Kevlar yarns and avoid any undesirable distortion during handling and cutting.

To capture the effect of strain level on the Kevlar geometry, tensile test on the Kevlar swatch were conducted. Three strain levels used in this research are 1.0%, 1.5% and 2.0%. Tests were conducted under stroke control condition with a stroke rate of 0.05 in/min and samples were loaded until these strain levels were reached. Samples size of 2.5" x 10" was used for all tests. Once specified strain level is reached samples were hold under stroke control condition. This ensures the constant strain level during sample preparation. In order to avoid re-orientation of yarns during unloading of samples, glue was applied on both sides of the sample under loaded condition. Three layers of glue were applied at an interval of 15 minutes each to get enough strength to restrict yarns from re-orientation during unloading. The sample was kept in loading position until glue is dried and gained strength. Samples were then removed from the testing frame and glued portion of the specimen was cut and potted in the epoxy. Figure 3.3 shows the stress strain curves for these three samples and Figure 3.4 shows the Kevlar specimen during test.

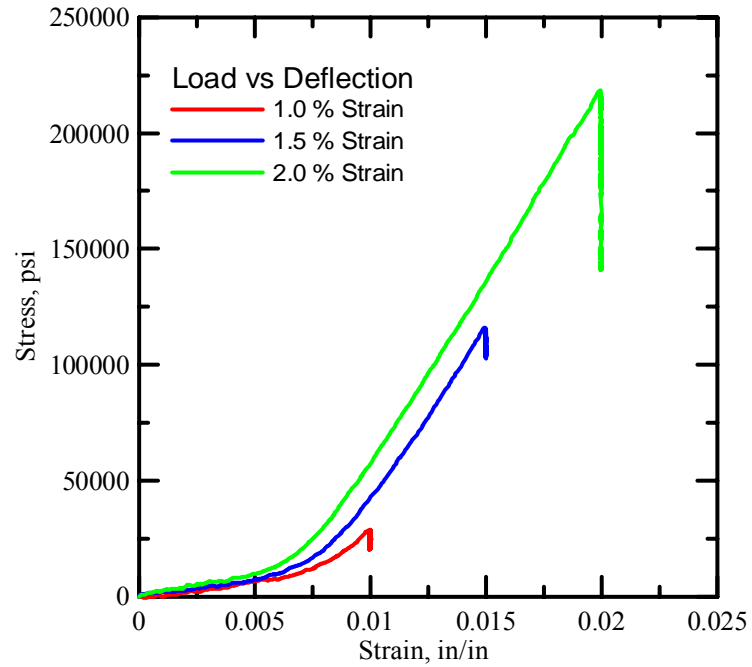


Figure 3.3. Stress Strain curve of Kevlar during test

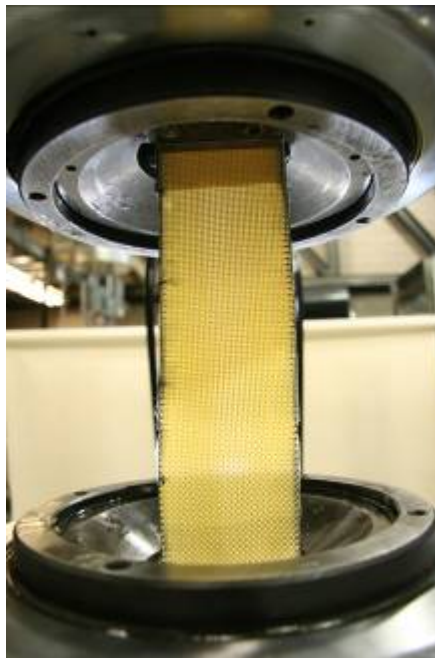


Figure 3.4. Sample held under constant strain level



### 3.2.2. Vacuum Impregnation

To ensure proper penetration of epoxy between yarns and fibers, vacuum impregnation was used. The samples prepared as per above procedure were soaked in the epoxy and kept in the vacuum jar. A constant vacuum of 25 in Hg or -85 KPa was applied for 1 hour. The samples were then removed from the vacuum jar and placed at room temperature for overnight curing. Vacuum apparatus used is shown in Figure 3.5.



Figure 3.5. Vacuum Apparatus

### 3.2.3. Cutting and Polishing

The samples potted in epoxy were cut to small size suitable for Optical Microscopy and were polished using variable speed polisher. This step is essential due to two reasons, first it is important to ensure that the cutting plane represents mid plane of the yarn as geometrical parameters changes with the location of cutting plane and second the quality of images depends on the surface finish. To ensure there is minimum effect of handling on the samples, the outer yarns were cut and removed as their geometry is prone

to be affected by handling during the sample preparation. The yarns which are near the center of the fabric were analyzed using Optical Microscopy. It is observed that the warp and fill direction have different geometric configuration. So, to track fill and warp directions, samples were cut in rectangular shape, longer side represents warp direction where as short side represents fill direction. All images were stored using a protocol which includes cross-section type, strain level and image number.

To get the good surface finish two levels of polishing was used using variable speed polisher. First samples were rough polished using Silicon Carbide Paper P#800 followed by fine polishing using 1 micron polishing paper. Due to small size, it is difficult to hold the samples vertically using hands so, rubber squeegee were used. The advantage of using the rubber squeegee was two fold. First, the samples were hold perfectly in vertical position and second there are lesser vibrations on the samples which ensure better surface finish. Polishing machine is shown in Figure 3.6 and finished samples are shown in Figure 3.7.



Figure 3.6. Polishing equipment

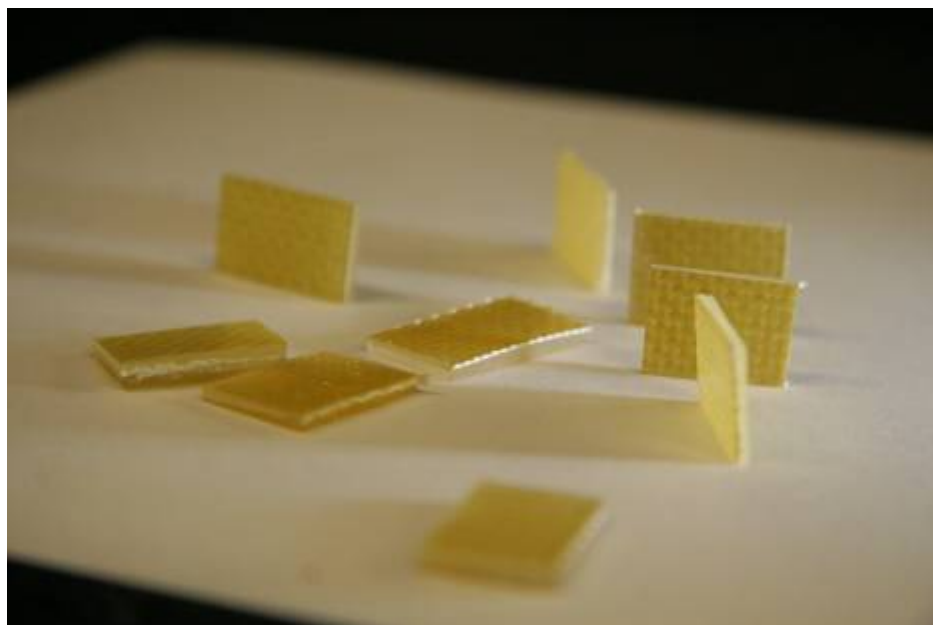


Figure 3.7. Finished Kevlar Samples

### 3.2.4. Optical Microscopy

Optical microscopy was used to take images of the Kevlar cross section. The polished samples of the Kevlar were placed vertically under the microscope with their cross-section facing the camera. Microscopy facility used is shown in Figure 3.8. The microscope was focused so as to obtain at least one complete sin curve of the longitudinal yarn. To calibrate the image, pictures of scale were also taken at the same microscope settings. Figure 3.9 shows the images of longitudinal cross-section of fill yarn under different strain levels and Figure 3.10 shows images of longitudinal cross-section of warp yarn under different strain levels.

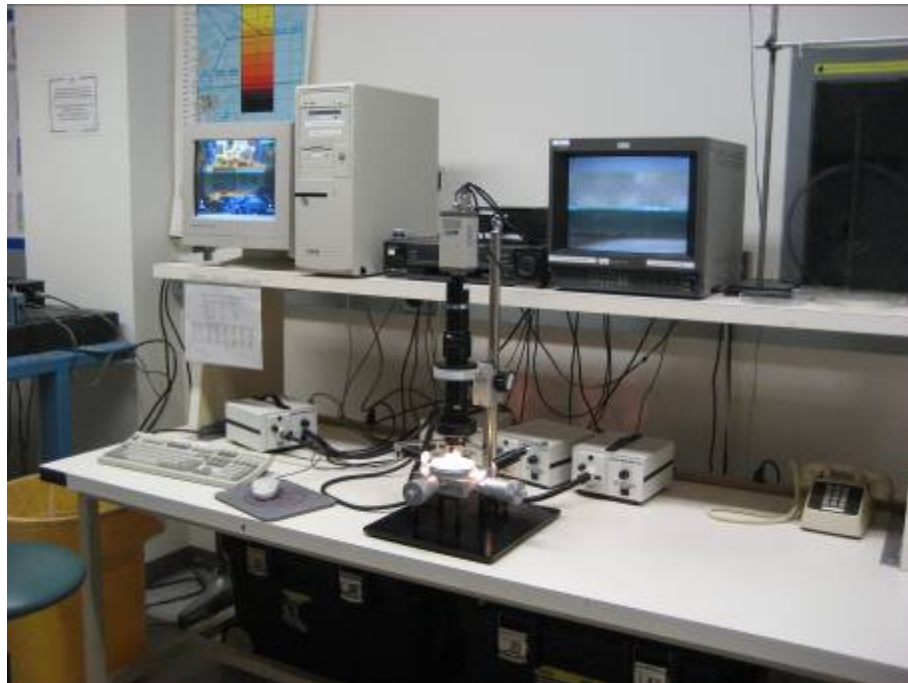


Figure 3.8. Optical Microscopy equipment



Figure 3.9 (a). Fill yarn longitudinal cross-section – undeformed geometry

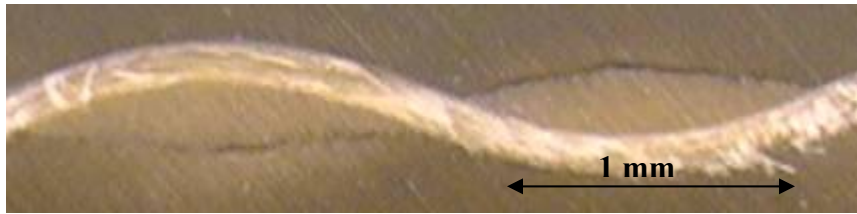


Figure 3.9 (b). Fill yarn longitudinal cross-section under 1.0% Strain level



Figure 3.9 (c). Fill yarn longitudinal cross-section under 1.5% Strain level

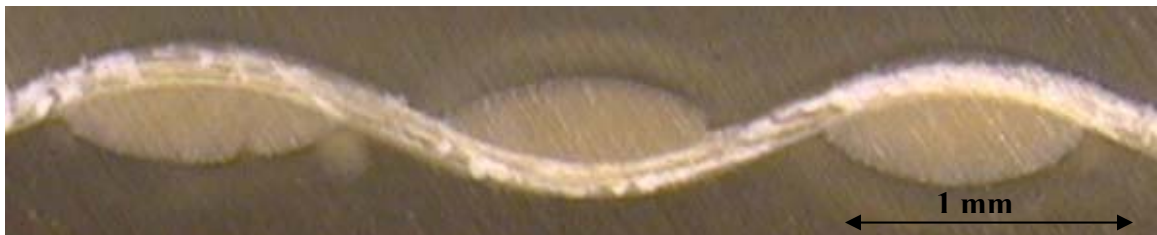


Figure 3.9 (d). Fill yarn longitudinal cross-section under 2.0% Strain level



Figure 3.10 (a). Warp yarn longitudinal cross-section – undeformed geometry



Figure 3.10 (b). Warp yarn longitudinal cross-section under 1.0% Strain level



Figure 3.10 (c). Warp yarn longitudinal cross-section under 1.5% Strain level



Figure 3.10 (d). Warp yarn longitudinal cross-section under 2.0% Strain level

It can be seen from these images that in undeformed state, fill and warp yarns can be considered as having elliptical cross-section (transverse cross-section) which follows sinusoidal curve (longitudinal cross-section). As the Kevlar fabric is loaded along the warp direction the fibers along loaded direction (warp) tries to straighten out while the

yarn in perpendicular direction (fill) becomes wavier. The waviness of fill yarn increases as the strain level increases. This can be considered as the transfer of crimp from warp yarns to fill yarns. Also, the warp yarns try to become more circular from elliptical cross-section while the cross-section of fill yarns becomes flatter.

### 3.2.5. Image Analysis

The geometric parameters associated with Kevlar yarn can be computed by approximating its cross-section with ellipse which follows sinusoidal path. The parameters associated with these curves were computed by digitizing points along these curves and fitting them using least square method. MATLAB programs are written to compute parameters associated with sine and ellipse curves. Further, as the samples are loaded the warp yarns are trying to straighten out by removal of crimp however, the interfacial pressure between fill and warp yarns doesn't allow warp yarns to become complete straight. This leads warp yarns to represent more of step function under load than sine function. So, warp yarns under load are fitted using step function instead of sine curves. This method is used to compute parameters separately for each sample at different strain level. The overall or average parameters were computed by fitting a single curve through all the selected points from different samples at a strain level.

#### Sine curve

General equation of sin curve is given by

$$f(x) = a \sin(bx + c) + d + ex \quad (3.1)$$

where  $a$  is amplitude,  $b$  is frequency,  $c$  is phase shift,  $d$  is shift along  $y$  direction and  $e$  is slope of the sin curve.

A MATLAB program is written which can be used to select points along the sinusoidal path and these points were then curve fitted in least square sense to compute the parameters given by above equation. The curve based on the estimate is then superimposed on the original image to check the quality of the fitted data. Black sin curve shown below shows the sin curve fitted to the image.

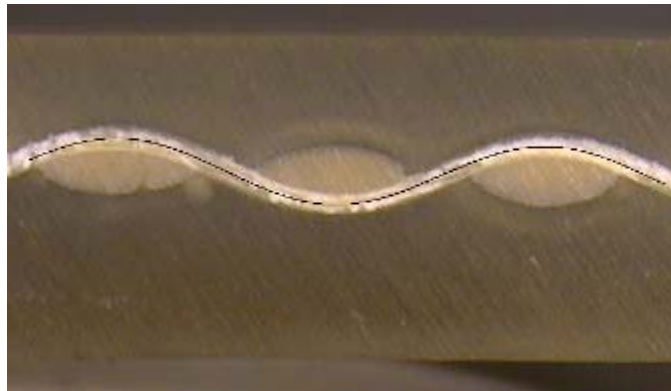


Figure 3.11. Sin curve parameter estimation

To estimate sinusoidal curve parameters with accuracy, number of samples were prepared for each fill and warp direction at different strain levels. For each sample, points along the sine curve were selected and parameters were estimated. The overall or average parameters were then computed by fitting single sinusoidal curve through all the selected points. Figure 3.12 represents one of such fit for warp direction undeformed samples.



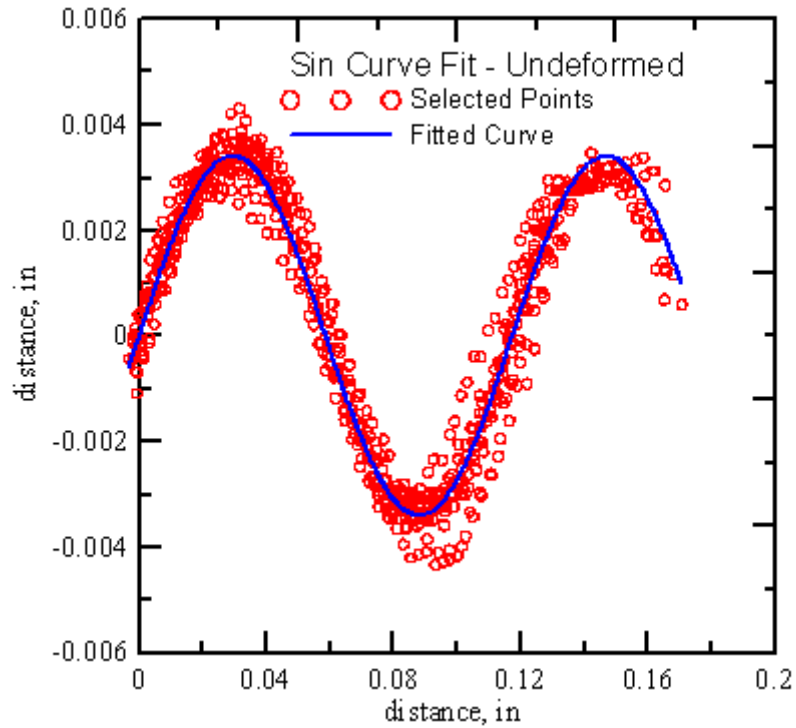


Figure 3.12. curve fit through point cloud

### Ellipse

Similar to the sine curve fitting, cross-section of the yarn was fitted by using elliptical approximation. The general equation of the ellipse in polar coordinates is given by

$$r = \frac{ab}{\sqrt{a^2 \sin^2 \theta + b^2 \cos^2 \theta}} \quad (3.2)$$

Where,  $r$  is radius (distance of point from center) and  $\theta$  is angle made by line joining center and point on ellipse circumference with  $x$  axis,  $a$  is semi-major axis and  $b$  is semi-minor axis.

A MATLAB program is written to compute the parameters associated with ellipse. Using this program points can be selected along the elliptical cross-section which

were then curve fitted in least square sense to compute the unknowns. The curve based on the estimate is then superimposed on the original image to check the quality of the fitted data. Black sin curve shown below shows the sin curve fitted to the image.

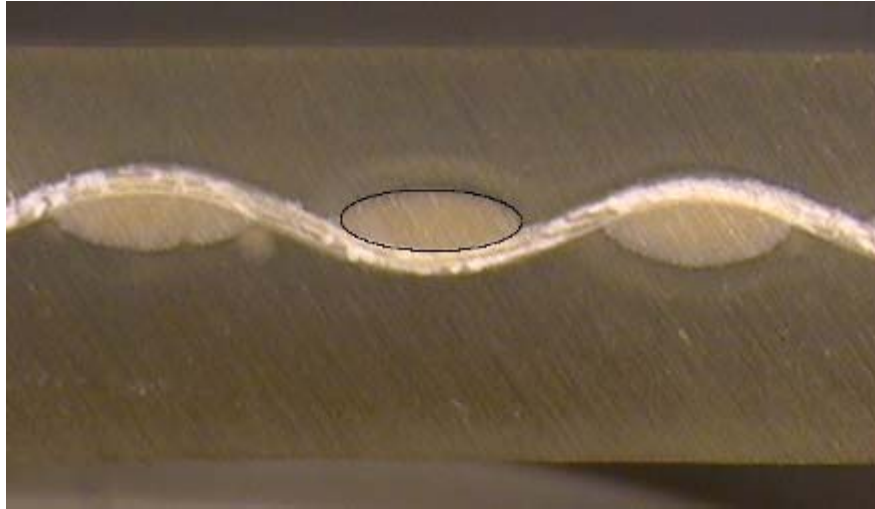


Figure 3.13. Cross section approximation using ellipse

To estimate elliptical curve parameters with accuracy, number of samples was prepared for each fill and warp direction at different strain levels. For each sample, points along the cross-section were selected and parameters were estimated. The overall or average parameters were then computed by fitting single elliptical curve through all the selected points. Figure 3.14 shows the curve fitted through all the data points selected for different samples.

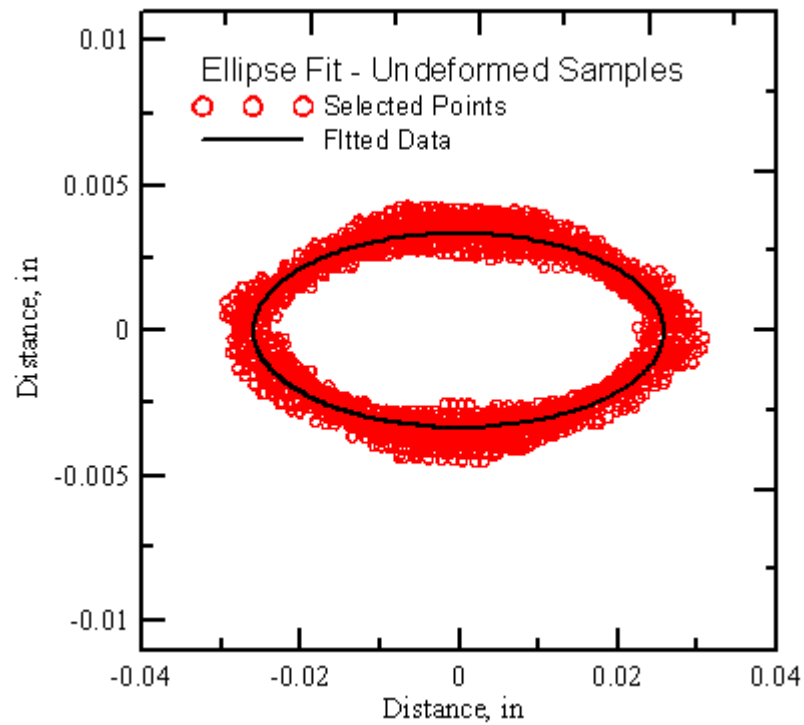


Figure 3.14: Ellipse fit through point cloud

### Step Function

As the warp yarns are loaded they try to straighten out. However, there is considerable resistance from fill yarns so, instead of straighten out complete warp yarns left with peak and valley at the location of fill yarns which can best be approximated using step function. Figure 3.15 shows the cross-section of warp yarn under strain which is approximated using step function. Since the step of the step function is small and its get smaller as we increase strain level so, it becomes increasingly difficult to fit step function through the selected points. So, instead of fitting step function as a single function in the curve two straight lines were fitted through the selected points on the warp yarns. The distance between these two lines was taken as step height.

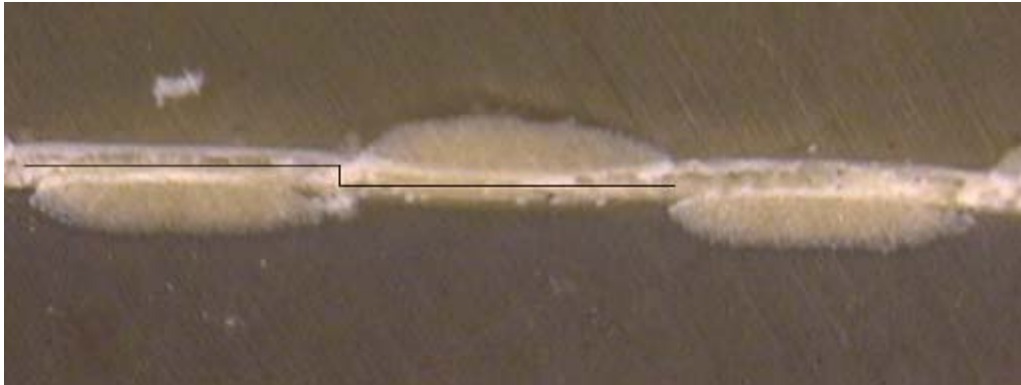


Figure 3.15. Cross section approximation using step function

### 3.2.6. Results and Discussion

The procedure discussed above was used to estimate the geometrical parameters for fill and warp yarns. The parameters associated with warp and fill yarns were estimated for undeformed samples as well as 1.0%, 1.5% and 2.0% strained samples.

#### Fill Yarns - Transverse Cross-section

The images taken along transverse cross-section of fill yarns were used to estimate the parameters associated with the fill yarn cross-section and the effect of strain on the fill yarns. Figures 3.16 shows the undeformed geometry of the fill yarn where as Figure 3.17, 3.18 and 3.19 shows the effect of strain levels on the transverse geometry of the fill yarns.

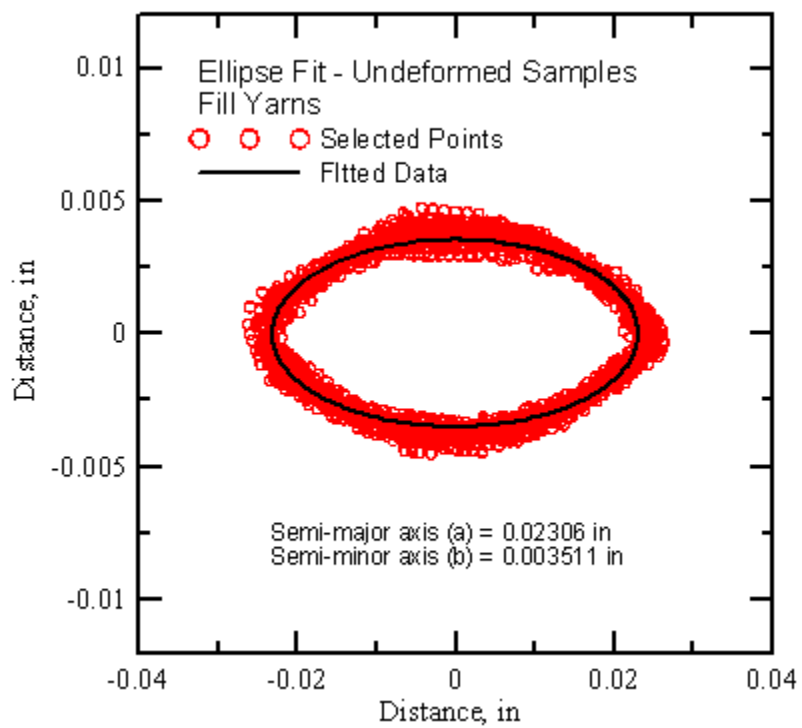


Figure 3.16. Fill cross-section (undeformed) ellipse curve fit through point cloud

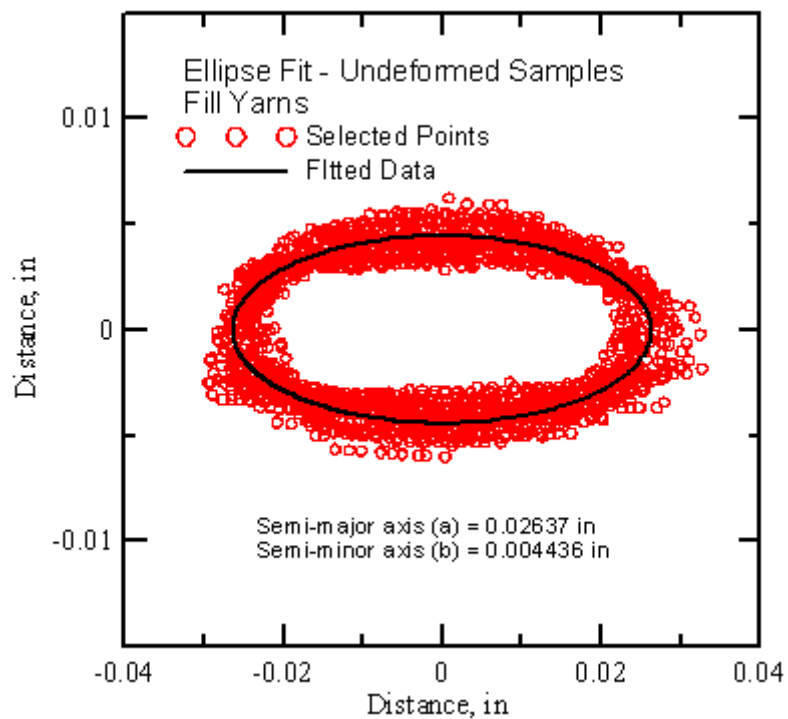


Figure 3.17. Fill cross-section (1.0 % Strain) ellipse curve fit through point cloud

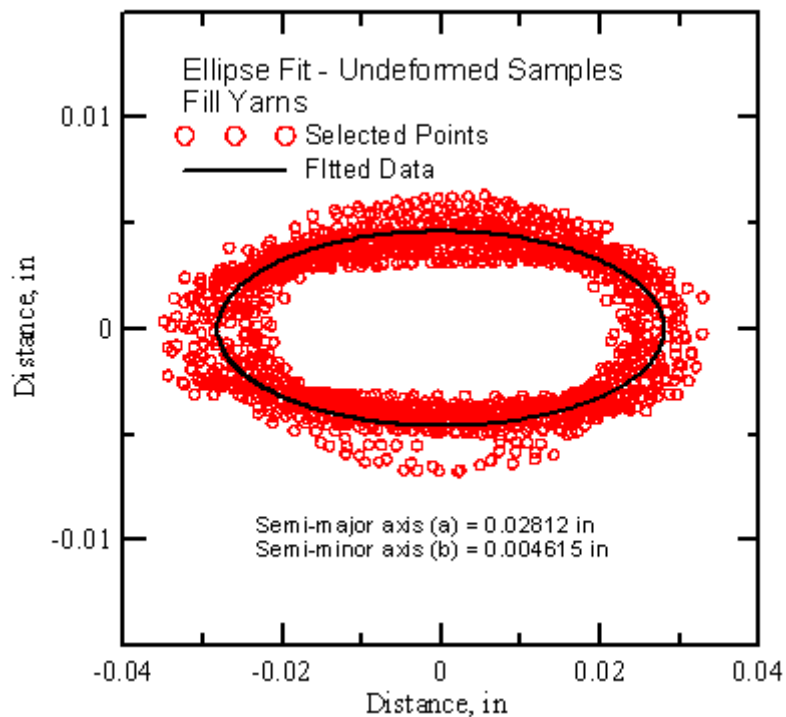


Figure 3.18. Fill cross-section (1.5 % Strain) ellipse curve fit through point cloud

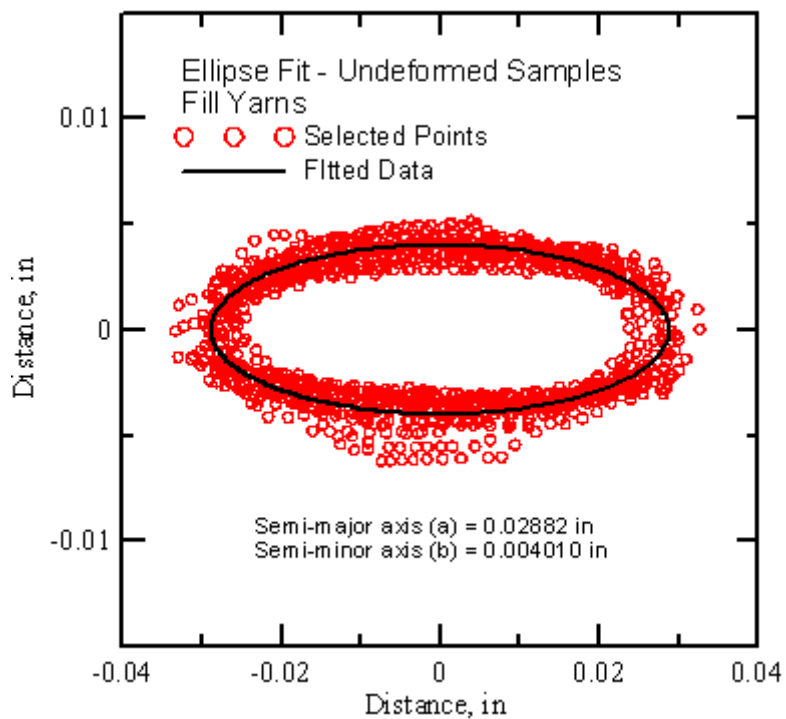


Figure 3.19. Fill cross-section (2.0 % Strain) ellipse curve fit through point cloud

Table 3.1 summarizes the parameters associated with the fill yarns for various loading conditions. The semi major axis (a) and semi minor axis (b) are shown for all samples at different strain levels. The parameters computed using point cloud approach is also shown in the table.

Table 3.1. Fill direction ellipse curve parameters

Sample #	0.0% strain level		1.0% strain level		1.5% strain level		2.0% strain level	
	a (in)	b (in)	a (in)	b (in)	a (in)	b (in)	a (in)	b (in)
1	0.0245	0.0038	0.0249	0.0043	0.0295	0.0046	0.0289	0.0043
2	0.0237	0.0038	0.0274	0.0040	0.0284	0.0045	0.0300	0.0050
3	0.0238	0.0037	0.0266	0.0037	0.0255	0.0052	0.0293	0.0036
4	0.0241	0.0035	0.0299	0.0039	0.0316	0.0047	0.0313	0.0038
5	0.0245	0.0038	0.0268	0.0044	0.0339	0.0043	0.0318	0.0039
6	0.0246	0.0035	0.0264	0.0046	0.0306	0.0047	0.0314	0.0036
7	0.0237	0.0035	0.0285	0.0039	0.0323	0.0042	0.0329	0.0034
8	0.0228	0.0038	0.0253	0.0040	0.0258	0.0049	0.0263	0.0039
9	0.0233	0.0036	0.0291	0.0036	0.0317	0.0043	0.0282	0.0039
10	0.0231	0.0037	0.0262	0.0040	0.0300	0.0044	0.0294	0.0039
11	0.0236	0.0036	0.0308	0.0040	0.0283	0.0047	0.0294	0.0033
12	0.0221	0.0036	0.0241	0.0045	0.0343	0.0039	0.0266	0.0038
13	0.0240	0.0037	0.0247	0.0050	0.0256	0.0058	0.0263	0.0039
14	0.0224	0.0035	0.0285	0.0050	0.0308	0.0042	0.0270	0.0037
15	0.0242	0.0035	0.0219	0.0045	0.0313	0.0048	0.0272	0.0041
16	0.0231	0.0034	0.0259	0.0051	0.0248	0.0043	0.0299	0.0035
17	0.0242	0.0036	0.0260	0.0052	0.0236	0.0047	0.0297	0.0041
18	0.0226	0.0036	0.0248	0.0049	0.0259	0.0040	0.0260	0.0051
19	0.0236	0.0036	0.0268	0.0047	0.0226	0.0048	0.0296	0.0044
20	0.0238	0.0037	0.0242	0.0043	0.0225	0.0047	0.0302	0.0036
<b>Average</b>	0.0236	0.0036	0.0264	0.0044	0.0285	0.0046	0.0291	0.0039
<b>Std. Dev</b>	0.0007	0.0001	0.0022	0.0005	0.0037	0.0004	0.0020	0.0005
<b>Average using point cloud</b>	0.0231	0.0035	0.0263	0.0044	0.0281	0.0046	0.0288	0.0040

Figure 3.20 shows the effect of strain on the semi-major axis of the fill yarns. The semi-major axis of yarns increases with increase in the strain level. It is interesting to note that the effect of the loading on the semi-major axis can be represented by linear curve in the current strain level range. It can be noted that the increase in the semi-major axis is not significant after 1.5 % strain level.

The effect of strain on the semi-major axis can be represented by following equation

$$\text{Semi-major axis (a)} = 0.289 * \text{strain} + 0.0235 \quad (3.3)$$

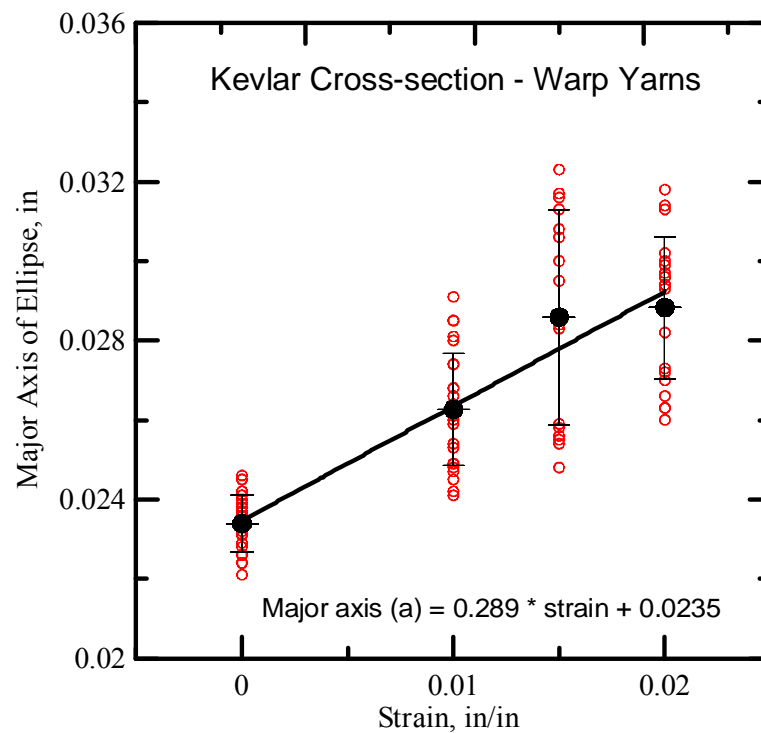


Figure 3.20. Comparison of Fill cross-section (ellipse) at different strain levels



Figure 3.21 shows the effect of strain level on the semi-minor axis of the fill yarns. The semi-minor axis of the fill yarns increases as the strain level increases. This means the density of the fill yarns reduces or the voids between fibers increases. Further, since the fill yarns become flat or more of rectangular in cross-section under load the approximation of the transverse cross-section with ellipse also added some error in the estimation. The equation of the fitted curve describing strain effect on the yarn geometry can be represented using following equation

$$\text{Semi-minor}(b) = 0.0035 + 0.17 * \text{strain} - 7.32 * (\text{strain})^2 \quad (3.4)$$

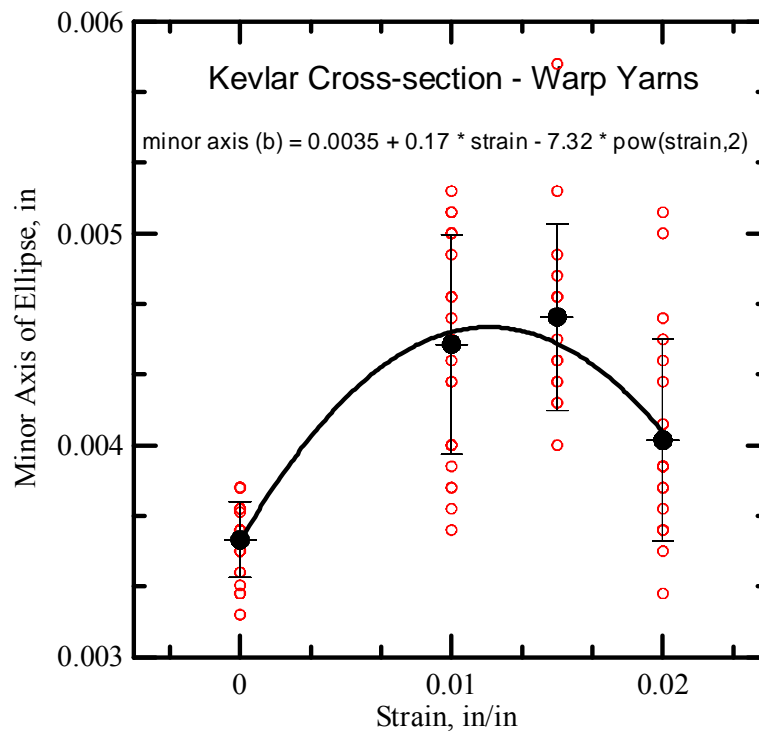


Figure 3.21. Comparison of Fill cross-section (ellipse) at different strain levels

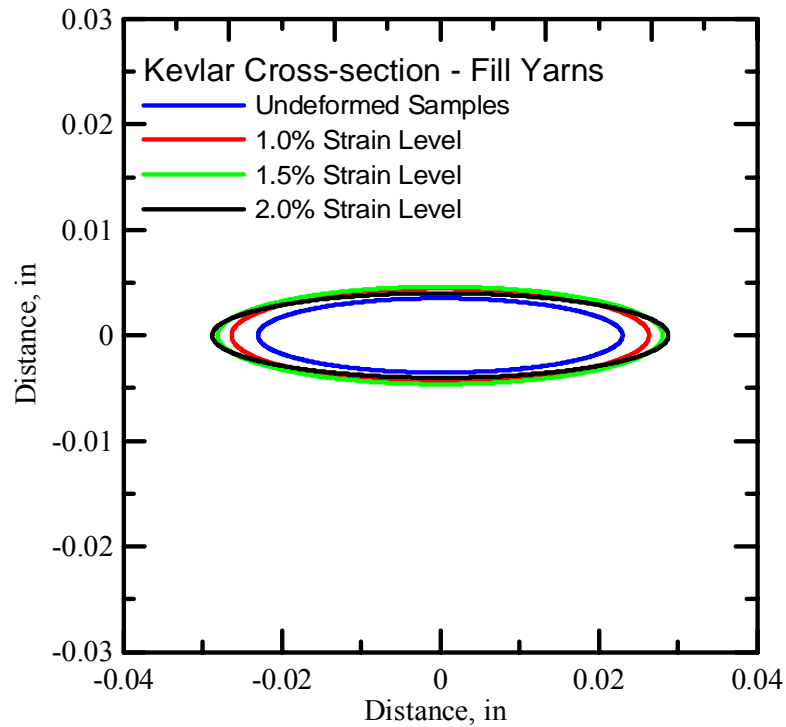


Figure 3.22. Comparison of Fill cross-section (ellipse) at different strain levels

Figure 3.23 shows the estimation of fill yarn transverse cross-section under loading. It is observed that as the strain level increases the semi-major axis of the yarns increases significantly while there is little increase in the semi-minor-axis of the yarns. So, the yarns become sparser or there is decrease in the density of the fill yarns as the warp yarns are loaded.

### Fill Yarns - Longitudinal Cross-section

The images taken along longitudinal cross-section of fill yarns were used to estimate the parameters associated with the fill yarn cross-section and the effect of strain on the fill yarns. Figures 3.23 shows the undeformed geometry of the fill yarn where as Figure 3.24, 3.25 and 3.26 shows the geometry of fill yarn at 1.0%, 1.5% and 2.0% strain level. Parameters for all the samples are listed in Table 3.2. The amplitude of the sine curve indicates the waviness of the yarn and period indicates the length of the complete sine curve. The amplitude and period associated with each sample was computed using image analysis and was plotted on a common scale. Curve fitted through all the points selected for various samples gives the overall estimation of parameters.

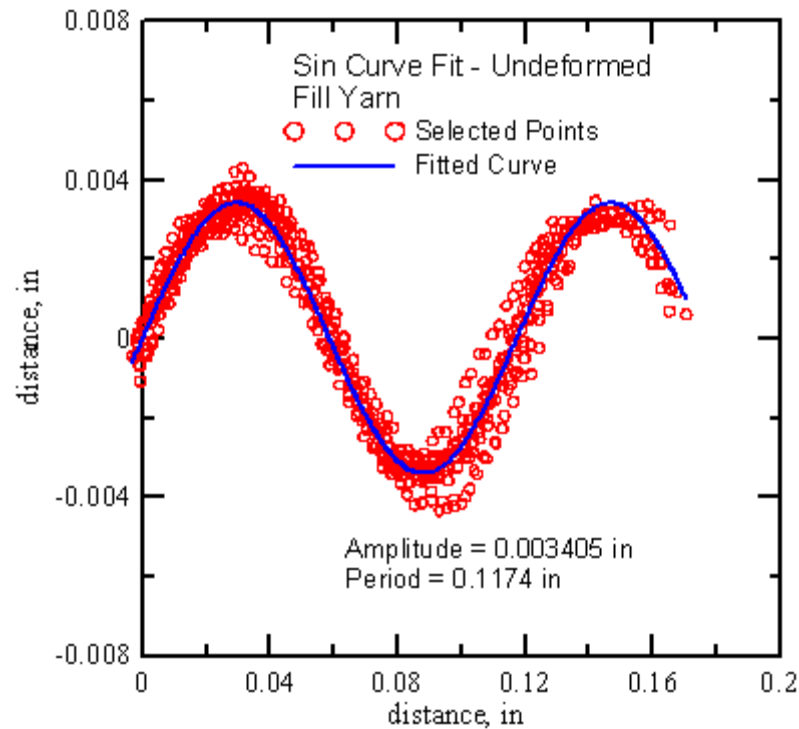


Figure 3.23. Fill cross-section (undeformed) sin curve fit through point cloud

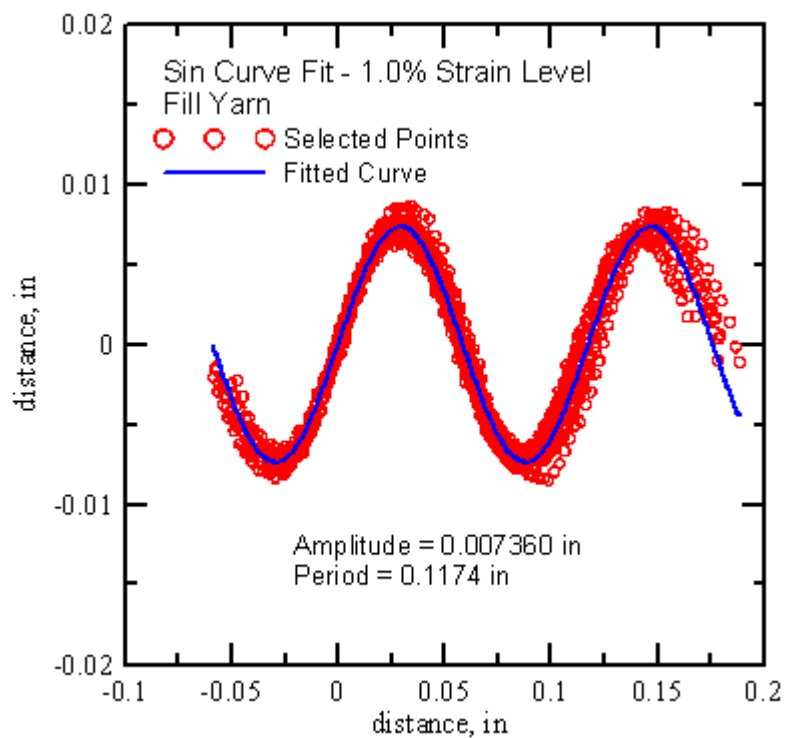


Figure 3.24. Fill cross-section (1.0% strain level) sin curve fit through point cloud

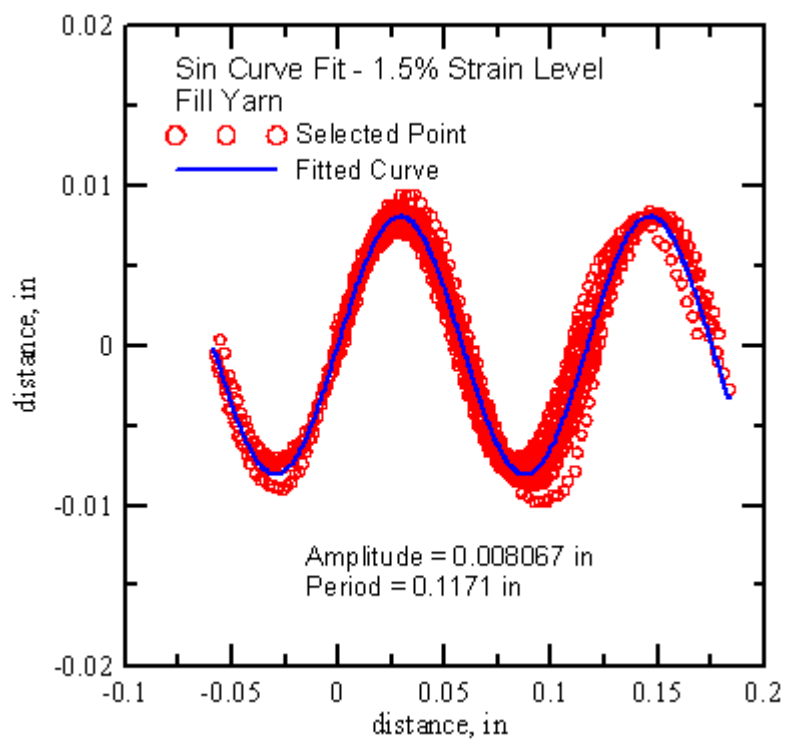


Figure 3.25. Fill cross-section (1.5% strain level) sin curve fit through point cloud

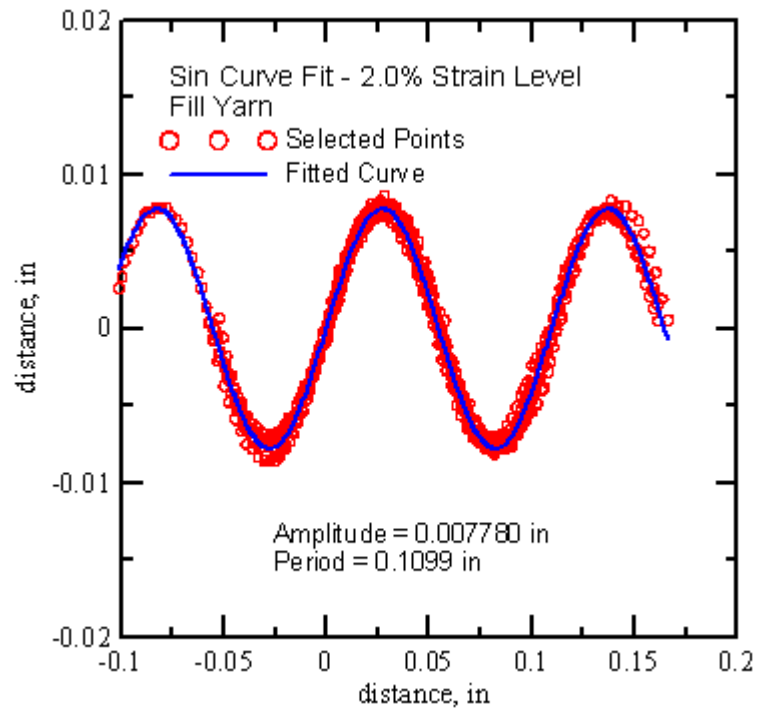


Figure 3.26. Fill cross-section (2.0% strain level) sin curve fit through point cloud

It can be observed that as the warp yarns are loaded the fill yarns tries to be come wavier which is indicated by the increase in the amplitude of the sine curve. Change in the period of the sine curve is also observed however, its very small.

Table 3.2. Fill direction sine curve parameters

Sample #	undeformed		1.0% strain Level		1.5% Strain Level		2.0% Strain Level	
	Amplitude (in)	Period (in)	Amplitude (in)	Period (in)	Amplitude (in)	Period (in)	Amplitude (in)	Period (in)
1	0.00301	0.10996	0.00691	0.11354	0.00873	0.11889	0.00824	0.1091
2	0.00353	0.11562	0.00681	0.11244	0.00747	0.11207	0.00752	0.10806
3	0.00349	0.11452	0.00674	0.11582	0.00798	0.11226	0.00759	0.11071
4	0.00349	0.11575	0.00703	0.11248	0.00804	0.11315	0.00805	0.10441
5	0.00414	0.11956	0.00765	0.11436	0.00812	0.11169	0.00773	0.10949
6	0.00342	0.11592	0.00757	0.11384	0.00848	0.11592	0.00779	0.10889
7	0.00333	0.11815	0.00691	0.11234	0.0084	0.11812	0.0074	0.10721
8	0.00312	0.11349	0.0069	0.11234	0.00789	0.11814	0.00757	0.11084
9	0.00377	0.12338	0.00705	0.11026	0.00757	0.11734	0.00868	0.11215
10	0.00363	0.11605	0.00797	0.11544	0.0079	0.12118	0.00817	0.11232
11	0.00333	0.1218	0.0071	0.11237	0.00899	0.11995	0.00794	0.11087
12			0.00732	0.11354	0.00854	0.11743	0.00774	0.11268
13			0.00733	0.1124	0.00816	0.12124		
14			0.00742	0.11422	0.00891	0.12045		
15			0.00832	0.12426	0.00987	0.12496		
Average	0.00348	0.11675	0.00715	0.1132	0.00814	0.11625	0.00788	0.10946
std dev	0.00031	0.0038	0.0004	0.0016	0.00047	0.00342	0.00038	0.00232
using point cloud	0.00341	0.1174	0.00736	0.11742	0.00807	0.11714	0.00778	0.10993

Figure 3.28 shows the effect of the strain on amplitude of the sine curve representing longitudinal cross-section of the fill yarns. It is observed that the fill yarn becomes wavier as the warp yarns are loaded this can be seen by the increase in the amplitude of the sine curve. This phenomenon can be looked as transfer of the slack from the warp yarns to the fill yarns. Further, the increase in the amplitude is much more

during initial phase of loading then later. A curve fitted through amplitude at different strain levels can be used to estimate the amplitude for the intermediate strain levels. The equation of the fitted curve obtained is

$$\text{Amplitude (A)} = 0.001072 * \ln(\text{strain}) + 0.01238 \quad (3.5)$$

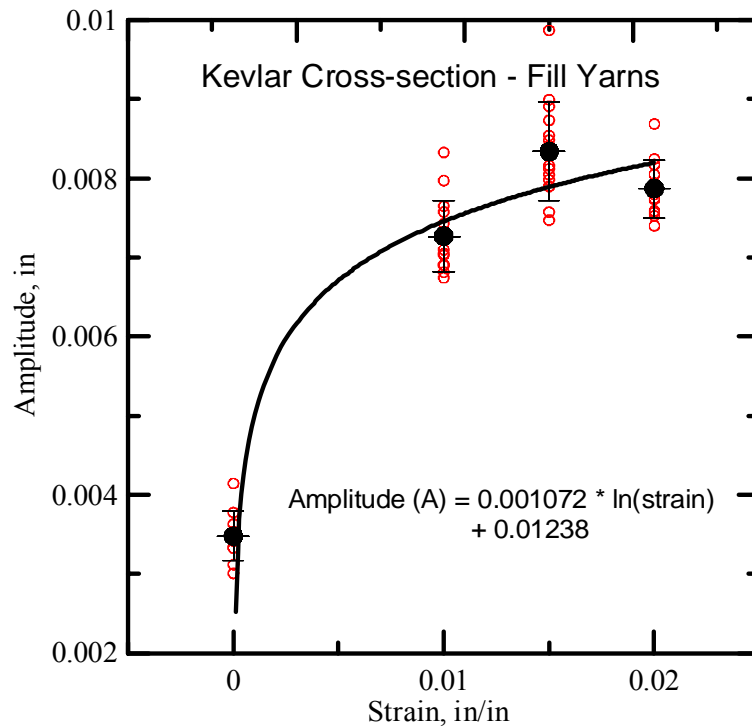


Figure 3.27. Comparison of Fill cross-section (sine curve) at different strain levels

Figure 3.28 shows the effect of warp yarn loading on sine curve representing longitudinal cross-section of fill yarn. A slight change in the period is observed this can be attributed to the reorientation of yarns under load. The equation representing this change can be represented as

$$\text{Period (P)} = -0.2368 * \text{strain} + 0.1173 \quad (3.6)$$

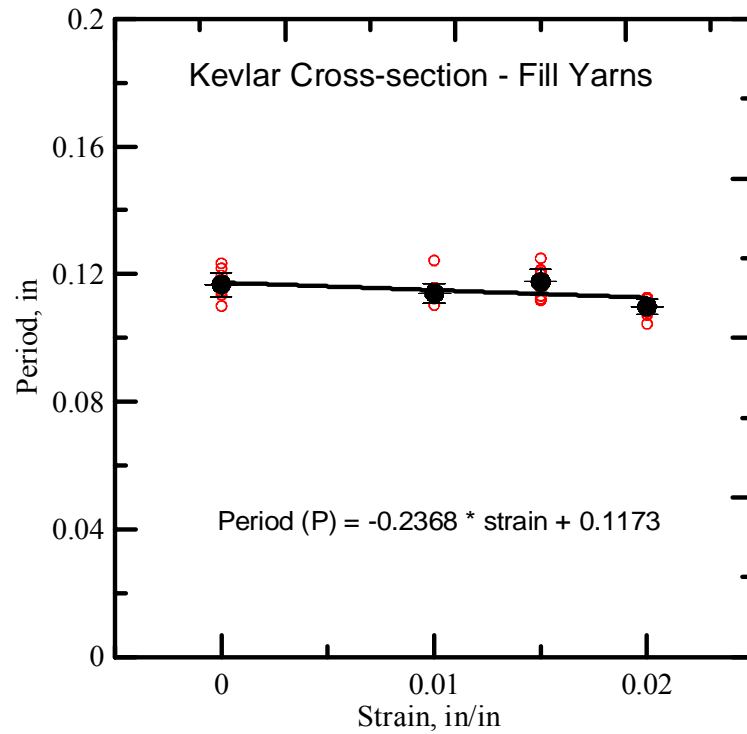


Figure 3.28. Comparison of Fill cross-section (sine curve) at different strain levels

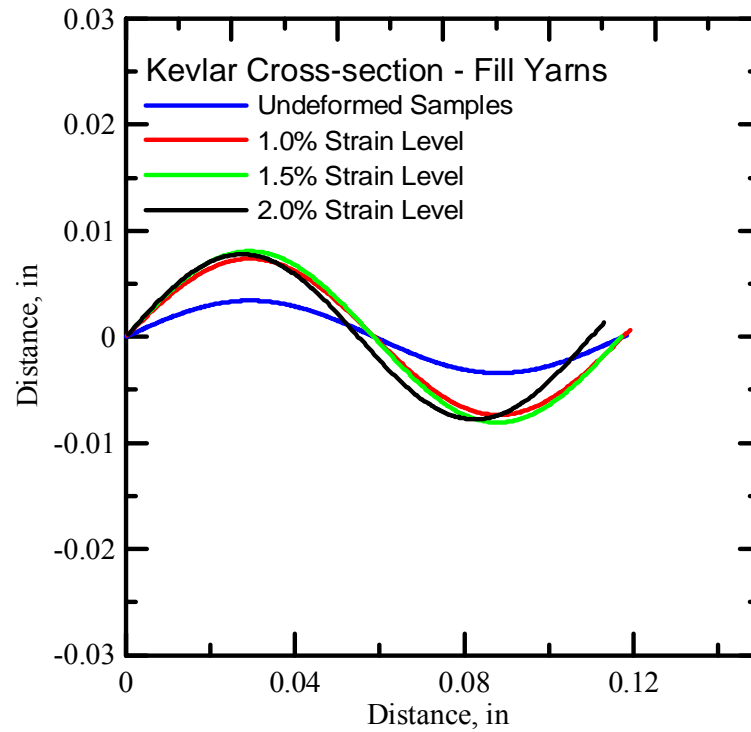


Figure 3.29. Comparison of Fill cross-section (sine curve) at different strain levels



### Warp Yarn - Transverse cross-section (Ellipse)

The images taken along transverse cross-section of warp yarns were used to estimate the parameters associated with the warp yarn cross-section and the effect of strain on the warp yarns. Figures 3.30 shows the undeformed geometry of the warp yarn where as Figure 3.31, 3.32 and 3.33 shows the effect of strain levels on the transverse geometry of the fill yarns.

It can be observed from these figures that as the loading increases, semi-major axis of the warp yarns decreases while semi-minor axis increases.

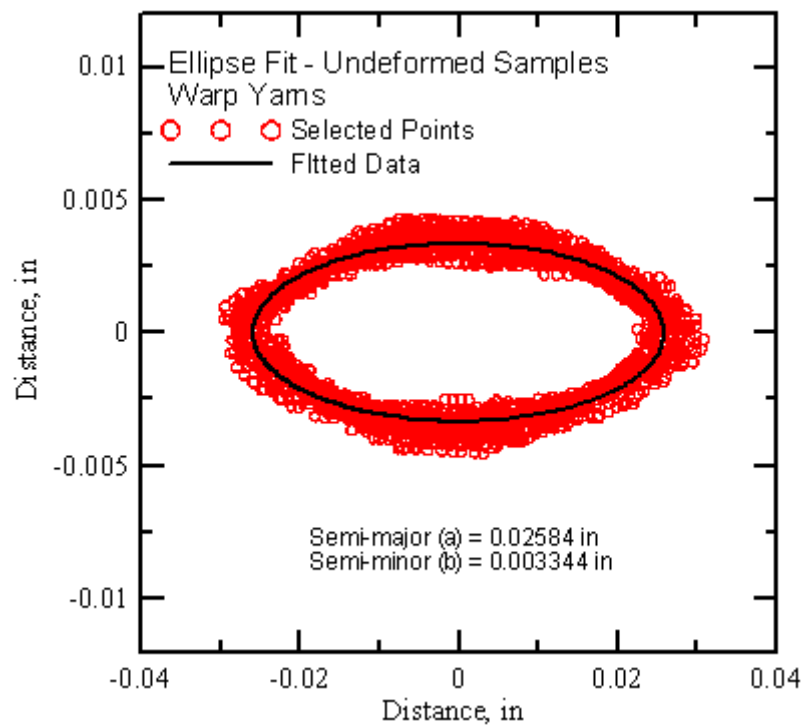


Figure 3.30. Warp cross-section (undeformed) ellipse fit through point cloud

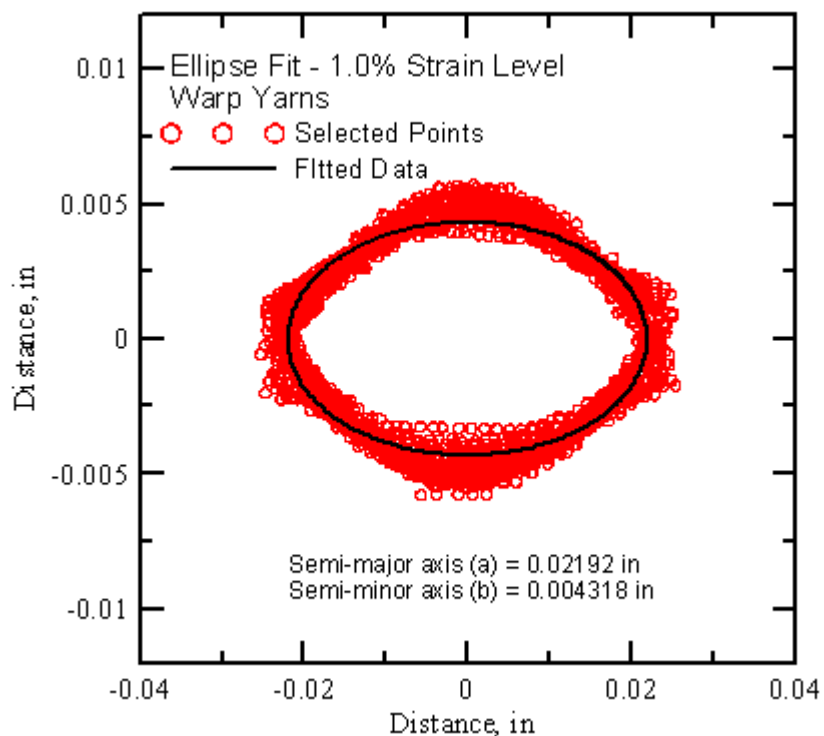


Figure 3.31: Warp cross-section (1.0% strain) ellipse fit through point cloud

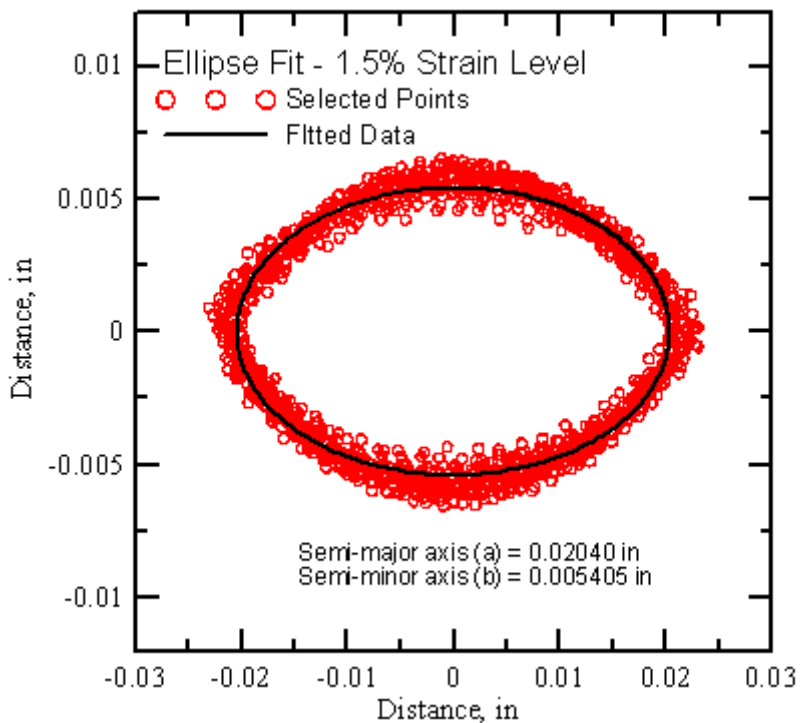


Figure 3.32. Warp cross-section (1.5% strain) ellipse fit through point cloud

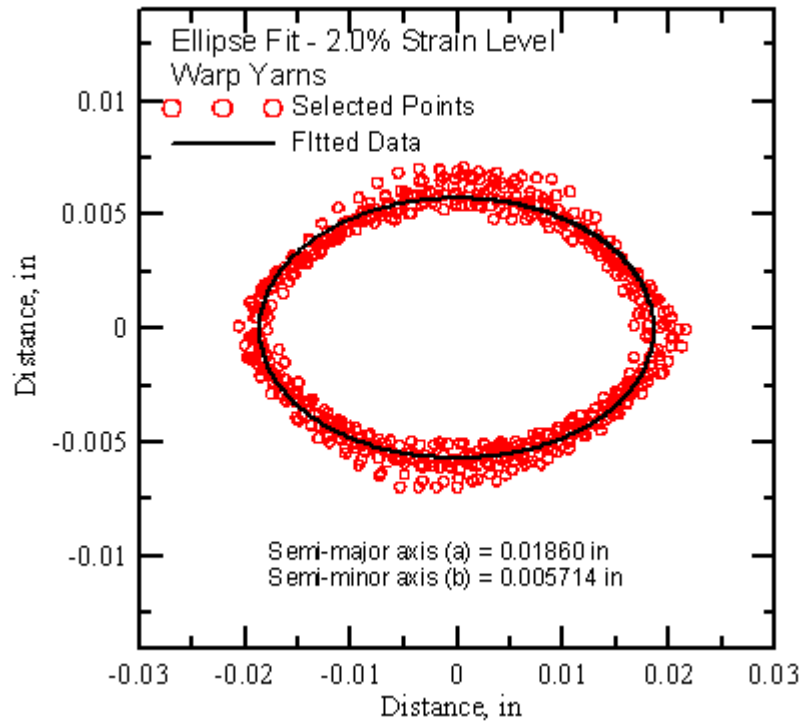


Figure 3.33. Warp cross-section (2.0% strain) ellipse fit through point cloud

Table 3.3 summarizes the parameters associated with the warp yarns for various loading conditions. The semi major axis (a) and semi minor axis (b) are shown for all samples at different strain levels. The parameters computed using point cloud approach is also shown in the table. It is interesting to note that as the strain level increases the major axis of warp yarns decreases while semi minor axis of yarns increases. This means the yarns becomes more and more circular with the increase in the strain level.

Table 3.3. Warp direction Elliptical curve parameters

Sample #	0.0% strain Level		1.0% Strain Level		1.5% Strain Level		2.0 % Strain Level	
	a (in)	b (in)	a (in)	b (in)	a (in)	b (in)	a (in)	b (in)
1	0.0235	0.0034	0.0232	0.0041	0.0198	0.0054	0.0178	0.0063
2	0.0256	0.003	0.0209	0.0042	0.0216	0.0049	0.0192	0.0055
3	0.0234	0.0037	0.0224	0.0042	0.0198	0.0056	0.0194	0.0063
4	0.0246	0.0036	0.0216	0.0041	0.0201	0.0054	0.019	0.0065
5	0.0262	0.0032	0.0228	0.0044	0.0194	0.0054	0.0178	0.006
6	0.0255	0.0034	0.0216	0.0041	0.0205	0.0055	0.0198	0.0051
7	0.0275	0.0029	0.0217	0.004	0.0195	0.0058	0.019	0.0051
8	0.0253	0.0035	0.0215	0.0041	0.0206	0.0054	0.0174	0.0058
9	0.0276	0.003	0.0213	0.0044	0.0207	0.0046	0.0181	0.0055
10	0.0237	0.0034	0.0224	0.0045	0.0205	0.0056	0.0188	0.0054
11	0.0277	0.003	0.0211	0.0045	0.0209	0.0053	0.0181	0.0056
12	0.0238	0.0033	0.021	0.0041	0.0201	0.0059		
13	0.0278	0.003	0.0228	0.0044	0.0197	0.0058		
14	0.0241	0.0035	0.0223	0.0043	0.0202	0.0051		
15	0.0282	0.0032	0.0213	0.0043	0.0202	0.0056		
16	0.0268	0.0033	0.0219	0.0047	0.0216	0.0057		
17	0.0282	0.0031	0.0227	0.0045	0.0199	0.006		
18	0.0262	0.0036	0.0209	0.0044	0.021	0.0058		
19	0.0241	0.0036	0.0206	0.0046	0.0213	0.0057		
20	0.024	0.0033	0.0225	0.0043	0.0213	0.0056		
<b>Average</b>	<b>0.02557</b>	<b>0.0033</b>	<b>0.02176</b>	<b>0.00432</b>	<b>0.02036</b>	<b>0.00547</b>	<b>0.01858</b>	<b>0.00574</b>
<b>Std Dev</b>	<b>0.00177</b>	<b>0.00024</b>	<b>0.0008</b>	<b>0.00019</b>	<b>0.00075</b>	<b>0.00037</b>	<b>0.00078</b>	<b>0.00048</b>
<b>using point cloud</b>	<b>0.02585</b>	<b>0.00335</b>	<b>0.02192</b>	<b>0.00432</b>	<b>0.0204</b>	<b>0.00541</b>	<b>0.0186</b>	<b>0.00571</b>

Figure 3.34 shows the effect of strain on the semi-major axis of the warp yarns. The semi-major axis of yarns increases with increase in the strain level. It is interesting to note that the effect of the loading on the semi-major axis can be represented by linear

curve. The effect of strain on the semi-major axis can be represented by following equation

$$\text{Semi-major axis (a)} = -0.364 * \text{strain} + 0.02572 \quad (3.7)$$

Figure 3.35 shows the effect of strain level on the semi-minor axis of the warp yarns. The semi-minor axis of the warp yarns increases as the strain level increases. The equation of the fitted curve describing strain effect on the yarn geometry can be represented using following equation

$$\text{Semi-minor(b)} = 0.124 * \text{strain} + 0.0033$$

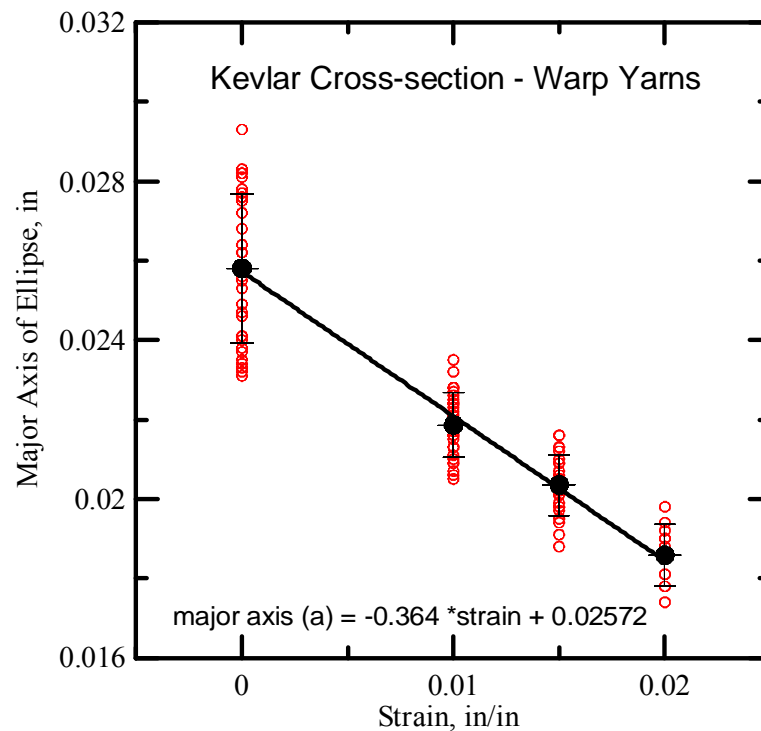


Figure 3.34. Comparison of Warp cross-section (ellipse) at different strain levels

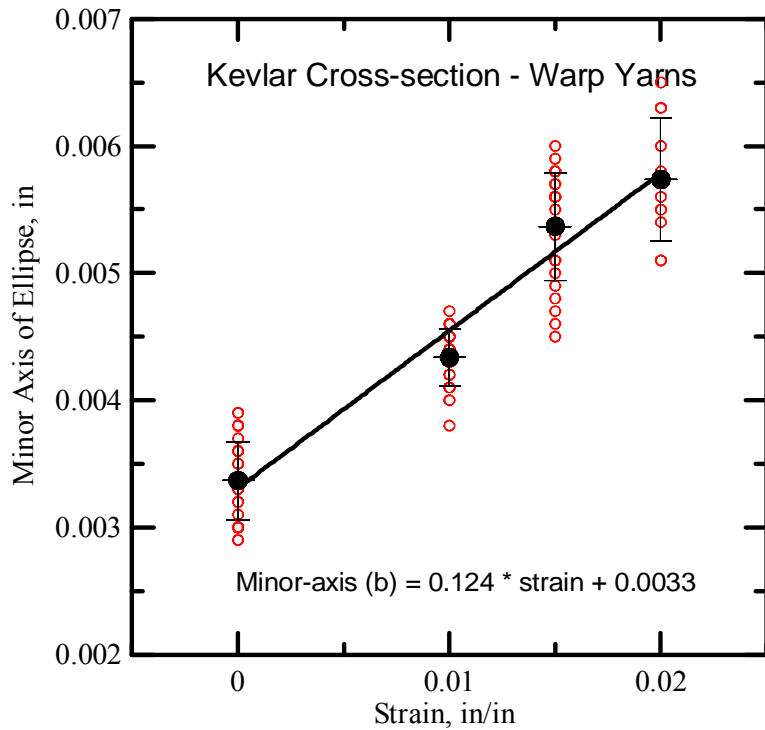


Figure 3.35. Comparison of Warp cross-section (ellipse) at different strain levels

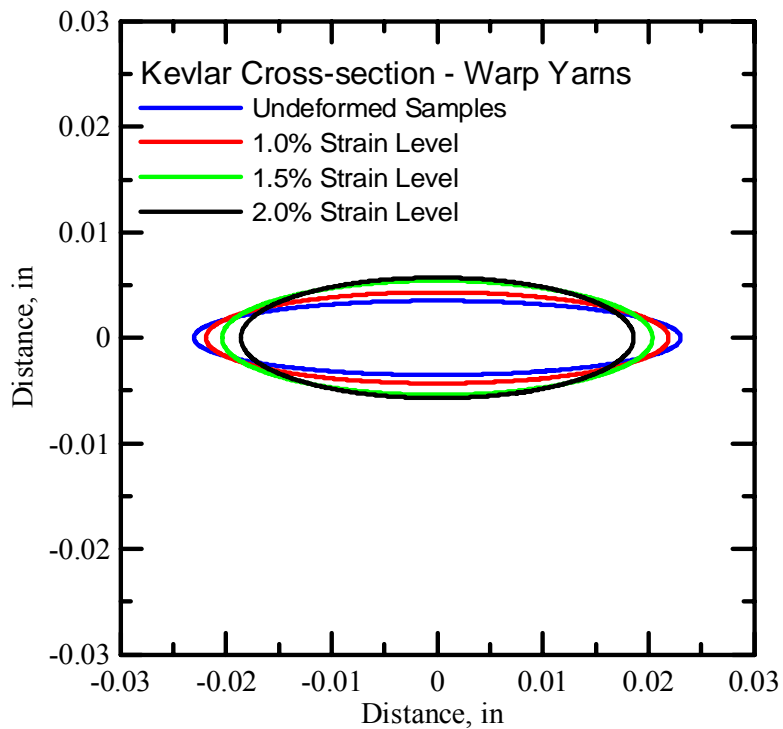


Figure 3.36. Comparison of Warp cross-section (ellipse) at different strain levels

Figure 3.36 shows the estimation of warp yarn transverse cross-section under loading. It is observed that as the strain level increases the semi-major axis of the yarns decreases significantly while there is increase in the semi-minor-axis of the yarns.

#### Warp Yarn - Longitudinal cross-section

The longitudinal geometry of warp yarns was analyzed and parameters associated with geometry were computed using images. Figure 3.38 shows undeformed geometry of warp yarn. As discussed earlier the undeformed warp yarns are follow sinusoidal curve and as these yarns are loaded they try to become flatter and approximately represents step function. So, deformed warp yarns are approximated using step function. Parameters associated with sinusoidal curve for undeformed geometry and step function for deformed geometry were computed and are listed in Table 3.4. The amplitude indicates the waviness or peak of the sine curve while period indicates the length of the complete sine curve. The length of the step function and height are also shown in the table. The amplitude and period associated with each sample was computed using image analysis and was plotted on a common scale. Curve fitted through all the points selected for various samples gives the overall estimation of parameters.

It can be observed that as the warp yarns are loaded they try to become flatter. This can be seen as removal of crimp due to the application of the load.

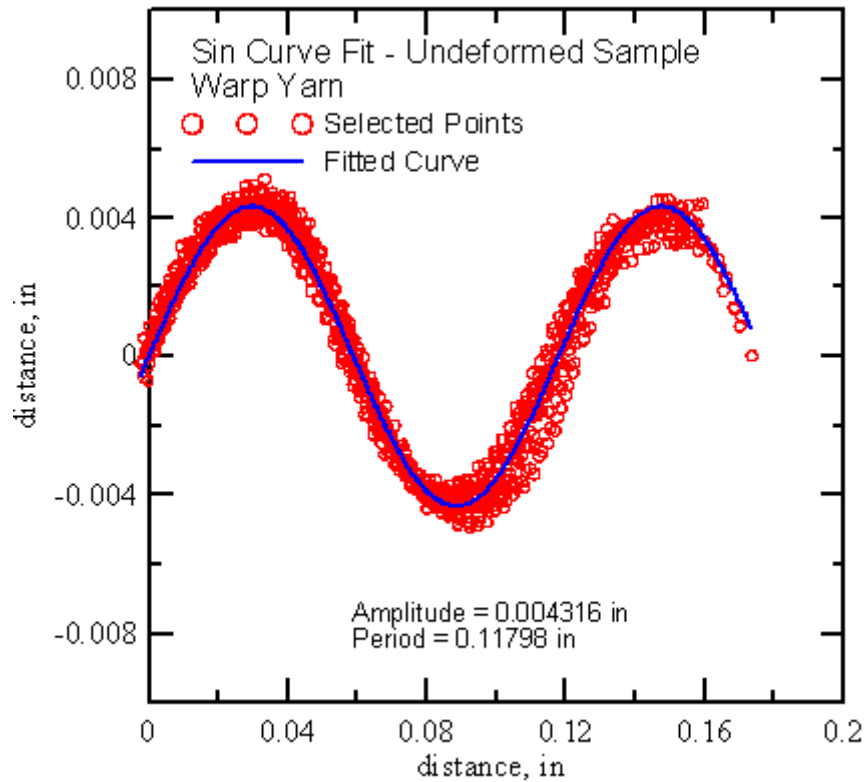


Figure 3.37. Warp cross-section (undeformed) sin curve fit through point cloud

Figure 3.38 shows the effect of the strain on the step height of the step function representing longitudinal cross-section of the warp yarns under load. It is observed that the warp yarns become flatter as they are loaded this can be seen by the decrease in step height of the step function. A curve fitted through step height at different strain levels can be used to estimate the step height for the intermediate strain levels. The equation of the fitted curve obtained is

$$\text{Step height} = 0.00079 + 0.329 \cdot \text{strain} - 16.23 \cdot (\text{strain})^2 \quad (3.8)$$



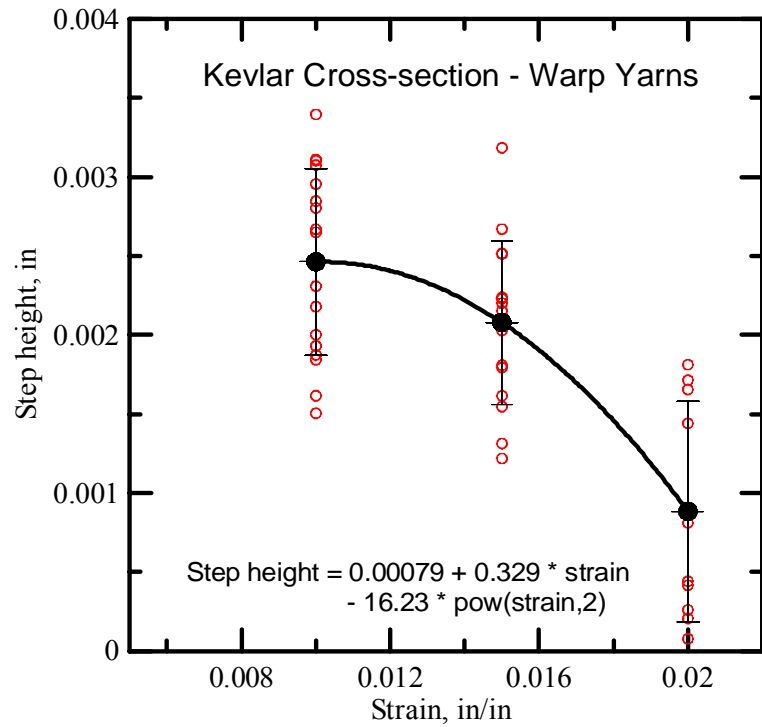


Figure 3.38. Warp cross-section (undeformed) sin curve fit through point cloud

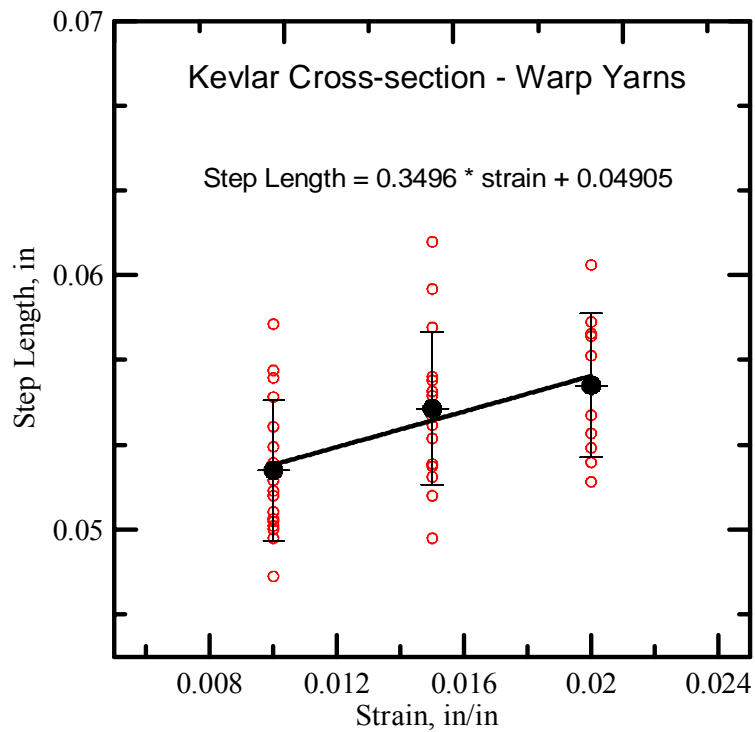


Figure 3.39. Warp cross-section (undeformed) sin curve fit through point cloud

Figure 3.39 shows the effect of strain on the step length. It is observed that as the strain level increases the step length also increases. The equation representing this change can be represented as

$$\text{Step length} = 0.3496 * \text{strain} + 0.04905 \quad (3.9)$$

Table 3.4. Warp direction Sine curve parameters

Sample #	undeformed		1.0% strain Level		1.5% Strain Level		2.0% Strain Level	
	Amplitude (in)	Period (in)	Step Length (in)	Step height (in)	Step Length (in)	Step height (in)	Step Length (in)	Step height (in)
1	0.00469	0.12107	0.05013	0.00231	0.05946	0.00251	0.05817	0.00144
2	0.00487	0.12256	0.05042	0.0034	0.05442	0.00267	0.0577	0.00171
3	0.00468	0.12299	0.04815	0.00307	0.05795	0.00318	0.05188	0.00181
4	0.0043	0.11615	0.04966	0.00193	0.05358	0.00223	0.0604	0.00041
5	0.00451	0.11574	0.05193	0.00311	0.05543	0.00179	0.0576	0.00165
6	0.00447	0.11807	0.05031	0.00265	0.05459	0.00203	0.05683	0.00081
7	0.00484	0.11899	0.05	0.00267	0.0541	0.00251	0.05321	0.00026
8	0.00425	0.1191	0.05626	0.00184	0.06131	0.00223	0.05264	0.00044
9	0.00434	0.11758	0.05152	0.002	0.05206	0.0022	0.05378	0.0002
10	0.00455	0.11613	0.05262	0.0031	0.04965	0.00215	0.05449	0.00008
11	0.00444	0.11788	0.05404	0.0028	0.05248	0.00181		
12	0.00388	0.11415	0.05808	0.00295	0.05526	0.00122		
13	0.00389	0.11705	0.05133	0.0015	0.05257	0.00161		
14	0.00407	0.11243	0.05069	0.00161	0.05586	0.00155		
15	0.00425	0.11539	0.05521	0.00285	0.056	0.00131		
<b>Average</b>	<b>0.00454</b>	<b>0.11875</b>	<b>0.05137</b>	<b>0.00263</b>	<b>0.055</b>	<b>0.0023</b>	<b>0.05567</b>	<b>0.00088</b>
<b>Std dev</b>	<b>0.00021</b>	<b>0.00252</b>	<b>0.00227</b>	<b>0.00054</b>	<b>0.0034</b>	<b>0.0004</b>	<b>0.00284</b>	<b>0.0007</b>

### Comparison of fill and warp yarns

The image analysis of longitudinal and transverse cross-section of warp and fill of Kevlar has shown that there is basic difference in the geometry of these two yarns. These differences can be attributed to the weave pattern and process of waving. Figure 3.41 and Figure 3.42 shows the comparison of transverse and longitudinal cross-section of fill and warp yarns.

From Figure 3.40 it can be observed that the warp yarns have greater semi-major axis while slightly less semi-minor axis as compared to fill yarns. So, initially warp yarns have more area of cross-section than fill yarns.

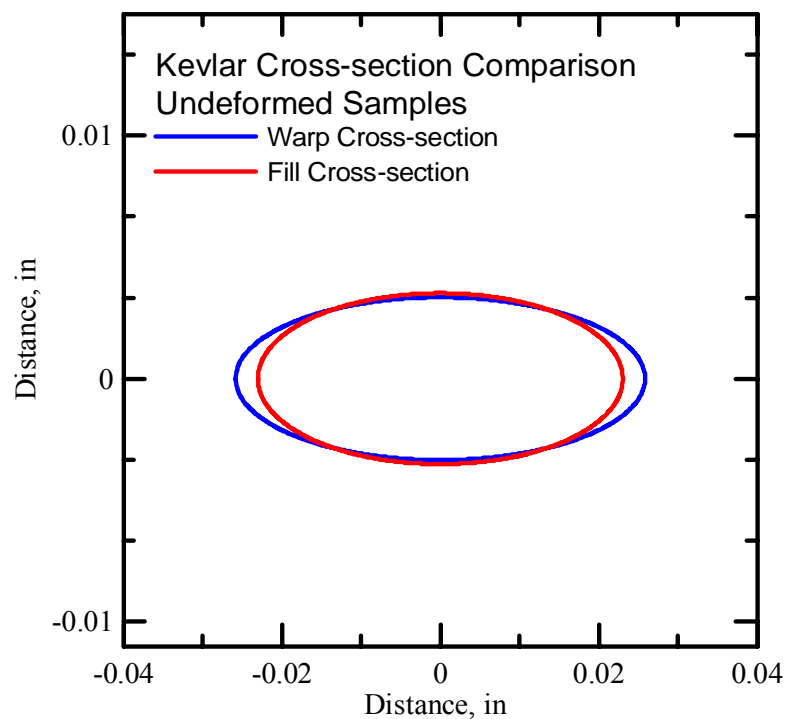


Figure 3.40. Comparison of Fill cross-section (ellipse) at different strain levels

Figure 3.41 shows the longitudinal cross-section of warp and fill yarns. It is interesting to note that both the yarns have same period this means both sides have same number of yarns per inch. The number of fill and warp yarns per inch of fabric computed based on period is approximately 17 which is same as manufacturer's specification. Further, the warp yarns has greater amplitude than the fill yarns or in other words warp yarns has greater slack than fill yarns this was also observed during the swath test in the warp and fill direction.

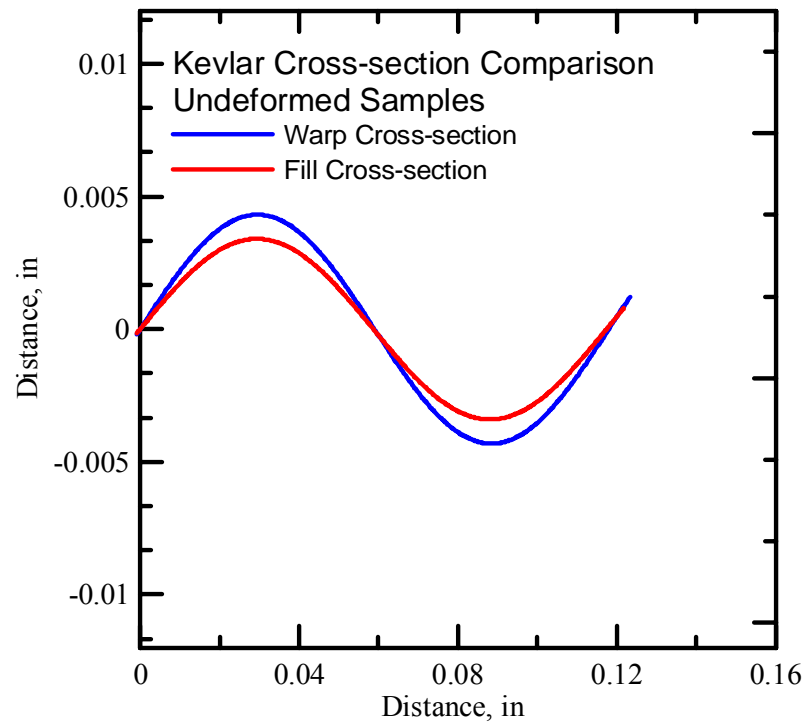


Figure 3.41. Comparison of Fill cross-section (ellipse) at different strain levels

### 3.3. Kevlar Single Yarn Tensile Tests

Objective of single yarn tensile tests are:-

- i) Understand the response of Kevlar single yarn under uniaxial tensile loading.
- ii) Provide estimation of Young's modulus in longitudinal direction.
- iii) Capture the effect of gage length on failure stress.

#### 3.3.1. Specimen preparation and fixture details

The samples for single yarn tensile tests were prepared by removing warp direction yarns from the woven fabric. Utmost care was taken to ensure that the yarns were removed without any damage. To remove the warp yarns following steps were taken

- i. Cut the length of the fabric based on gage length required for the test sample.
- ii. Cut the sample from sides along the warp direction of the fabric so as to remove stitches on the fabric sample.
- iii. Remove fill yarns from both ends of the fabric. This ensures easy removal of warp yarns.
- iv. Apply crazy glue on both sides of the warp yarns to allow removal of the yarns without any damage.
- v. After glue is dried remove the warp yarn one by one with care.

The single yarn test setup is shown in Figure 3.42. A low capacity load cell (300 lbf) was used to record the load value with good accuracy. A universal joint was connected to the testing frame to avoid any unwanted loading during the test. Universal

joint also helps in the alignment of yarn during test. To avoid any slipping of test sample during testing a special grip was used for these tests. As shown in the Figure 3.42 sample was first wrapped around the shaft before gripping using screws. It is important to keep samples perfectly vertical during the test. To check the sample orientation a laser beam was used during the test.

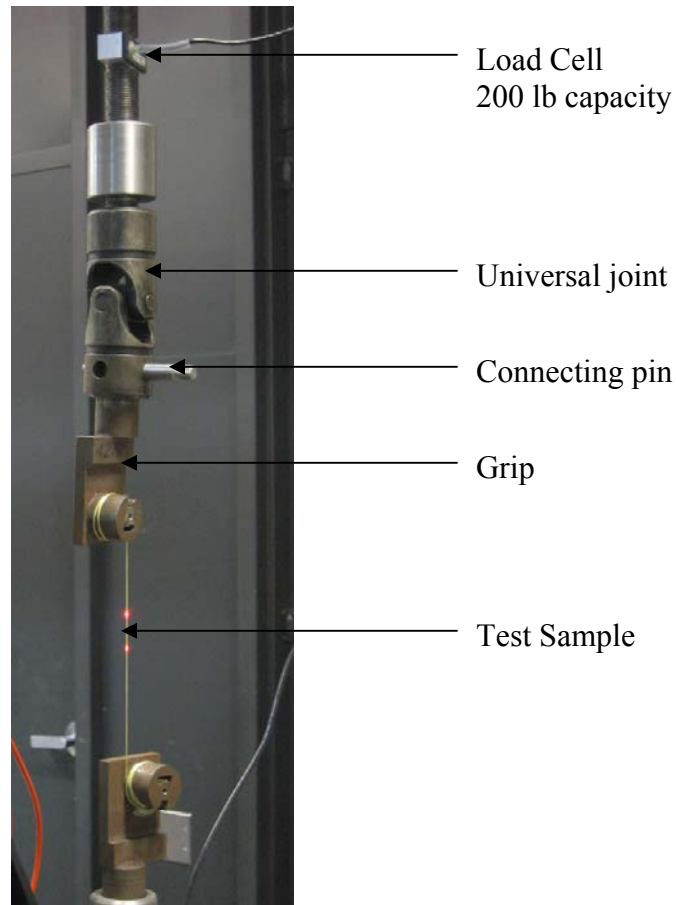


Figure 3.42. Single yarn test setup

### 3.3.2. Specimen Test Procedure

The single yarn test specimen tested on MTS test frame under displacement controlled condition such that the strain rate for the specimen is 0.025 /min. Six different

lengths of specimen were tested to ascertain the effect of gage length on the peak stress, young's modulus and strain at peak stress. Figure 3.43 shows the picture of specimen during testing.



(a) Sample before test



(b) Sample during test



(c) Sample during test



(d) Sample failed

Figure 3.43. Single yarn tensile test

To ensure that the specimen is perfectly straight during the test, a laser beam is used which was calibrated to be perfectly vertical using mercury levels. As shown in the

Figure 3.43 the specimen was not perfectly vertical before the test this is due to the tilt of the fixture in the presence of universal joint. However, as test proceeds and load start increasing the specimen aligned itself perfectly vertical. During the test the specimen remains vertical which can be confirmed by the laser light on the specimen. Table 3.5 shows the test plan used during single yarn tests. Six different lengths ranging from 2 in to 17 in were chosen and the strain rate during all the tests were maintained to be 0.025 /min. Stroke displacement rate was computed based on the length of the specimen. Total 10 replicates were tested for each gage length to ensure estimation of material parameters with good accuracy.

Table 3.5: Single yarn test plan

S.No.	Guage Length in	Strain rate /min	Stroke Disp. rate in/min	# Replicates	Total number of tests
1	2	0.025	0.05	10	10
2	5	0.025	0.125	10	10
3	8	0.025	0.2	10	10
4	11	0.025	0.275	10	10
5	14	0.025	0.35	10	10
6	17	0.025	0.425	10	10

### 3.3.3. Results and Discussion

#### 3.3.3.1 Kevlar Single Yarn Test Results

The stress-strain curve obtained from the test with gage length of 2 in is shown in Figure 3.44. The variation among the tests results is small which ensures repeatability of these tests. The young's modulus computed based on these tests is 22780 MPa, average



peak stress is 1899 MPa and strain at peak stress is estimated to be 0.12 mm/mm. Table 3.6 lists these parameters for all the samples.

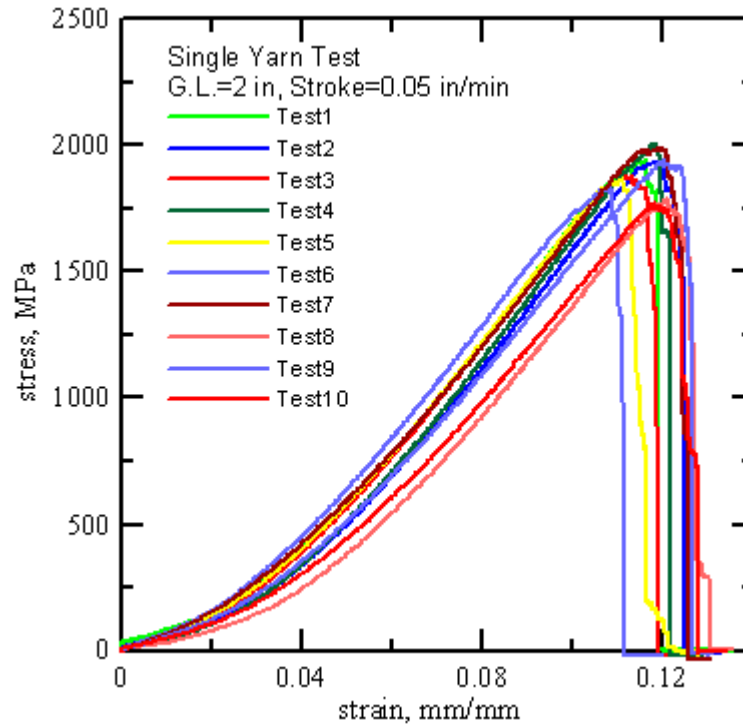


Figure 3.44. Stress Strain curves for G.L. = 2 in

The stress-strain curve obtained from the test with gage length of 5 in is shown in Figure 3.45 and that for gage length 8 in is shown in Figure 3.46. The variation among the tests results is small which ensures repeatability of these tests. The young's modulus computed for gage length 5 in is 43725 MPa, average peak stress is 1792 MPa and strain at peak stress is estimated to be 0.054 mm/mm. The young's modulus for gage length 8 in is 57913 MPa, peak stress is 1768 MPa and strain at Peak stress is 0.042.

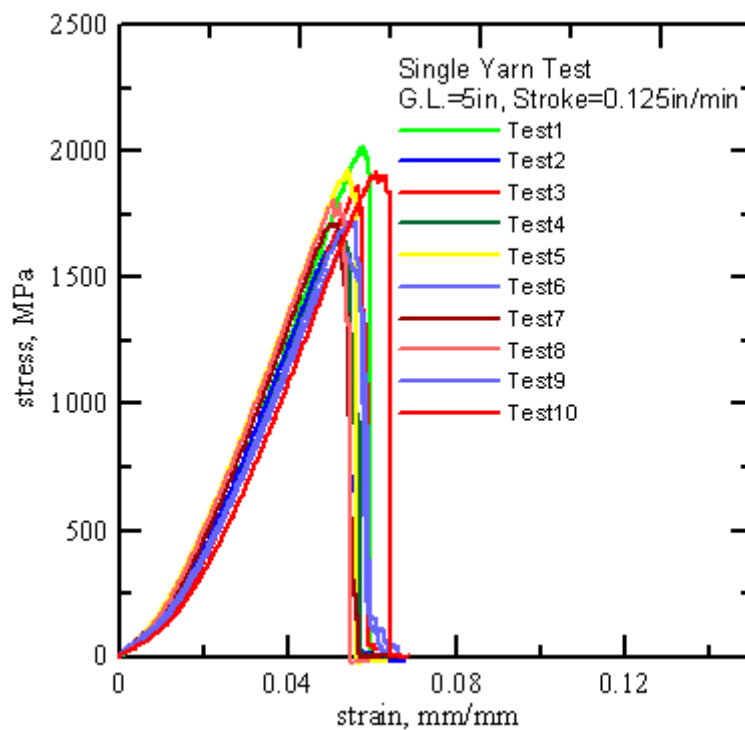


Figure 3.45. Stress Strain curves for G.L. = 5 in

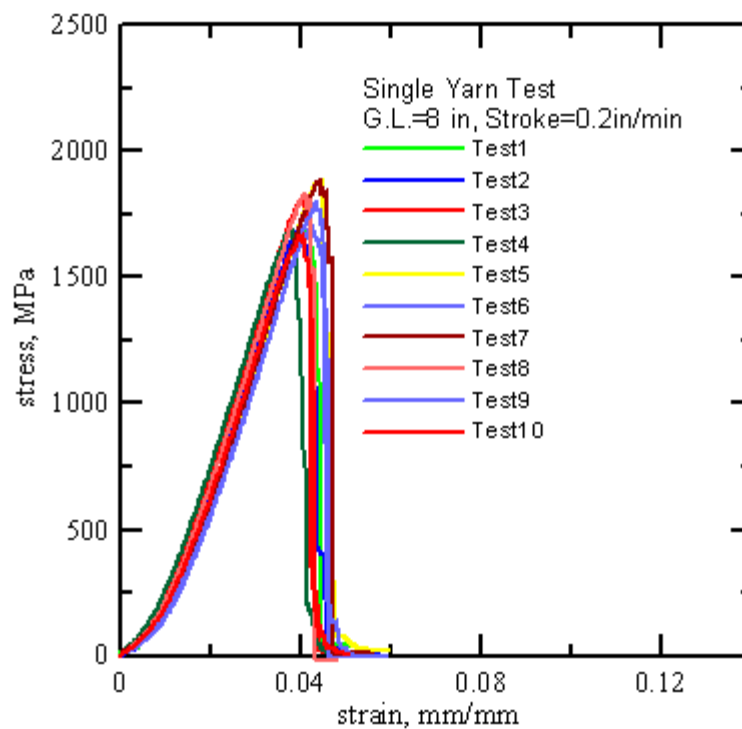


Figure 3.46. Stress Strain curves for G.L. = 8 in

The stress-strain curve obtained from the test with gage length of 11 in, 14 in and 17 in are shown in Figure 3.47, 3.48 and 3.49 respectively. The variation among the tests results is small which ensures repeatability of these tests. The young's modulus computed for gage length 11 in is 67161 MPa, average peak stress is 1698 MPa and strain at peak stress is estimated to be 0.034 mm/mm. The young's modulus for gage length 14 in is 73790 MPa, peak stress is 1674 MPa and strain at Peak stress is 0.029. The young's modulus for gage length 17 in is 77440 MPa, peak stress is 1587 MPa and strain at Peak stress is 0.026.

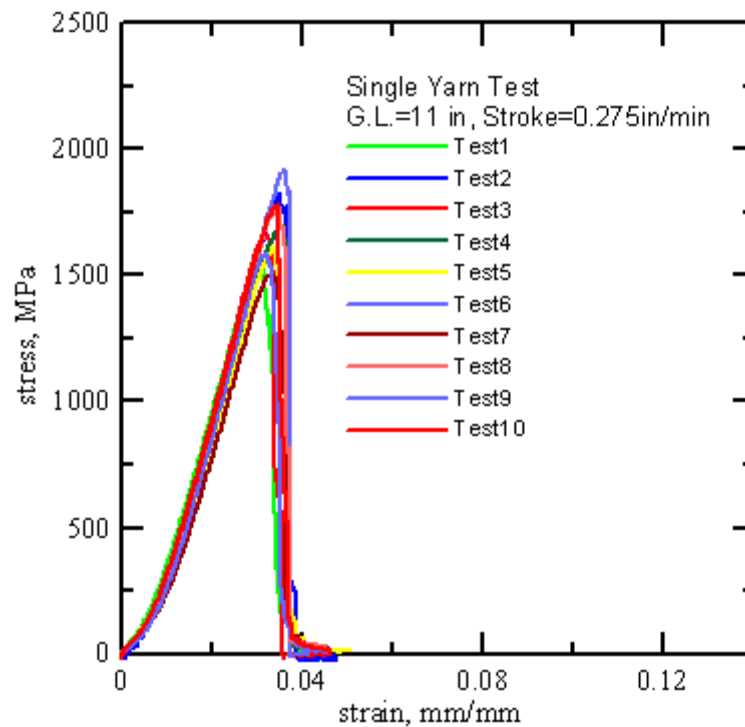


Figure 3.47. Stress Strain curves for G.L. = 11 in

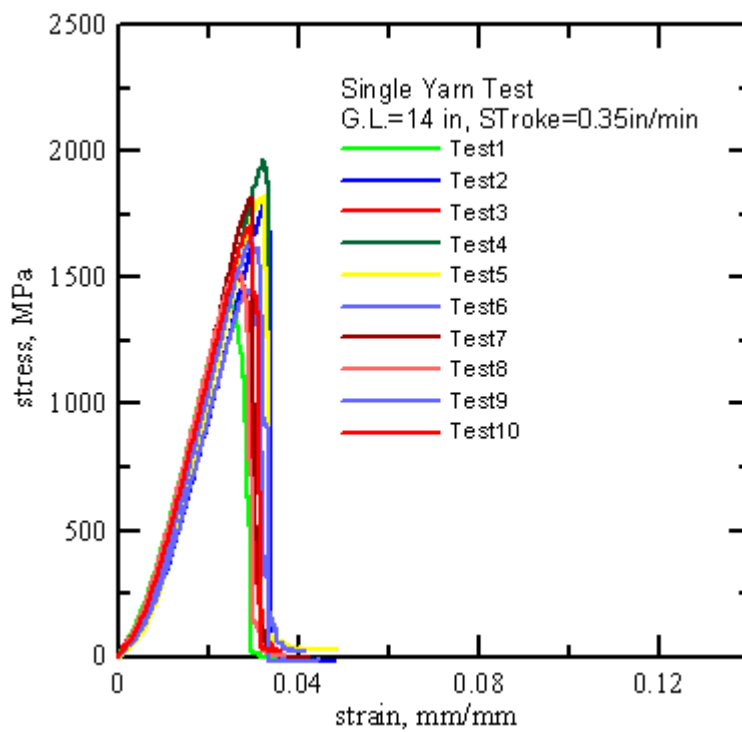


Figure 3.48. Stress Strain curves for G.L. = 14 in

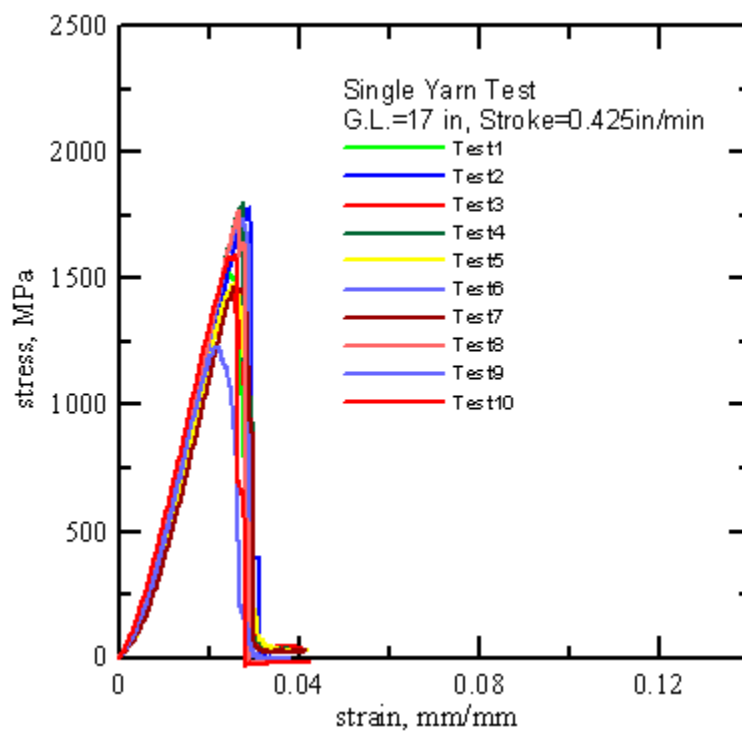


Figure 3.49. Stress Strain curves for G.L. = 17 in

Table 3.6: Single yarn test results

Sample #	2 in Length Sample			5 in Length Sample			8 in Length Sample		
	E (MPa)	max stress (Mpa)	strain at max stress	E (MPa)	max stress (Mpa)	strain at max stress	E (MPa)	max stress (Mpa)	strain at max stress
1	23711.6	1954.3	0.120	46194.3	2021.8	0.060	58214.9	1692.7	0.040
2	23398.8	1939.0	0.120	42714.7	1665.8	0.050	58664.6	1696.3	0.040
3	22766.8	1889.3	0.110	44289.1	1863.4	0.060	58782.8	1810.0	0.040
4	24011.9	2008.5	0.120	43196.3	1660.8	0.050	57636.6	1690.0	0.040
5	23054.7	1870.2	0.110	44575.6	1931.1	0.050	59839.1	1893.2	0.040
6	22732.0	1834.7	0.110	41057.7	1600.7	0.050	55753.6	1701.9	0.040
7	22826.2	1993.9	0.120	44323.1	1715.4	0.050	56918.0	1888.6	0.040
8	22215.3	1786.6	0.120	45099.0	1812.0	0.050	58943.4	1835.8	0.040
9	21839.2	1942.2	0.120	42573.4	1728.4	0.060	57382.9	1809.1	0.040
10	21244.8	1770.0	0.120	43235.6	1925.3	0.060	57000.3	1669.9	0.040
<b>Max</b>	24011.9	2008.5	0.120	46194.3	2021.8	0.060	59839.1	1893.2	0.040
<b>Min</b>	21244.8	1770.0	0.110	41057.7	1600.7	0.050	55753.6	1669.9	0.040
<b>Mean</b>	<b>22780.1</b>	<b>1898.8</b>	<b>0.120</b>	<b>43725.9</b>	<b>1792.5</b>	<b>0.050</b>	<b>57913.6</b>	<b>1768.7</b>	<b>0.040</b>
<b>std Dev.</b>	<b>843.9</b>	<b>82.9</b>	<b>0.005</b>	<b>1466.9</b>	<b>139.5</b>	<b>0.005</b>	<b>1203.1</b>	<b>87.7</b>	<b>7E-18</b>

Table 3.7: Single yarn test results

Sample #	11 in Length Sample			14 in Length Sample			17 in Length Sample		
	E (MPa)	max stress (Mpa)	strain at max stress	E (MPa)	max stress (Mpa)	strain at max stress	E (MPa)	max stress (Mpa)	strain at max stress
1	63597.1	1579.4	0.030	73666.2	1445.4	0.020	76422.7	1526.0	0.020
2	68086.5	1836.8	0.040	71261.5	1807.6	0.030	77380.4	1784.8	0.030
3	68291.5	1674.1	0.030	73638.4	1506.4	0.030	74120.1	1455.6	0.030
4	65664.2	1704.1	0.040	76319.4	1966.0	0.030	81335.1	1802.9	0.030
5	66710.8	1617.1	0.030	76175.0	1825.1	0.030	76827.5	1479.7	0.030
6	69849.1	1922.0	0.040	67718.5	1456.3	0.030	82475.1	1744.9	0.030
7	64244.0	1507.0	0.030	76409.5	1823.0	0.030	74790.5	1471.4	0.030
8	69176.9	1774.1	0.030	75011.8	1541.8	0.030	80878.5	1769.0	0.030
9	68349.4	1587.2	0.030	73192.1	1663.1	0.030	73006.5	1236.2	0.020
10	67642.7	1783.9	0.030	74517.7	1708.7	0.030	77162.6	1597.3	0.030
<b>Max</b>	69849.1	1922.0	0.040	76409.5	1966.0	0.030	82475.1	1802.9	0.030
<b>Min</b>	63597.1	1507.0	0.030	67718.5	1445.4	0.020	73006.5	1236.2	0.020
<b>Mean</b>	<b>67161.2</b>	<b>1698.6</b>	<b>0.030</b>	<b>73791.0</b>	<b>1674.3</b>	<b>0.030</b>	<b>77439.9</b>	<b>1586.8</b>	<b>0.030</b>
<b>std Dev.</b>	<b>2074.2</b>	<b>130.2</b>	<b>0.0048</b>	<b>2679.6</b>	<b>180.9</b>	<b>0.003</b>	<b>3189.1</b>	<b>186.5</b>	<b>0.004</b>

### 3.3.3.2 Gage length effect

Figure 3.50 shows the stress strain curves of single yarn tensile test for gage lengths 2in, 5in, 8in, 11in, 14in and 17in. It can be observed that as the gage length increases the young's modulus of the yarn increases while peak stress reduces significantly. The reduction in the peak stress with increase in the gage length can be attributed to the increase in imperfection with the increase in gage length. A quantitative analysis of gage length effect is shown in next section where weibull curve fitting analysis is carried out to understand the effect of gage length and corresponding weibull parameters.

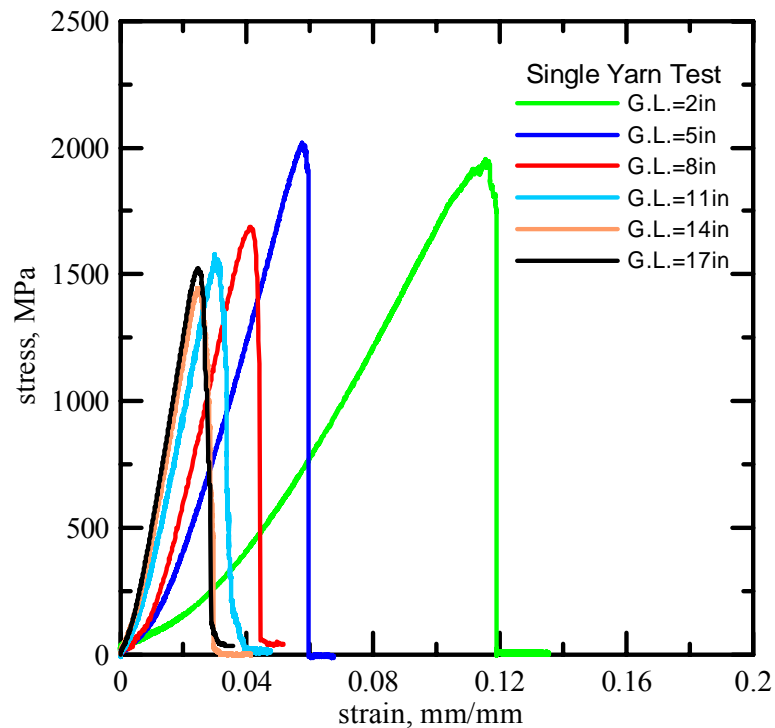


Figure 3.50. Peak Stress vs gauge length

Figure 3.51 shows the effect of gage length on peak stress. A perfectly linear relation between the peak stress and gage length is observed. The line fitted through the average of all the samples for each gage length can be represented by the equation

$$\text{Peak Stress} = -19 * (\text{Gage Length}) + 1916 \quad (3.10)$$

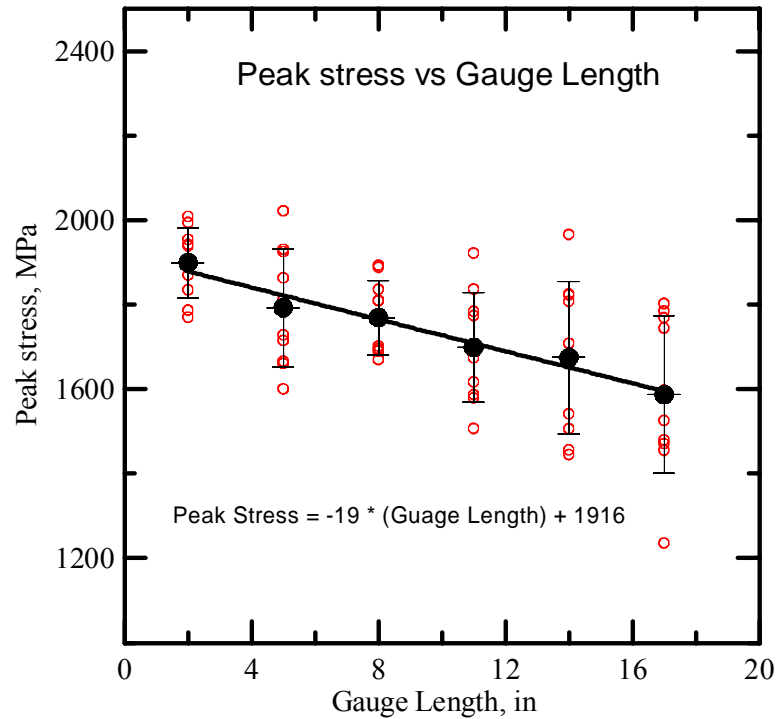


Figure 3.51. Peak Stress vs gauge length

Figure 3.52 and Figure 3.53 shows the effect of gage length on young's modulus and strain at peak stress. It is observed that as gage length increases young's modulus of the yarns increases and strain at peak stress decreases. Polynomial curve of degree two can be used to define the effect of gage length on the young's modulus and log curve can be used to define its effect of the strain at peak stress.

$$\text{Young's modulus} = 8590 + 7950 * (\text{gage length}) - 231 (\text{gage length})^2 \quad (3.11)$$

$$\ln(\text{strain at peak stress}) = -0.7 * \ln(\text{gage length}) - 1.7 \quad (3.12)$$

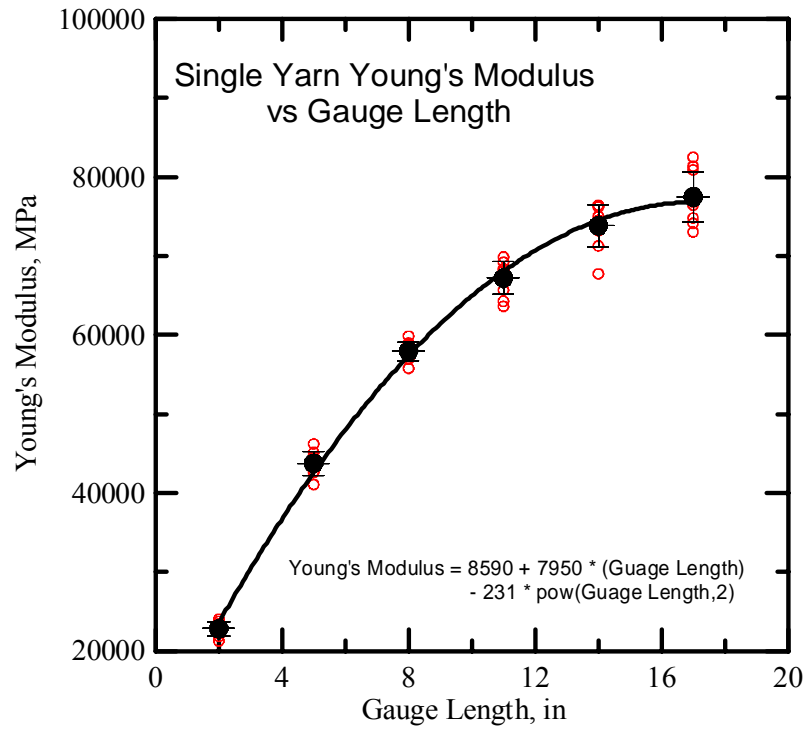


Figure 3.52. Young's Modulus vs gauge length

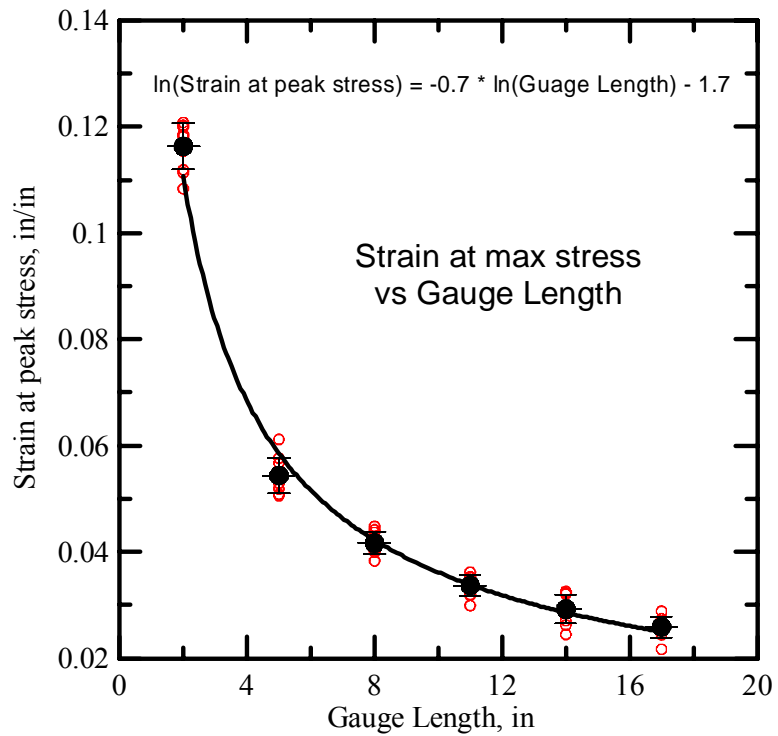


Figure 3.53. Strain at peak stress vs gauge length



### 3.3.4. Weibull Analysis

#### 3.3.4.1 Introduction

The classical way to view the strength of the materials or structures is a deterministic one. That is, a true strength, a single value that is characteristic of the material or structure, is supposed to exist. In experiments to determine this true strength, considerable scatter in the results is usually observed. As this is not considered to be a feature of the material or object itself, it is usually attributed to uncontrollable experimental variables. As a consequence, the second central moment of the experimental data, the standard deviation, is interpreted as indicating the success of standardizing the experimental set-up and procedures. Therefore, standard deviation can be considered to be an indicator of the quality of an experiment or testing method.

The deterministic view has become much less popular in the technical sciences. If the deterministic view is valid, identical experiments performed on material specimens of different sizes should yield the same results for failure stress. However, it has been shown that for Kevlar yarns, larger specimens have a lower failure stress compared to smaller ones. These systematic differences cannot be explained by random variations in experimental procedures, but by imperfections included in the yarn structure. Flaws can cause a material to fail long before its ideal strength is reached. Although this ideal strength might be interpreted as true strength, for practical purposes it is of more importance to understand the actual strength of the material than true strength. It is more logical, therefore to accept imperfections as an integral part of a material or structure and to account for their presence when describing its strength. The distribution of

imperfections within a structure is of a probabilistic nature. As a consequence, the strength of the structure itself is of a probabilistic nature. The Weibull analysis is widely used for this purpose and is used here to explain variation in Kevlar strength as a function of gage length.

The basic form of the weibull equation for cumulative probability density is:

$$P(\sigma)=1-\exp\left[-\left(\frac{\sigma}{\sigma_0}\right)^m\right] \quad (3.13)$$

Where  $\sigma$  is the failure stress and  $\sigma_0$  and  $m$  are the parameters of the distribution.  $\sigma_0$  is the reference or scaling value related to the mean and  $m$  is the weibull modulus or shape parameter.

In order to include the length effect in the Weibull model parameters related to gage length or volume of the yarns can be introduced in the model. The modified weibull equation for cumulative probability density is give by:-

$$P(\sigma)=1-\exp\left[-\left(\frac{v}{v_0}\right)\left(\frac{\sigma}{\sigma_0}\right)^m\right] \quad (3.14)$$

Where  $v$  represents the volume of the yarn and  $v_0$  represents the scaling value for the volume.

#### 3.3.4.2 Results and Discussion

The single yarn tensile data was used for weibull curve fitting. The data obtained by single yarn tensile tests is shown in Table 3.8. To implement weibull equation to the experimental test data, MATLAB code was written. Weibull parameters were computed

by fitting Cumulative probability distribution of the test data in least square sense. The weibull parameters thus obtained are shown in Table 3.9.

Table 3.8: Single yarn test data

Replicate #	Peak Stress, psi					
	2 in	5 in	8 in	11 in	14 in	17 in
1	283451.9	293240.1	245509.7	229079.0	209638.3	221327.6
2	281222.6	241605.7	246030.4	266398.9	262166.7	258862.4
3	274014.4	270257.4	262517.5	242805.2	218487.3	211109.3
4	291305.1	240881.5	245113.7	247161.8	285137.9	261487.7
5	271242.0	280079.7	274580.3	234533.3	264701.5	214617.3
6	266093.2	232156.9	246833.6	278767.2	211211.2	253068.6
7	289189.1	248791.3	273912.7	218577.9	264395.9	213406.6
8	259122.8	262811.6	266263.0	257312.2	223613.4	256576.6
9	281686.7	250681.0	262381.6	230199.3	241209.6	179289.1
10	256712.5	279242.2	242194.2	258726.6	247818.1	231670.4

Figure 3.55 shows the weibull curve fitting to experimental data using least square method. As it can be observed there is basic difference in the cumulative probability plots for different lengths. As the gage length of the sample increases the cumulative probability plot shifts towards lower stress values, which is clear indicator of dependence of peak stress on the gage length.

Table 3.9: Weibull parameters

Weibull Parameter		Gage Lengths					
		2 in	5 in	8 in	11 in	14 in	17 in
$\sigma_0$		280130	265140	260160	249790	250160	239370
$m$		21.7	11.5	14.3	11.9	7.9	8.8

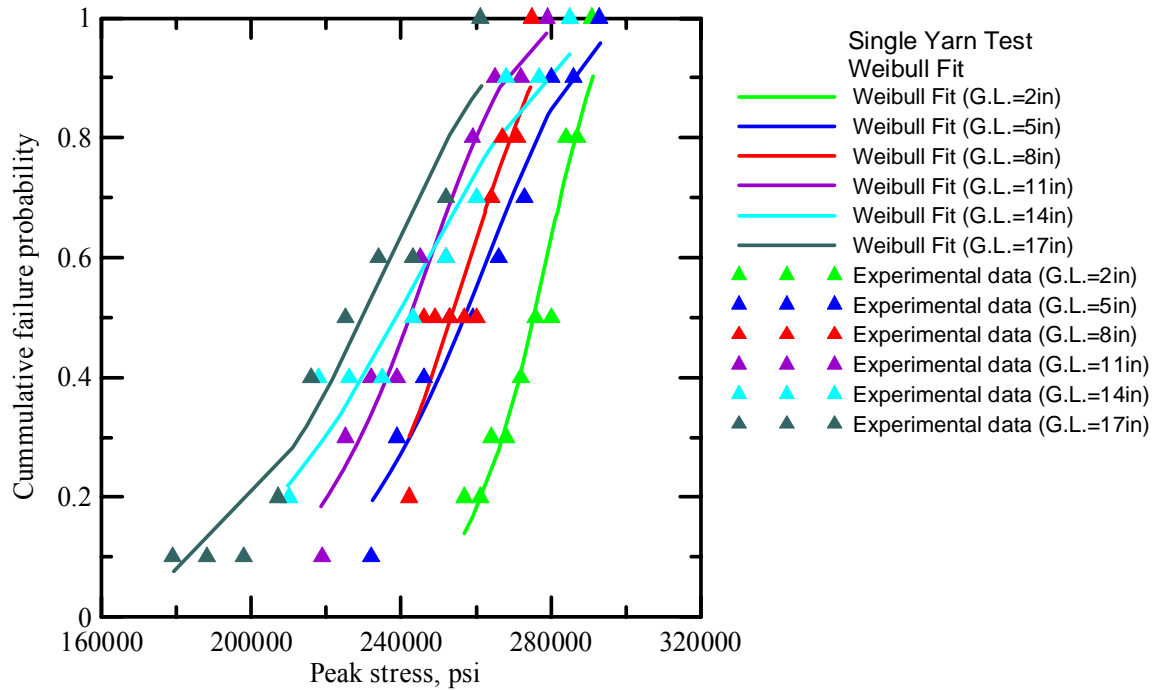


Figure 3.54. Comparison of cumulative failure probability vs peak stress for different gage lengths

## 4. MICRO-MECHANICAL MODEL OF KEVLAR

This chapter explains the micro-mechanical model of Kevlar fabric developed using the experimental results discussed in chapter 3. The process starts with building a 3-D model of Kevlar yarns based on actual measurements of geometry parameters obtained via photomicrographs of sectioned fabric and combining it with material model which is based on yarn level laboratory testing. The material model of Kevlar yarns was incorporated in LS-DYNA using user defined material model (UMAT) written in FORTRAN. The model was verified by comparing simulation results of Single yarn tensile tests and swatch tensile tests with experimental data. The result shows good relation with experimental results. The micro-mechanical model thus developed can be used to determine their mechanical properties via Virtual Testing.

### 4.1. GEOMETRIC MODEL

#### 4.1.1. Unit Cell Development

A Kevlar fabric can be built by replicating a smallest unit known as unit cell. The unit cell model of the Kevlar was developed by using the geometric parameters computed using sectioned Kevlar. The fill and warp direction yarns were assumed to have elliptical cross-section which follows sinusoidal path. The computed parameters associated with Kevlar geometry is shown in table 4.1.

Table 4.1: Geometry Parameters

	Transverse Cross-section - Elliptical Cross-section		Longitudinal Cross-section - Sinusoidal Path	
	Semi - major axis (a), in	Semi - minor axis (b), in	Period, in	Amplitude, in
Warp Yarn	0.02584	0.003345	0.117981	0.004316
Fill Yarn	0.023059	0.003511	0.117415	0.003405

The parameters shown in Table 4.1 were used to build 3-D model of unit cell. An elliptical curve representative of yarn transverse cross-section was first modeled using semi-minor and semi-major axis dimensions which is then extruded along the sinusoidal path represented by amplitude and period values. As shown in the table the geometric dimensions of yarn are essentially direction dependent. UG NX 4.0 was used to build the geometric modeling of the yarns.

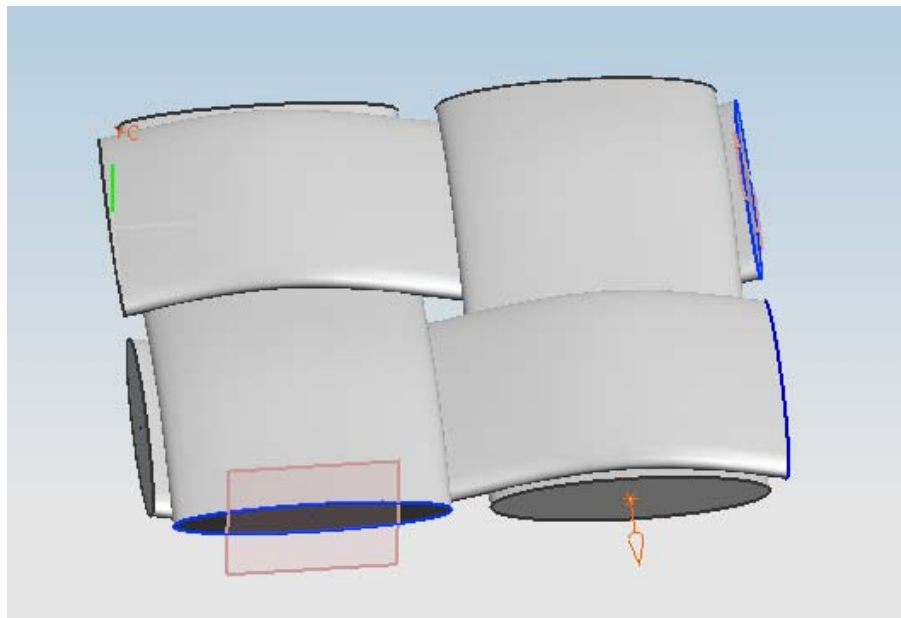


Figure 4.1. Unit cell Model

To ensure numerical stability and avoid any undue stresses in the model, the initial geometry should not have intersecting bodies or surfaces. Initial penetrating surfaces results in undue interfacial stresses and can lead to unstable model during simulations. The unit cell model developed using above methodology was checked for penetrations. Initial penetration was removed by modifying the cross-section and sinusoidal curve parameters. This was achieved by changing amplitude of the sine curve. Table 4.2 shows the parameters used to develop geometric model of the Kevlar fabric.

Table 4.2: Modified geometry parameters

	Transverse Cross-section - Elliptical Cross-section		Longitudinal Cross-section - Sinusoidal Path	
	Semi - major axis (a), in	Semi - minor axis (b), in	Period, in	Amplitude, in
Warp Yarn	0.02580	0.00334	0.11798	0.00481
Fill Yarn	0.02304	0.00351	0.11742	0.00380

#### 4.1.2. Swatch Model Generation

A swatch model can be generated by replicating unit cell in warp and fill directions. The number of warp and fill direction unit cells can be computed by dividing required length by length of the unit cell in the respective direction. The swatch model thus created is shown in Figure 4.2.

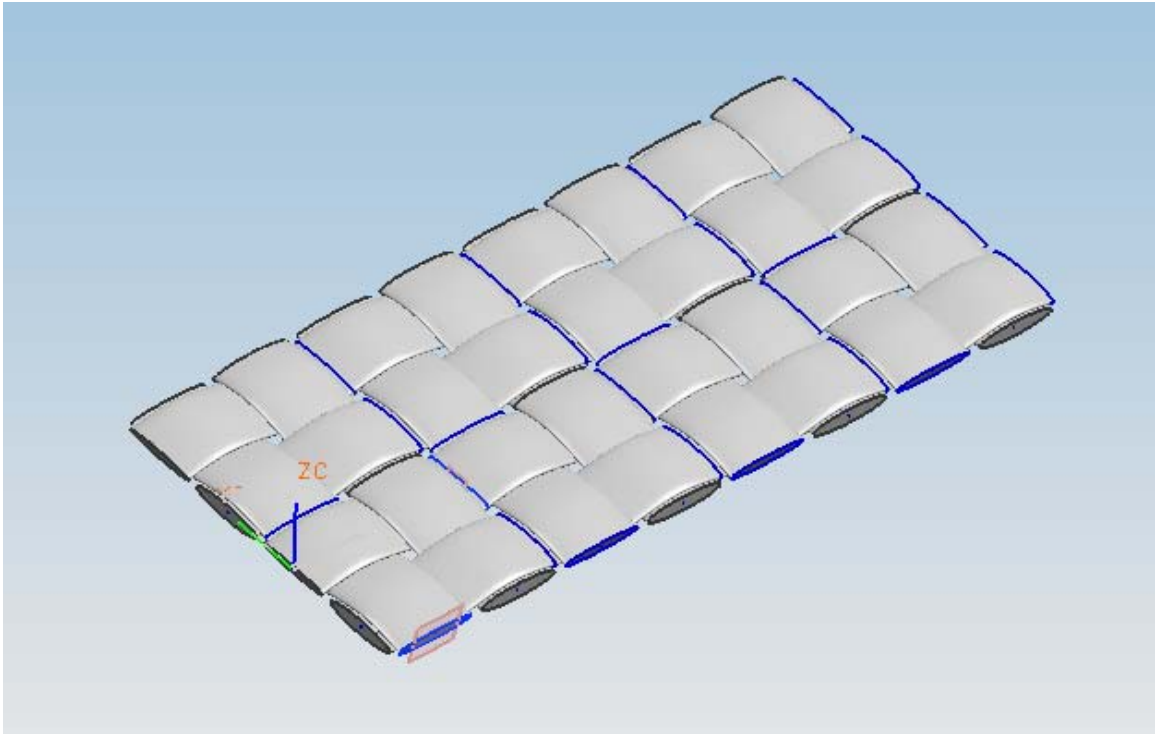


Figure 4.2. Swatch Model

## 4.2. MATERIAL MODEL DESCRIPTION

### 4.2.1. Kevlar Yarn Constitutive Behavior

The constitutive model that most accurately describes the yarn's behavior is orthotropic. The constitutive relation of Kevlar yarns can be represented as shown in equation (4.1). The inverse constitutive law which relates stress increments in term of strain increments can be represented by equation (4.2).



$$\begin{bmatrix} \Delta \varepsilon_{11} \\ \Delta \varepsilon_{22} \\ \Delta \varepsilon_{33} \\ \Delta \varepsilon_{23} \\ \Delta \varepsilon_{31} \\ \Delta \varepsilon_{23} \end{bmatrix} = \begin{bmatrix} \frac{1}{E_1} & \frac{-\nu_{21}}{E_2} & \frac{-\nu_{31}}{E_3} & 0 & 0 & 0 \\ \frac{-\nu_{12}}{E_1} & \frac{1}{E_2} & \frac{-\nu_{32}}{E_3} & 0 & 0 & 0 \\ \frac{-\nu_{13}}{E_1} & \frac{-\nu_{23}}{E_2} & \frac{1}{E_3} & 0 & 0 & 0 \\ 0 & 0 & 0 & \frac{1}{2G_{23}} & 0 & 0 \\ 0 & 0 & 0 & 0 & \frac{1}{2G_{31}} & 0 \\ 0 & 0 & 0 & 0 & 0 & \frac{1}{2G_{12}} \end{bmatrix} \begin{bmatrix} \Delta \sigma_{11} \\ \Delta \sigma_{22} \\ \Delta \sigma_{33} \\ \Delta \sigma_{21} \\ \Delta \sigma_{31} \\ \Delta \sigma_{12} \end{bmatrix} \quad (4.1)$$

$$\begin{bmatrix} \Delta \sigma_{11} \\ \Delta \sigma_{22} \\ \Delta \sigma_{33} \\ \Delta \sigma_{23} \\ \Delta \sigma_{31} \\ \Delta \sigma_{12} \end{bmatrix} = \begin{bmatrix} \frac{1-\nu_{23}\nu_{32}}{E_2E_3c} & \frac{\nu_{21}+\nu_{31}\nu_{23}}{E_2E_3c} & \frac{\nu_{31}+\nu_{21}\nu_{32}}{E_2E_3c} & 0 & 0 & 0 \\ \frac{\nu_{12}+\nu_{13}\nu_{32}}{E_3E_1c} & \frac{1-\nu_{13}\nu_{31}}{E_1E_3c} & \frac{\nu_{32}+\nu_{31}\nu_{12}}{E_3E_1c} & 0 & 0 & 0 \\ \frac{\nu_{13}+\nu_{12}\nu_{23}}{E_1E_2c} & \frac{\nu_{23}+\nu_{13}\nu_{21}}{E_1E_2c} & \frac{1-\nu_{12}\nu_{21}}{E_1E_2c} & 0 & 0 & 0 \\ 0 & 0 & 0 & 2G_{23} & 0 & 0 \\ 0 & 0 & 0 & 0 & 2G_{31} & 0 \\ 0 & 0 & 0 & 0 & 0 & 2G_{12} \end{bmatrix} \begin{bmatrix} \Delta \varepsilon_{11} \\ \Delta \varepsilon_{22} \\ \Delta \varepsilon_{33} \\ \Delta \varepsilon_{23} \\ \Delta \varepsilon_{31} \\ \Delta \varepsilon_{12} \end{bmatrix} \quad (4.2)$$

$$\text{Where, } c = \frac{1-\nu_{12}\nu_{21}-\nu_{23}\nu_{32}-\nu_{31}\nu_{13}-2\nu_{12}\nu_{23}\nu_{31}}{E_1E_2E_3} \quad (4.3)$$

In this research yarn properties in the plane perpendicular to the main longitudinal direction is assumed to isotropic. Material direction 11 refers to the main longitudinal direction of the yarn or direction perpendicular to material isotropy, direction 22 and 33 refers to the direction perpendicular longitudinal direction i.e. these directions represents material isotropy. The values for  $E_{11}$  was computed using single yarn tensile tests while

other material constants are based on literature values or assumptions. The determination of these material properties will be discussed in the following sections.

#### 4.2.2. Determination of $E_{11}$

To determine yarn's stress-strain behavior in the principal material direction, experimental tests were conducted at Arizona State University (ASU). These tests were discussed in details in chapter 3. Additionally, strain rate effects on this behavior were based on published experimental results. From the single yarn quasi-static tension tests conducted at ASU it was determined that the yarn had three distinct regions during loading; an initial region of low stiffness resulting from the low stress required to straighten the yarns, a region of high stiffness where low strain increases results in large stress increases (or elastic region), and a region of negative stiffness where the stress decreases rapidly with an increase in strain (or post-peak or softening region). Stress strain curves for single yarn tests (warp yarns) are shown in Figure 4.1. The stiffness, peak stress and strain at peak stress are gage length dependent. The yarn test results corresponding to gage length 17 in were used in determination of the material properties as longer length has lesser fixture effect.

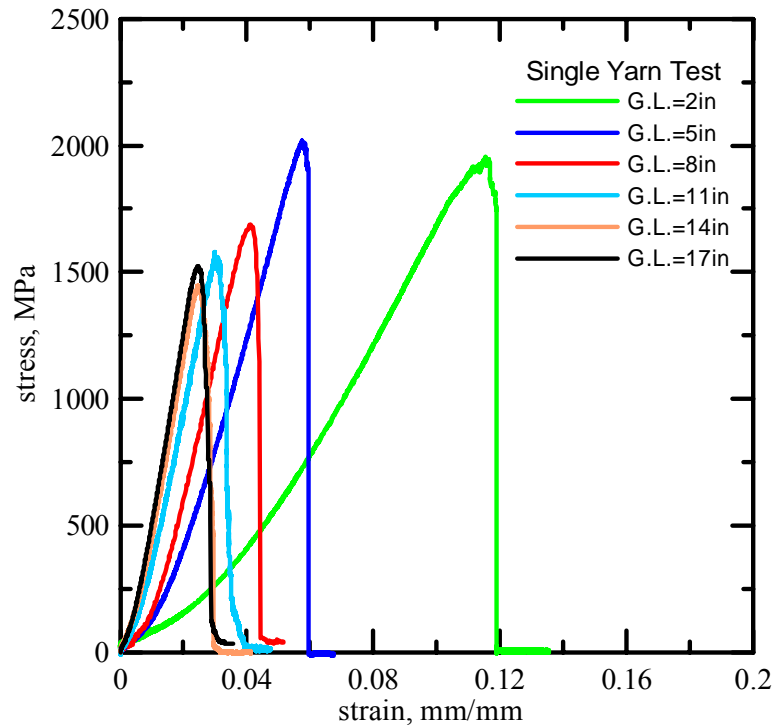


Figure 4.3. Stress vs strain curves of single yarn tensile tests for different gage lengths

#### Pre-peak Behavior in Material Model

Experimental test results showed the behavior of the fabric to be nonlinear. It is observed that the initial non-linear region is very small for 17 in model which is caused by the initial straightening of the test fixture and some undulations present in the yarn sample. Since, initial stiffness is geometric behavior instead of material behavior; this initial crimp is ignored when computing the stiffness for solid element representing yarn. The modified stress-strain curves (after removing crimp) are shown in Figure 4.4. As shown the prepeak response can be reasonably approximated by a linear function. A linear fitted curve used to represent material model is also shown along with the tension test results.

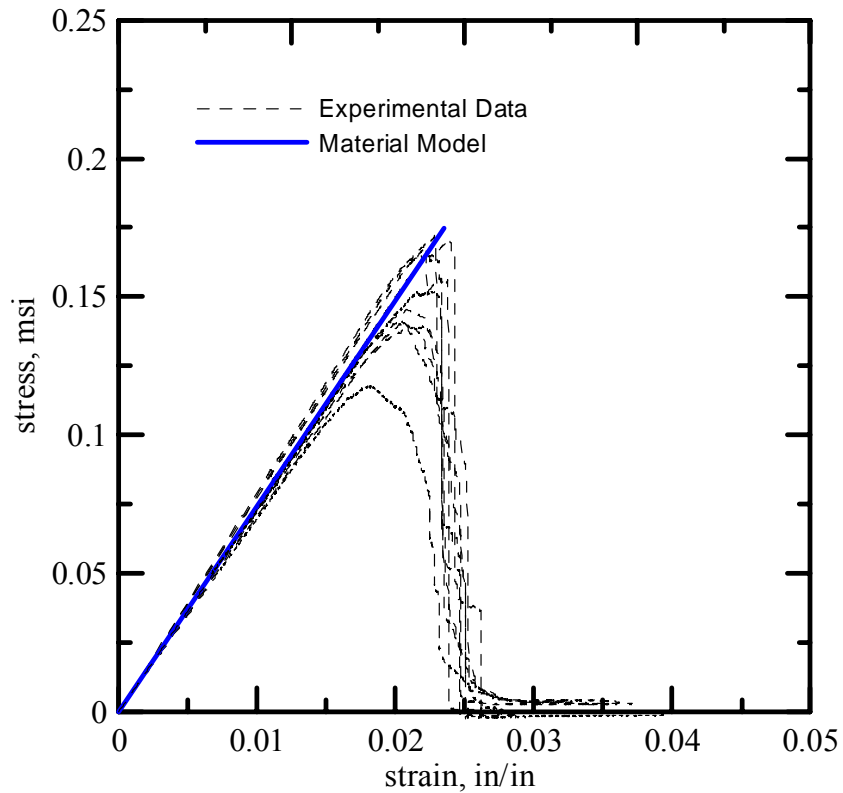


Figure 4.4. Kevlar warp yarn experimental stress-strain curves with linear approximation.

The linear approximation was constructed as follows. First the crimp region from the experimental curves was removed by extending the elastic region backward until it intersect x-axis and then shift the end to the origin. The strain at peak stress and peak stress were then chosen such that it represents tests with maximum stress values. The final values used in the material model to describe the warp direction pre-peak behavior were strain to peak stress ( $\varepsilon_{11}^{\max}$ ) of 0.024 and an elastic stiffness ( $E_{11}$ ) of  $7.43(10^6)$  psi. Due to unavailability of long fill yarns, testing was not performed for fill yarns. Fill yarn material properties were assumed to be same as warp yarns.

### Post-peak and failure behavior in Material Model

Kevlar®49 yarn consists of hundreds of filaments. The failure of yarn is primarily governed by the failure of filaments. One could imagine failure of yarn as a function of filament failure over a range of strain values. For the experimental purposes the strain level at which the load carrying capacity becomes very low is taken as failure strain but the physical failure occur at very large strain values. Therefore a simple approach was used to model yarn failure in a finite element simulation – once the element representing the yarn experienced a critical level of strain it was considered to have failed. There were several options for the failure strain value. One was to assume the failure strain was simply the strain reported at the end of the tension tests. However, after analyzing the deformed samples it was determined that much larger strains are required to fully fail the Kevlar yarns. It was observed that the yarn can experience strains larger than the last reported strain value from the test results. Testing was terminated when the load carrying capacity of the yarn reached very small. To simplify and simulate this in the material model, the post-peak region was approximated with a linear region followed by a non-linear region up until fabric failure. The linear post-peak region stiffness was determined by fitting a linear curve to the experimental results. It was found that the linear region post-peak stiffness was approximately -3.5 times the elastic stiffness. Thus the linear region stiffness ( $E_{11}^{soft}$ ) was  $-26.00(10^6)$  psi. A level of strain or stress had to be assumed for where the non-linear post-peak region began. In the material model it was assumed that if the stress was less than 2,000 psi then the stress-strain response was in the post-

peak non-linear region in that respective direction. The stress in the non-linear region was assumed as follows.

$$\sigma_{11} = \sigma^* \left( 1 - \left( \frac{\varepsilon_{11} - \varepsilon_{11}^*}{\varepsilon_{fail} - \varepsilon_{11}^*} \right)^{dfac} \right) \quad (4.4)$$

In the above equations  $\sigma^*$  and  $\varepsilon^*$  are the stress and strain values at which the non-linear region begins in each respective direction,  $\varepsilon_{fail}$  is the failure strain in each respective direction, and  $dfac$  is a factor which specifies the rate of decrease in stress. The values for  $\varepsilon^*$  were computed in the subroutine. The values for failure strain and the factor  $dfac$  was considered to be 0.2. Figure 4.5 shows the stress-strain response (used in the finite element simulations) for the pre-peak and post-peak behavior.

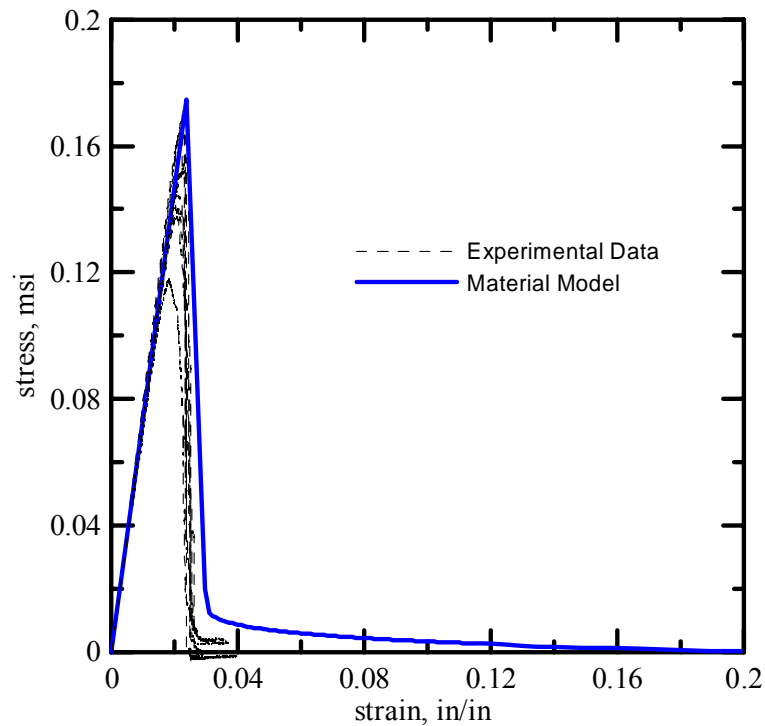


Figure 4.5. Kevlar® 49 yarn uniaxial stress-strain results with approximation for pre-peak and post-peak behavior

### Unloading/reloading and compression behavior

When the fabric is subjected to impact loads it can load and unload many times throughout the event. So, it is important to model cyclic behavior correctly. Cyclic testing was not performed at yarn level, so, it was assumed that the yarn unload and reload along the same path which is same as initial loading. So, in the material model the unloading and reloading stiffness were expressed as a factor of 1.0 times the elastic stiffness. Thus the unloading and reloading stiffness for the yarn ( $E_{11}^{unl}$ ) was  $7.43(10^6)$  psi. Kevlar<sup>®</sup>49 yarn has negligible compressive stiffness. However to avoid numerical instabilities, a very small stiffness was assumed when the finite element experiences compression. The compressive stiffness was taken as 0.5% of the elastic stiffness. Thus the compressive stiffness of the yarn ( $E_{11}^{comp}$ ) direction was assumed to be  $3.7(10^4)$  psi.

### Strain rate effect

The most successful published results on single yarn tensile tests were reported by Wang and Xia who achieved strain rate testing of Kevlar<sup>®</sup> 49 yarns up to a rate of  $1350 \text{ s}^{-1}$  [Wang and Xia, 1999]. The results from their research that show the strain rate effect on the stress-strain response of the yarns is shown in Figure 4.6.

The results show that there is an increase in the yarn peak stress and failure strain with an increase in strain rate. The increase in peak stress is caused by an increase in stiffness and an increase in the strain to peak stress. It was desired to develop a strain rate model that captured this increase in stiffness and increase in strain to peak stress while maintaining approximately the same relative increase in the peak stress found in the

experimental results. The Cowper-Symonds model was chosen to simulate the strain rate effects [Cowper and Symonds, 1957].

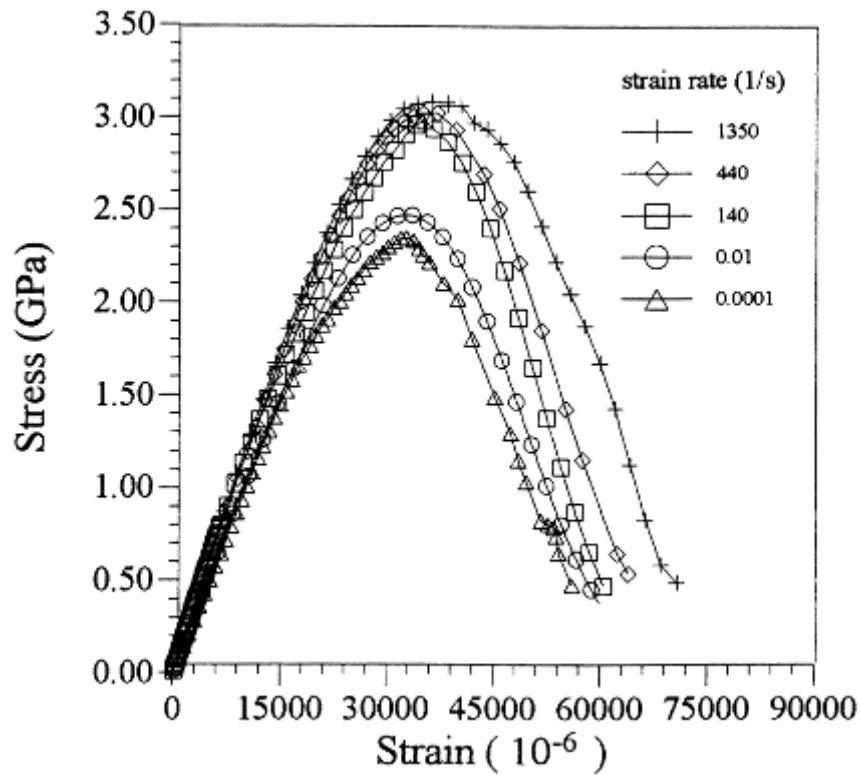


Figure 4.6. Strain rate effect on the stress-strain behavior of Kevlar® 49 yarns from Wang and Xia

The general Cowper-Symonds model accounts for increases in the peak stress of a material with an increase in strain rate is shown below.

$$\sigma^{\max(adj)} = \sigma^{\max} \left( 1 + \frac{\dot{\epsilon}}{C} \right)^{\frac{1}{P}} \quad (4.5)$$

In the above equation  $\sigma^{\max}$  is the static peak stress,  $\sigma^{\max(adj)}$  is the adjusted peak stress due to some level of strain rate,  $\dot{\epsilon}$  is the strain rate, and the  $C$  and  $P$  factors are unique to each material and need to be determined experimentally. The model captures



the non-linear strain rate effects that many materials experience by simulating the rapid increase in material properties at a lower range of strain rates and a less rapid increase in material properties at very high strain rates.

In the material model the elastic stiffness and strain to peak stress were assumed to be a function of the strain rate using the Cowper-Symonds model. The peak stress was indirectly assumed to be a function of the strain rate as the elastic stiffness and the strain to peak stress was increased. The elastic stiffness for the yarn was adjusted based on the strain rate as shown below.

$$E_{11}^{adj} = E_{11} \left( 1 + \frac{\dot{\epsilon}_{11}}{C_E} \right)^{\frac{1}{P_E}} \quad (4.6)$$

In the above equations  $E$  is the static elastic stiffness,  $E^{adj}$  is the adjusted elastic stiffness in each respective direction,  $\dot{\epsilon}$  is the strain rate in each respective direction, and  $C_E$  and  $P_E$  are Cowper-Symonds  $C$  and  $P$  factors describing the strain rate effects on the elastic stiffness. The crimp stiffness, unloading and reloading stiffness, and the post-peak stiffness were assumed to be unaffected by the strain rate. The crimp strain was also assumed to be unaffected by the strain rate.

The effective strain to peak stress was adjusted based on the strain rate. The effective strain to peak stress in this case is defined as the strain to peak stress minus the crimp strain.

$$\epsilon_{11}^{\max(adj)} = \epsilon_{11}^{\max} \left( 1 + \frac{\dot{\epsilon}_{11}}{C_\epsilon} \right)^{\frac{1}{P_\epsilon}} \quad (4.7)$$

In the above equations  $\epsilon^{\max}$  is the effective strain to peak stress,  $\epsilon^{\max(adj)}$  is the adjusted effective strain to peak stress,  $\dot{\epsilon}$  is the strain rate, and  $C_\epsilon$  and  $P_\epsilon$  are Cowper-

Symonds  $C$  and  $P$  factors describing the strain rate effects on the effective strain to peak stress. The failure strain was not assumed to be a function of the strain rate as much larger strains than are reported experimentally are already assumed as the failure strain in the material model

The factors  $C_E$ ,  $P_E$ ,  $C_\varepsilon$  and  $P_\varepsilon$  were determined by fitting the normalized effect on the peak stress on the material model using those factors with the normalized effect on the peak stress from the experimental results. The normalized peak stress is defined as the adjusted peak stress divided by the static peak stress. Thus in the material model the normalized peak stress in the warp direction can be represented as shown below.

$$\frac{\sigma_{11}^{\max(adj)}}{\sigma_{11}^{\max}} = \frac{1}{\sigma_{11}^{\max}} \left( \varepsilon_{11}^{crp} E_{11}^{crp} + \varepsilon_{11}^{\max(adj)} E_{11}^{adj} \right) \quad (4.8)$$

In the above equation  $\varepsilon^{crp}$  is the crimp strain and  $E^{crp}$  is the crimp stiffness. From ballistic test simulation it was found that the element strain rate exceeded the maximum level found in the experimental tests, oftentimes reaching 10,000 or even 15,000  $s^{-1}$ . Therefore the fitting was based on an estimated extrapolation of the experimental results. The values for  $C_E$ ,  $P_E$  which best correlated with the experimental results were 5  $s^{-1}$ , and 40.0, respectively. The values for  $C_\varepsilon$  and  $P_\varepsilon$  which best correlated with the experimental results were 5  $s^{-1}$ , and 40.0, respectively. Figure 4.7 shows the normalized peak stress as a function of strain rate using these factors with the Cowper-Symonds model along with the experimental yarn results. The results are shown up to a strain rate of 10,000  $s^{-1}$ .

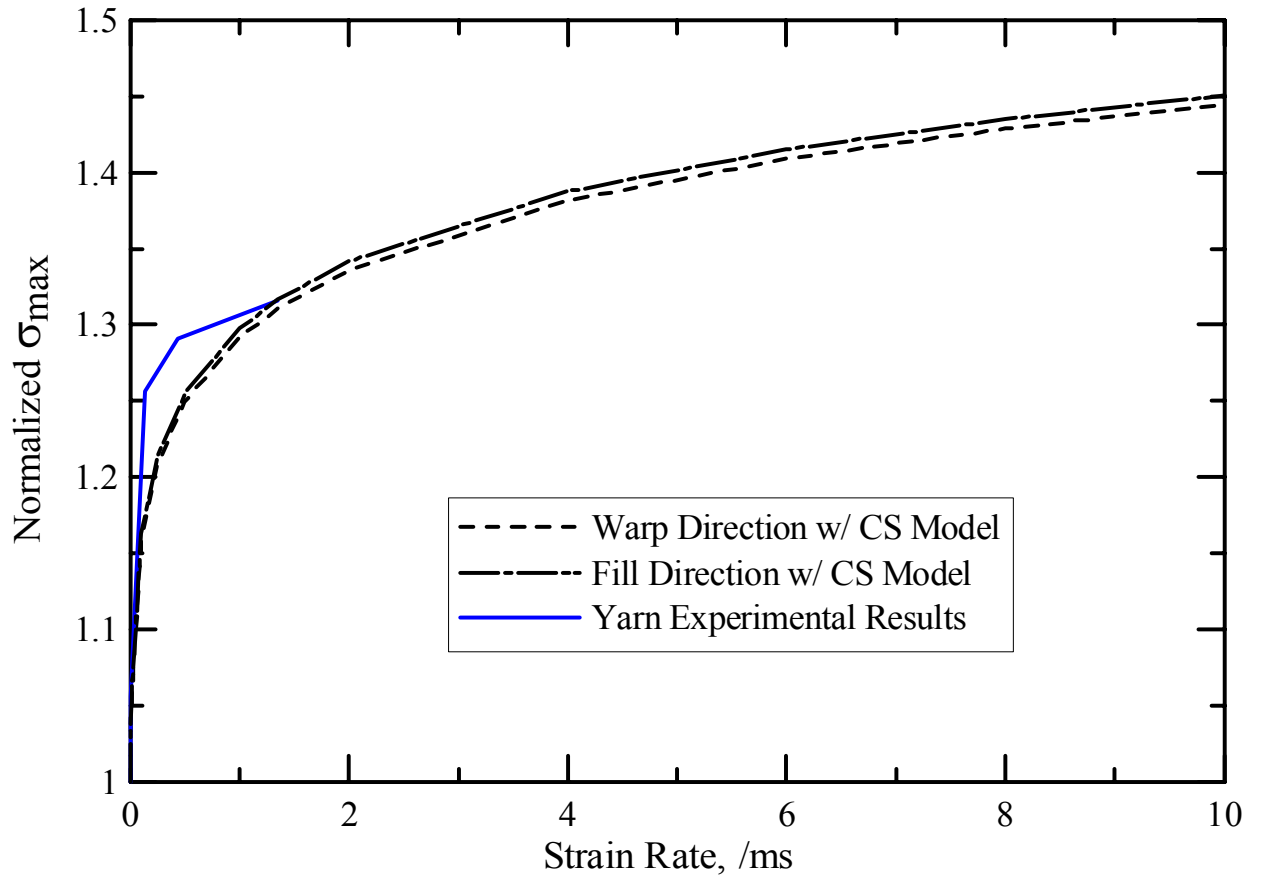


Figure 4.7. Normalized peak stress as a function of strain rate for material strain rate model and experimental results

During a simulation an element's strain rate can vary. This does not pose a problem for the elastic stiffness strain rate model as the stiffness is simply allowed to change at each step depending on the current strain rate however, in the effective strain to peak stress model the strain to peak stress cannot be allowed to constantly change throughout the analysis. This would cause complications in the stress-strain path of the element. For this reason an assumption was made that the effective strain to peak stress would be a function of the maximum strain rate that the element experiences during the analysis. So, the equation for adjusted strain becomes:-

$$\varepsilon_{11}^{\max(adj)} = \varepsilon_{11}^{\max} \left( 1 + \frac{\dot{\varepsilon}_{11}^{\max}}{C_{\varepsilon}} \right)^{\frac{1}{P_{\varepsilon}}} \quad (4.9)$$

where  $\dot{\varepsilon}^{\max}$  is the maximum strain rate experienced by the element in each respective direction.

Figure 4.8 shows the effect of the strain rate model on the stress-strain response on the yarn model.

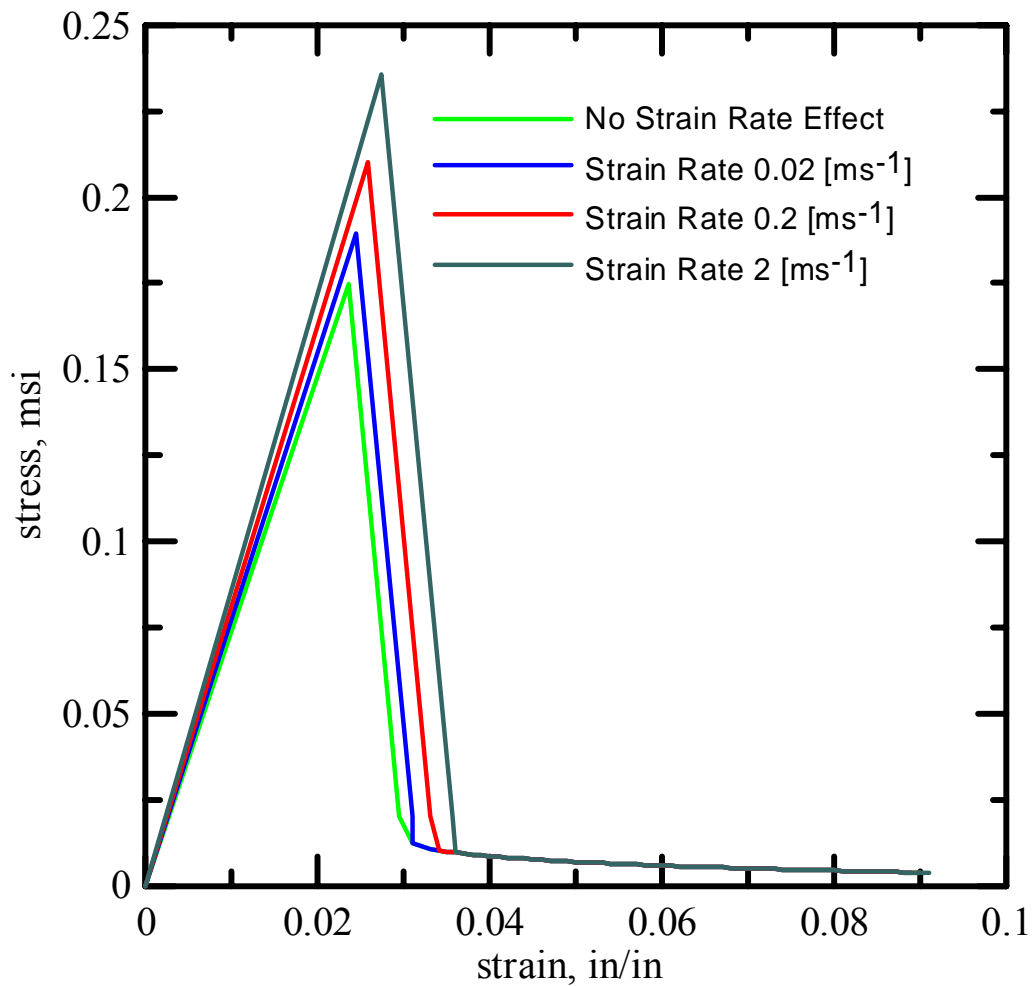


Figure 4.8. Strain rate effects on the yarn model

#### 4.2.3. Determination of $E_{22}$ , $E_{33}$ , $G_{13}$ , $G_{12}$ and poisson's ratio

Material properties other than  $E_{11}$  were approximated based on the Kevlar yarn behavior and data available in literature. Young's modulus other than  $E_{11}$  i.e.  $E_{22}$  and  $E_{33}$  were assumed to be 0.5% of  $E_{11}$  as yarn has very low load carrying capacity in direction perpendicular to main longitudinal direction. This is due to presence of hundreds of filaments which are free to move relative to each other. The shear modulus of the yarn is expected to be low. Cheng and co-worker [Cheng, 2005] conducted torsional experiments to compute shear modulus of single filament. They found that  $G_{13}$  is around 24.4 GPa and  $G_{12}$  is very small. In this research the yarn level shear modulus  $G_{13}$  &  $G_{12}$  is assumed to be 3.48 msi and  $G_{23}$  is assumed to be 0.5% of  $E_{11}$ . There is no available literature for the poisson's ratio of Kevlar yarn. In this research poisson's ratio is assumed to be zero. Values of all the material parameters are listed in APPENDIX-A.

### 4.3. Verification of Micro-mechanical model

#### 4.3.1. Single Yarn Simulations

The material model developed for Kevlar Yarn solid elements was validated by single yarn tensile test simulation of warp yarn using explicit finite element code, LS-DYNA. The length of the yarn used in the simulation was 2 in. The geometric model was based on the parameters computed during experimental phase of this research. Figure 4.9 shows top view and side of a Kevlar yarn finite element model.

One end of the model was kept fixed and other end was given a velocity to simulate stroke controlled test. The stroke rate used in the actual test was 0.2 [in/min], however if this small rate is used the simulation will take very large simulation time even

for small models. To reduce the clock time for the simulation, these simulations were run using multi-processor cluster. Typically 16 nodes or processor were used to run the simulations. Mass scaling was used to increase the time step of the simulation and displacement rate was increased artificially (time scaling) to reduce to overall simulation time. To reduce the inertial effect on the model ramp function was used to apply velocity. A typical ramp function is shown in the Figure 4.10. Although in actual test the strain rate was very low (quasi-static test), the strain rate in simulation is expected to be high due to velocity scaling. So, in order to diminish these undesirable strain rate effects, the material model was made insensitive to the strain rate by modifying the values of Cowper-Symonds factors (C and P).

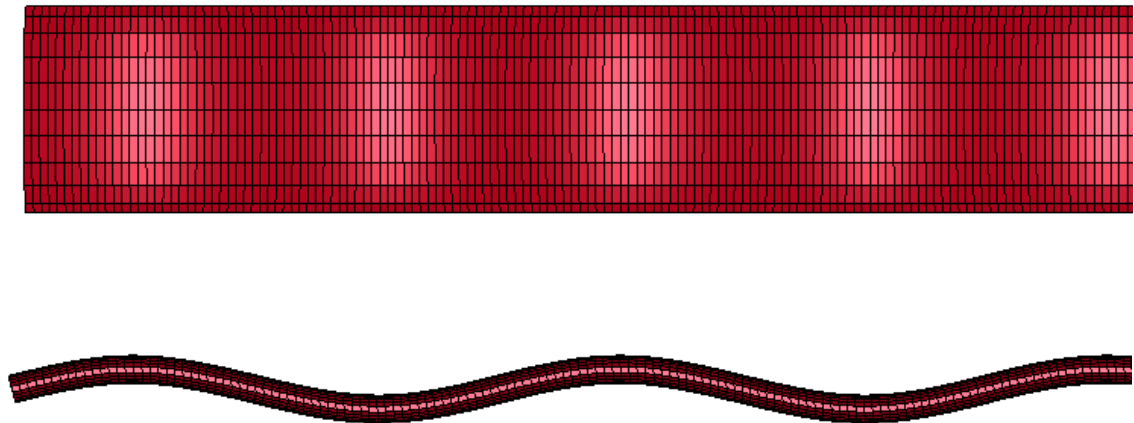


Figure 4.9. Single Yarn model

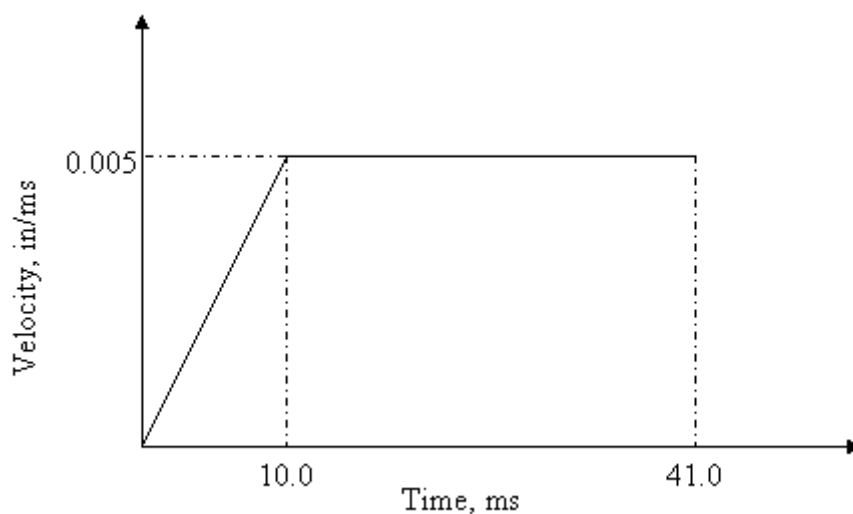


Figure 4.10. Ramp function used to apply velocity

The effect of mesh density on the response of single yarn tensile test was studied. Coarse mesh is modeled with 100 elements per sine wave and fine mesh was modeled with 1800 elements per sine wave. All other meshes lie in between these two extremes. Table 4.3 shows different meshes used for single yarn simulation.

Table 4.3: Mesh Study – Single Yarn Simulations

	Number of elements		
	Along length per sine curve	Along Width	Along Thickness
Mesh 1	10	10	1
Mesh 2	20	10	1
Mesh 3	20	20	2
Mesh 4	20	10	3
Mesh 5	40	20	3
Mesh 6	40	20	1
Mesh 7	60	30	1
Mesh 8	60	10	1

Figure 4.11 shows yarn cross-section at different time interval during simulation. It is observed that the yarn was crimped before the simulation starts. During the

simulation undulations in the yarn or amplitude of the sinusoidal curve reduces and eventually the amplitude of the sine curves becomes zero and the yarn represents the straight yarn without any undulations. The failure of in the yarn is observed when the element in the yarn reaches fail strain.



Figure 4.11. (a) Cross-section of Kevlar Yarn at the start of simulation



Figure 4.11. (b) Cross-section of Kevlar Yarn during simulation



Figure 4.11. (c) Cross-section of Kevlar Yarn during simulation



Figure 4.11. (d) Cross-section of Kevlar Yarn just before breakage



Figure 4.11. (e) Cross-section of Kevlar Yarn after failure



Figure 4.12 shows the effect of mesh density on the stress strain response of the Kevlar single yarn simulations. In the figure mesh 1 indicates coarse mesh and mesh 8 indicates fine mesh. It is observed that as the number of elements along the length is increased the yarn tries to straighten out with ease than using coarse mesh or in other terms the coarse mesh is stiffer than fine mesh. The initial low stiffness region visible in mesh 8 is due to the crimp in yarn. So, the undulations in the model compensates for the crimp. The maximum stress seems to be lower than the experimental test.

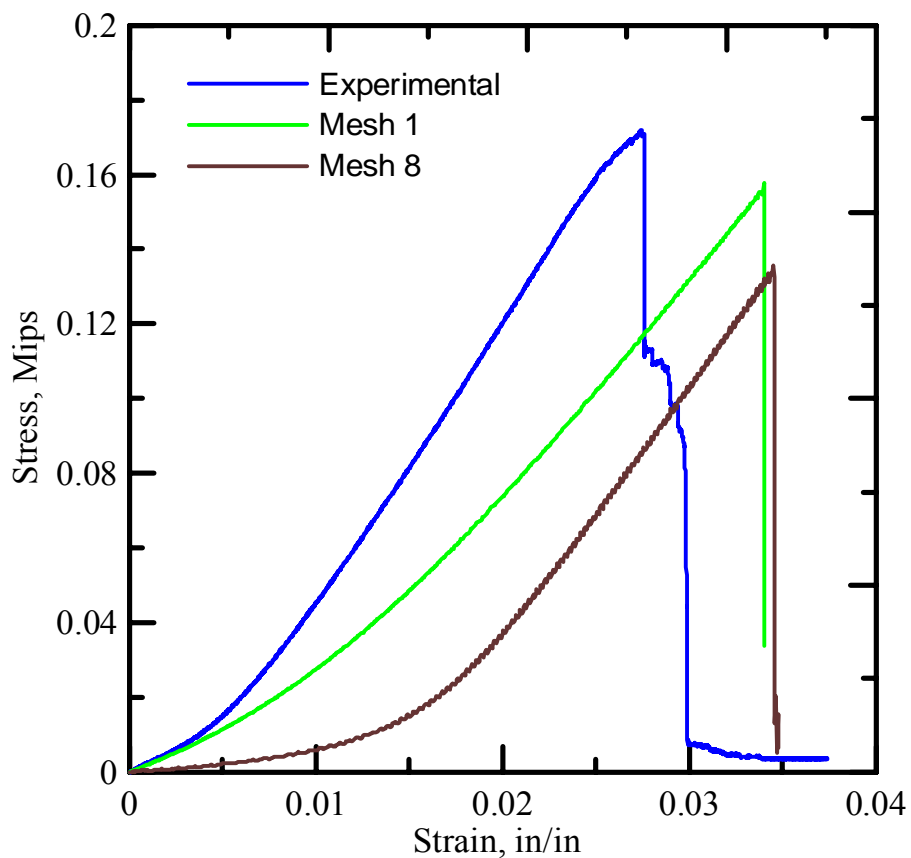


Figure 4.12. Mesh density effect on single yarn simulation

Figure 4.13 shows the stress strain response of single Kevlar yarn using fine mesh. A good co-relation between the simulation and experimental response can be observed when curve is shifted by 0.012 in/in. The initial low stiffness zone is the region when yarn becomes straight and requires lesser load than the elastic region. This region is not seen in the experimental test as crimp was removed due to handling and initial tighten of the yarn in grips. The peak stress can be matched using this argument and increasing the strain at the peak stress in the input files.

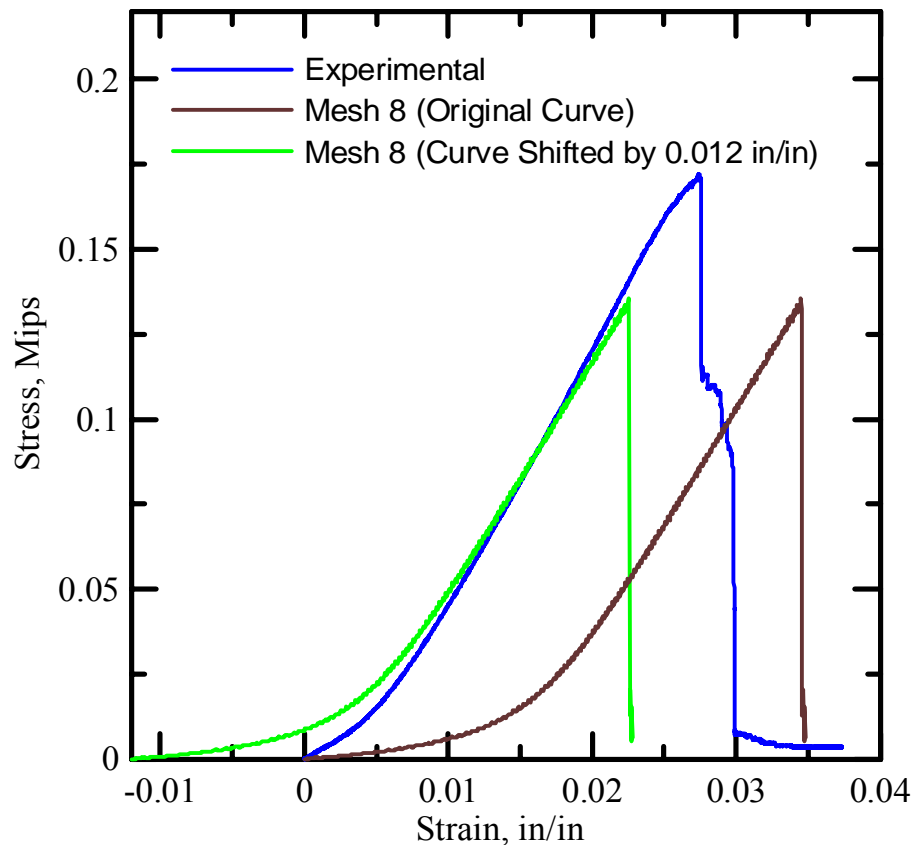


Figure 4.13. Simulation curve shifted by 0.012 in/in

### 4.3.2. Swath Tensile Test Simulations

The Kevlar fabric can be generated by using unit cell model developed based on the Kevlar geometry parameters computed in this research. Figure 4.14 shows the model of unit cell. Warp direction is represented along x-axis and fill direction is represented along y-axis.

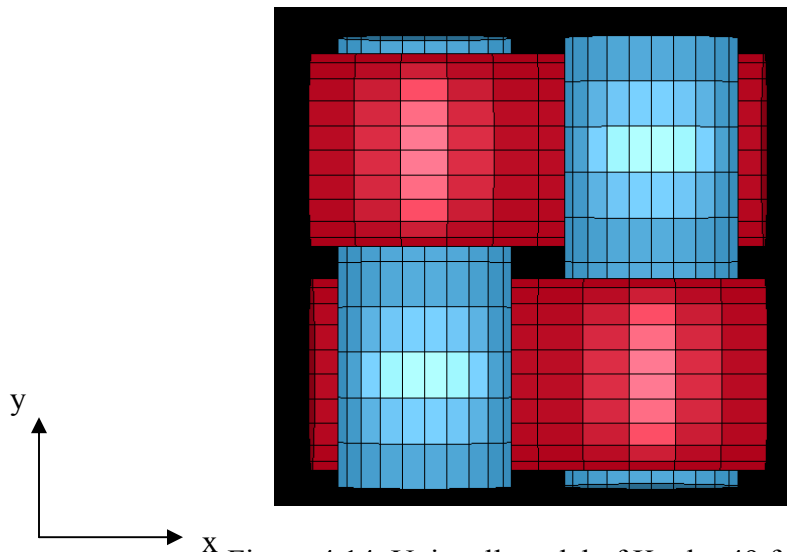


Figure 4.14. Unit cell model of Kevlar 49 fabric

The swath model was built by replicating unit cell in fill and warp directions. Figure 4.15 shows the swath model (5 in x 1 in) of Kevlar created by replicating the unit cells in fill and warp directions.

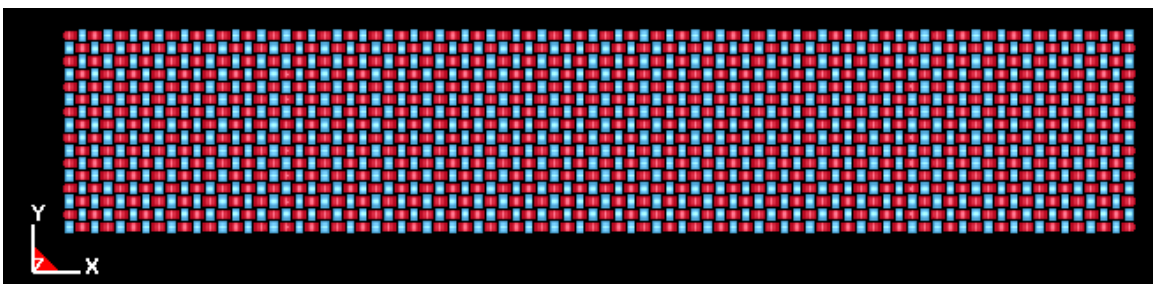


Figure 4.15. Swath Model

One end of the model was kept fixed and other end was given a velocity to simulate stroke controlled test. The stroke rate used in the actual test was 0.2 [in/min], however if this small rate is used the simulation will take very large simulation time due to large number of cycles required to complete the simulation. To reduce the clock time for the simulation, these simulations were run using multi-processor cluster. Typically 32 nodes or processor were used to run the simulations. Mass scaling was used to increase the time step of the simulation and displacement rate was increased artificially (time scaling) to reduce to overall simulation time. To reduce the inertial effect on the model ramp function was used to apply velocity. A typical ramp function is shown in the Figure 4.16. Although in actual test the strain rate was very low (quasi-static test), the strain rate in simulation is expected to be high due to velocity scaling. So, in order to diminish these undesirable strain rate effects, the material model was made insensitive to the strain rate by modifying the values of Cowper-Symonds factors (C and P).

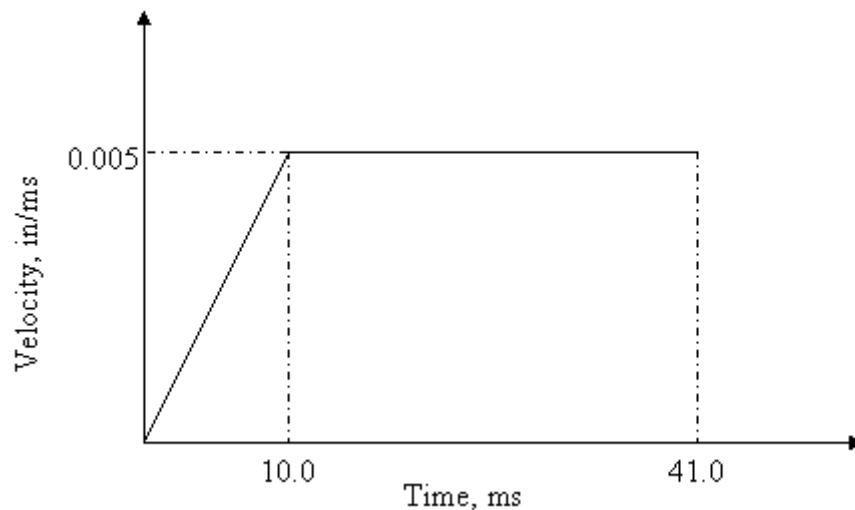


Figure 4.16. Ramp function used to apply velocity

Fine mesh is used for swatch simulations as contact surfaces between fill and warp yarns plays very important role in these simulations. Figure 4.17 shows the cross-section along longitudinal warp yarns during the simulation and Figure 4.18 shows the longitudinal cross-section during experiments. It is observed that model is capable of capturing warp yarn behavior which is strengthening of these yarns under the application of the loading. The transverse cross-section of fill yarns as it can be seen is not changed much during simulation this is due to inbuilt drawback of representing hundreds of filaments using solid elements.

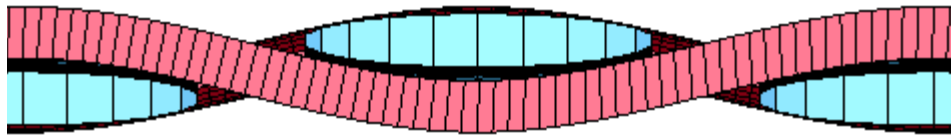


Figure 4.17. (a) Warp yarn longitudinal cross-section at the start of simulation

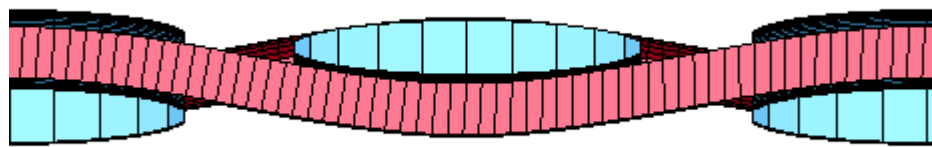


Figure 4.17. (b) Warp yarn longitudinal cross-section during simulation

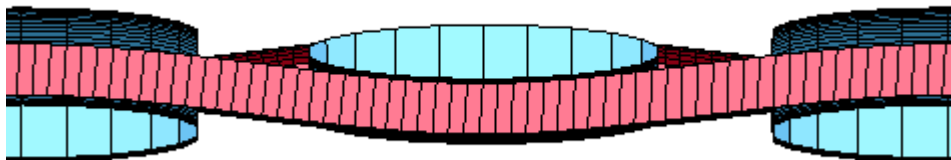


Figure 4.17. (c) Warp yarn longitudinal cross-section during simulation



Figure 4.18 (a). Warp yarn longitudinal cross-section – undeformed geometry



Figure 4.18 (b). Warp yarn longitudinal cross-section under 1.0% Strain level



Figure 4.18 (c). Warp yarn longitudinal cross-section under 1.5% Strain level



Figure 4.18 (d). Warp yarn longitudinal cross-section under 2.0% Strain level

Figure 4.19 shows the longitudinal cross-section of fill yarns during the simulation and Figure 4.20 shows the longitudinal cross-section during experiments. It is observed that fill yarns become wavier as warp yarns are loaded. This phenomenon is well captured by the model however, current model is unable to capture the change in transverse cross-section of warp yarns. This is due to an inbuilt drawback of the model in which hundreds of filaments are represented by solid elements of yarns which restricts the ability of filaments to move over each other.



Figure 4.19. (a) Fill yarn longitudinal; cross-section at the start of simulation

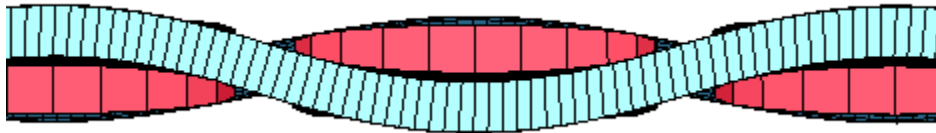


Figure 4.19. (b) Fill yarn longitudinal cross-section during simulation

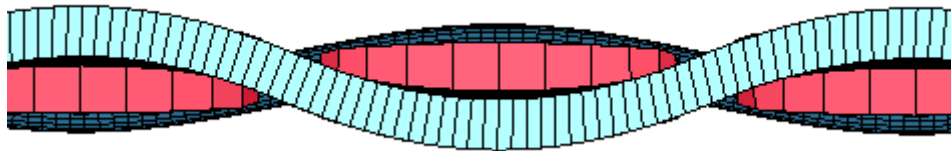


Figure 4.19. (c) Fill Yarn longitudinal cross-section during simulation



Figure 4.20. (a) Fill yarn longitudinal cross-section – undeformed geometry

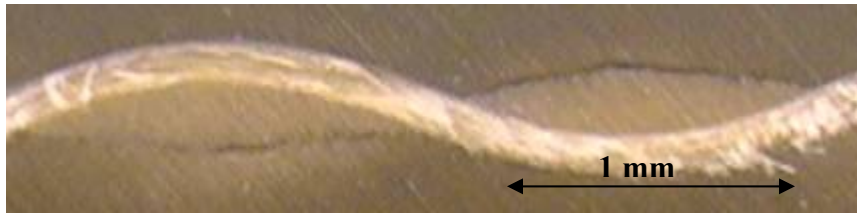


Figure 4.20. (b) Fill yarn longitudinal cross-section under 1.0% Strain level



Figure 4.20. (c) Fill yarn longitudinal cross-section under 1.5% Strain level



Figure 4.20. (d) Fill yarn longitudinal cross-section under 2.0% Strain level



Figure 4.21 shows the quantitative comparison of longitudinal cross-section of fill and warp yarns. It is observed that simulation is capable of predict overall response pattern for the longitudinal cross-section of both fill and warp yarns. The difference between the measure value of the parameters can be attributed to the solid element formulation of yarn which restricts the movement of filaments as it can be seen in the real yarn.

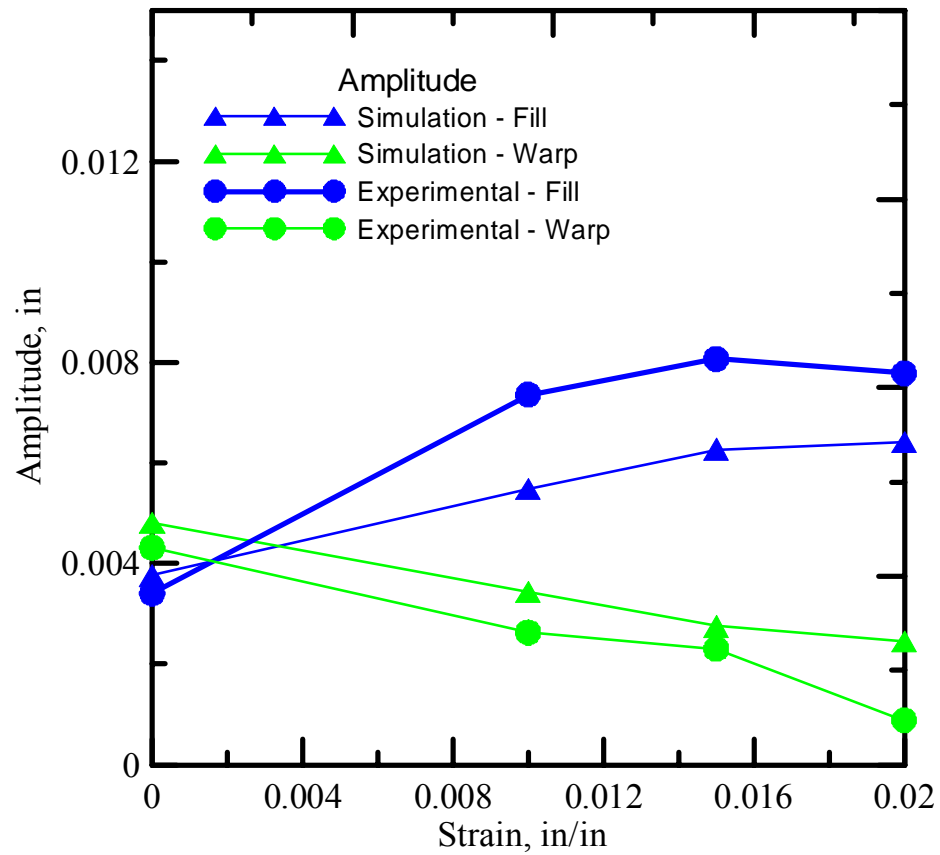


Figure 4.21. Amplitude comparison of longitudinal cross-section of fill and warp yarns

Figure 4.22 shows the stress-strain response of the swatch model. The simulation prediction of strength is lesser than the average strength reported by the swatch tests. The stiffness of the model is also lesser than the stiffness values reported by the experiments.

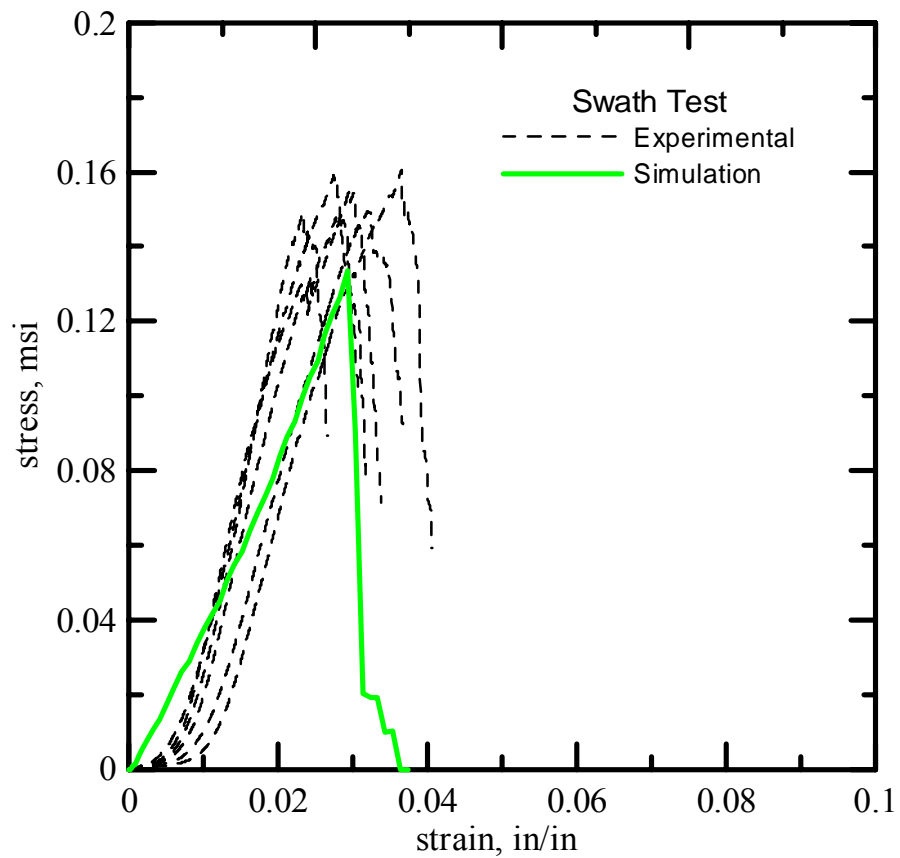


Figure 4.22. Preliminary single yarn simulation results

## **5. CONTINUUM MODEL**

### 5.1. Introduction

In the prior study at ASU, Kevlar<sup>®</sup>49 material model (ASUumatv1.0) was developed which was based on the results from static and dynamic experimental tests and included non-linearity in the stress-strain response, strain rate effects, and a failure criterion. The model was incorporated into the LS-DYNA finite element program through a user defined material definition (subroutine) and was validated by comparing the results against experimental ballistic tests conducted at NASA Glenn Research Center. Detailed description of this material model is explained in [Stahlecker, 2007]. In this model fabric layers were represented by single FE layer. The thickness of FE layer was assumed to be equal to the thickness of total number of layers in the model. Although, the simulation results were shown to match closely with the experimental tests for most of the test cases however, the results for the very low or very high projectile velocity test cases did not match closely with the experiments. Further, the friction between the fabric layers is considered to be an important factor in fabric behavior but this model failed to capture the effect of friction on the test results. This indicates that additional research is required to improve the material model and ballistic test modeling methodology. This chapter deals with the modification made in the failure criteria and modeling methodology.

### 5.2. ASU Continuum Model

#### 5.2.1. Improvements in Current Continuum Model

The primary mode of failure of Kevlar<sup>®</sup>49 is the breakage of the warp or fill direction yarns. There were several options to compute the failure strain value. One was

to assume the failure strain was simply the strain reported at the end of the tension tests. However, after analyzing the deformed fabric samples it was determined that much larger strains are required to fully fail the fabric yarns. One of the fabric samples at the end of the warp direction tension test is shown in Figure 5.1.

From the deformation shown in the Figure 5.1 it is clear that the fabric can experience strains larger than the last reported strain value from the test results. Testing was terminated when the load carrying capacity of the fabric reached almost zero. To simplify and simulate this in the material model, the post-peak region was approximated with a linear region followed by a non-linear region up until fabric failure.

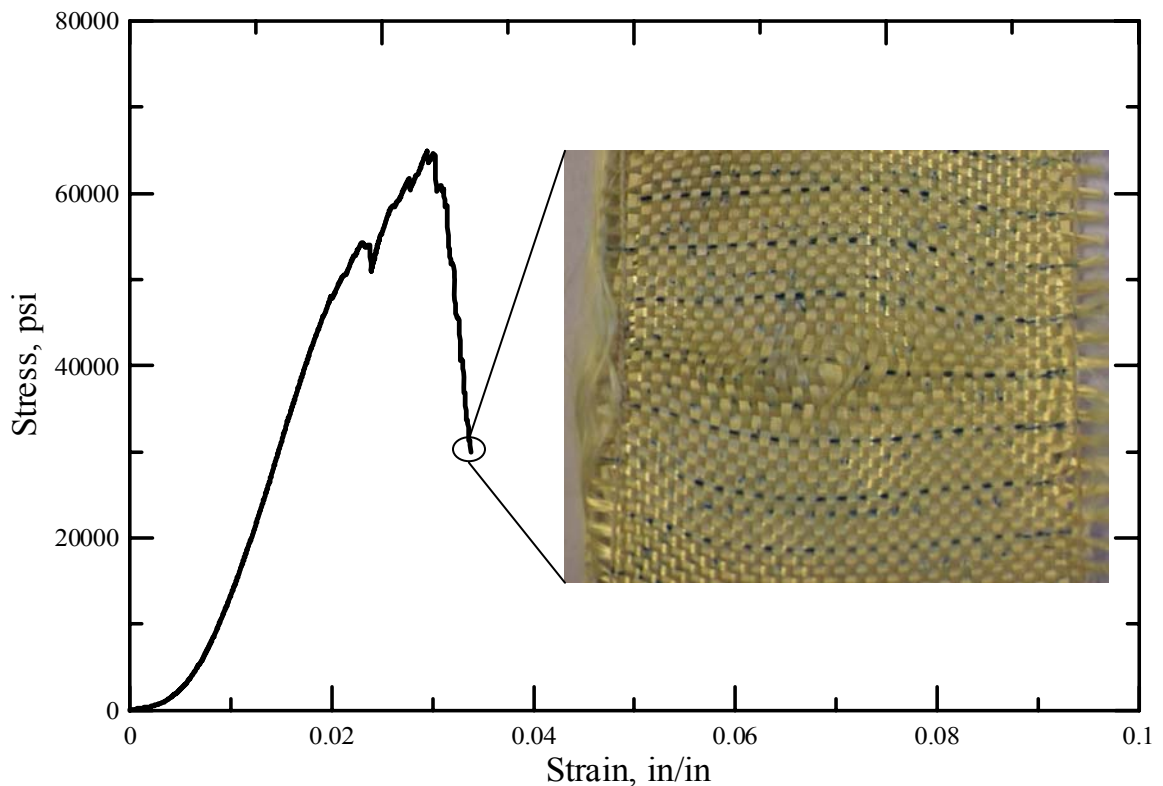


Figure 5.1. Fabric sample at end of warp direction tension test

Figure 5.2 and 5.3 shows the experimental swatch tensile test results and ASU material model (ASUumatv1.0) developed for Kevlar<sup>®</sup>49. In ASUumatv1.0 a simple approach was used to model fabric failure in a finite element simulation – once the element representing the fabric experienced a critical level of strain in either the warp or fill directions the element was considered to have failed. This critical value for both fill and warp direction was considered to be 0.2.

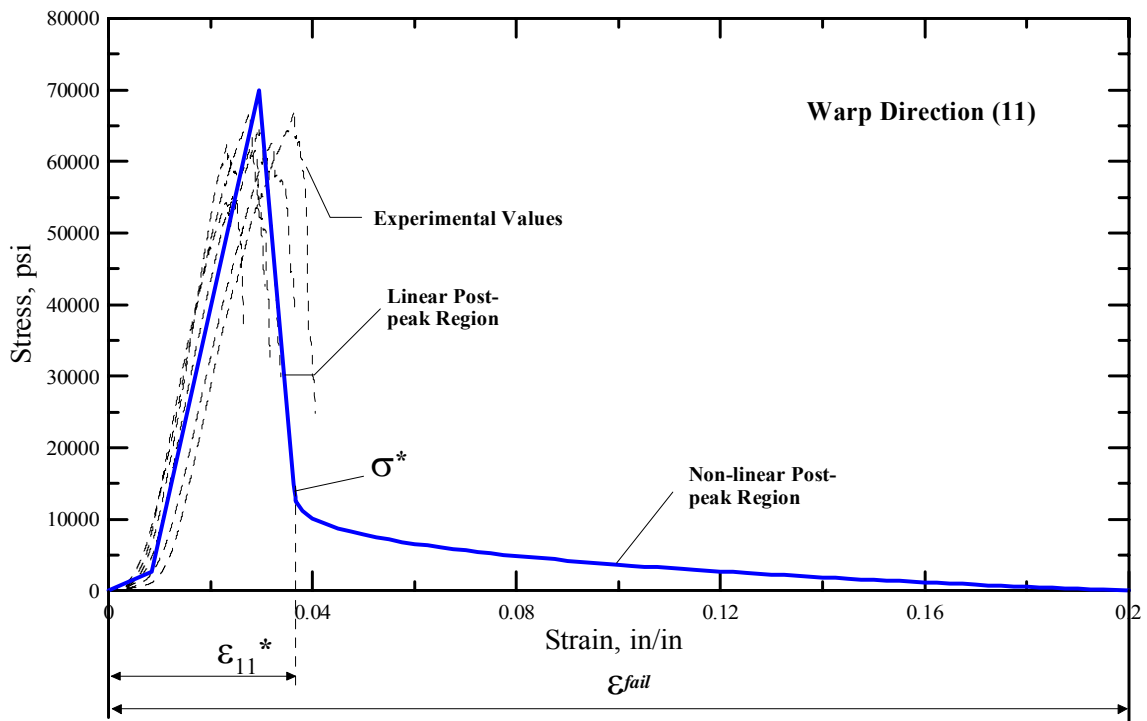


Figure 5.2. Kevlar<sup>®</sup> 49 warp (11) direction uniaxial stress-strain results with approximation for pre-peak and post-peak behavior

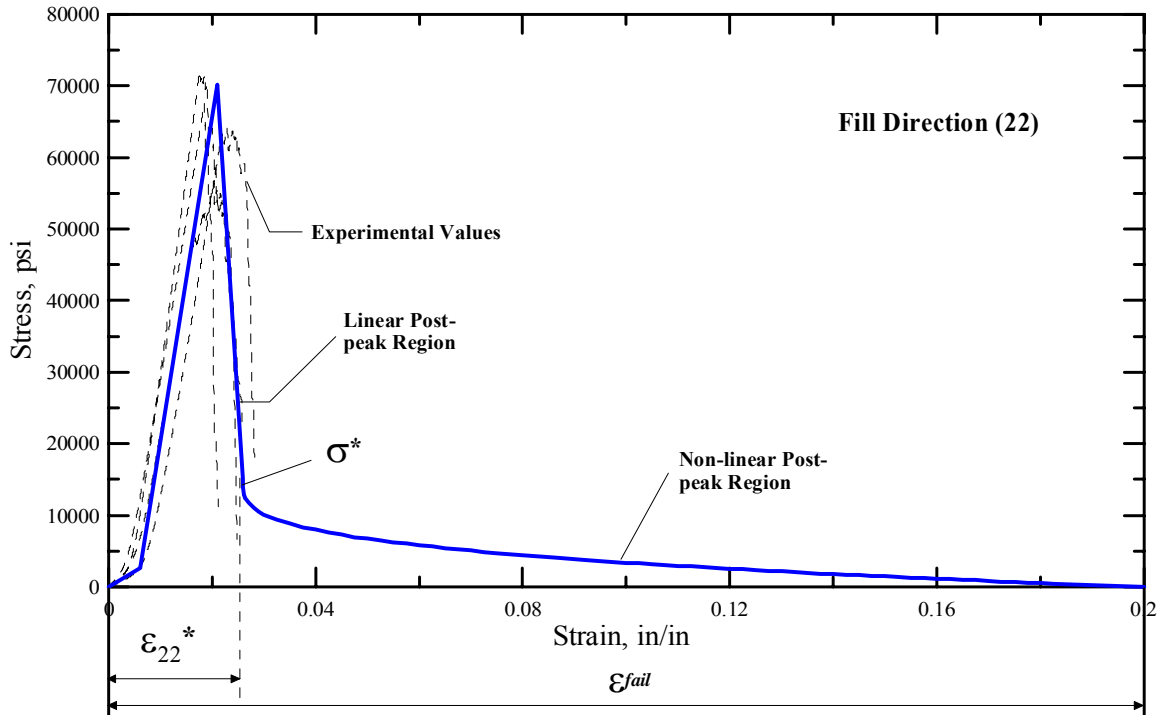


Figure 5.3. Kevlar® 49 fill (22) direction uniaxial stress-strain results with approximation for pre-peak and post-peak behavior

In the finite element model the fabric is represented by the shell elements and local coordinate system of shell element is used to define material directions. In ASUumatv1.0 when strain in any direction reached fail strain, the element is considered to be failed in both the directions. Further, as observed in Figure 5.2 & 5.3 although experimental tests shown that the material is unable to carry any load after certain strain level, ASUumatv1.0 have substantial load carrying capacity in the non-linear region of the post peak curve. In ASUumatv1.1 following two modifications were made to improve the material model.

- 1) The stress at which the non linear curve starts is reduced from 15000 psi to 5000 psi. This results in lesser load carrying capacity of the fabric under post peak region which is closer to actual experimental tests.
- 2) The failure in fill and warp directions was decoupled by providing separate fail strain in both the directions. If the strain level in one direction is reached at fail strain then the load carrying capacity of that direction was reduced to zero where as other direction can still carry the load up to fail strain. This fail strain in the ASUumatv1.1 is specified as 0.1. In order to limit total strain in any direction, the overall strain in the element in any direction is restricted to 0.35.

Figure 5.4 and Figure 5.5 shows the comparison of the ASUumatv1.0 and ASUumatv1.1 material model comparison for both fill and warp directions.

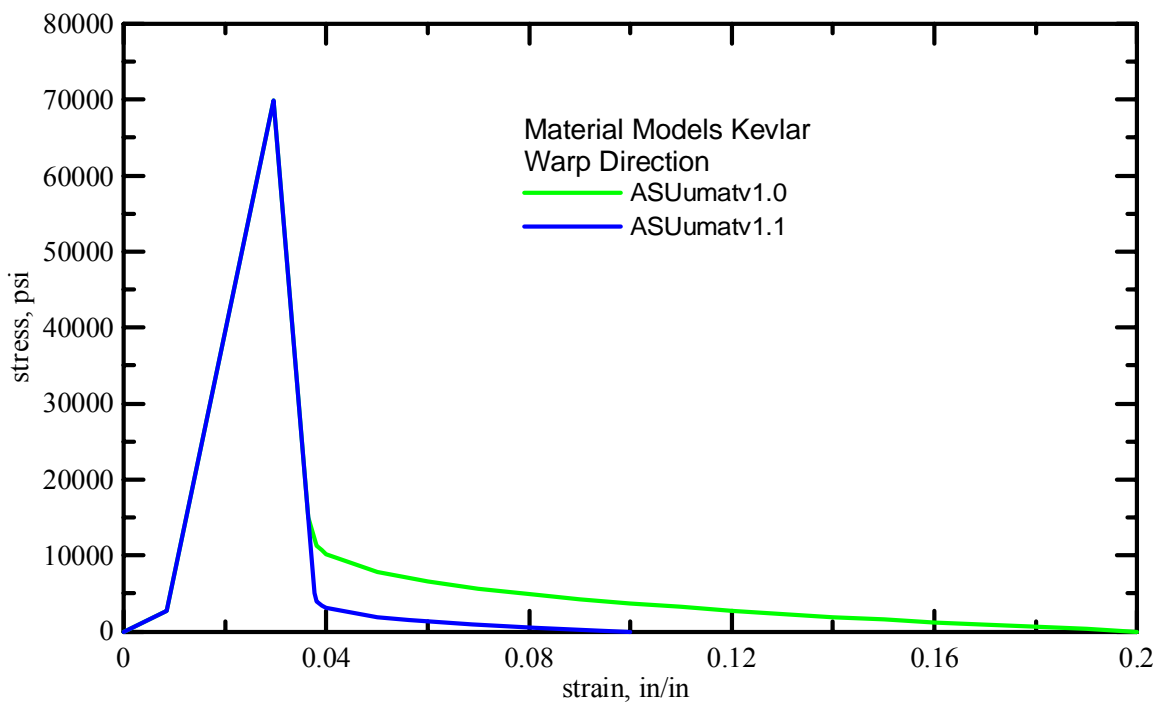


Figure 5.4. Kevlar® 49 warp (11) direction load curves used in ASU material model v1.0 and v1.1

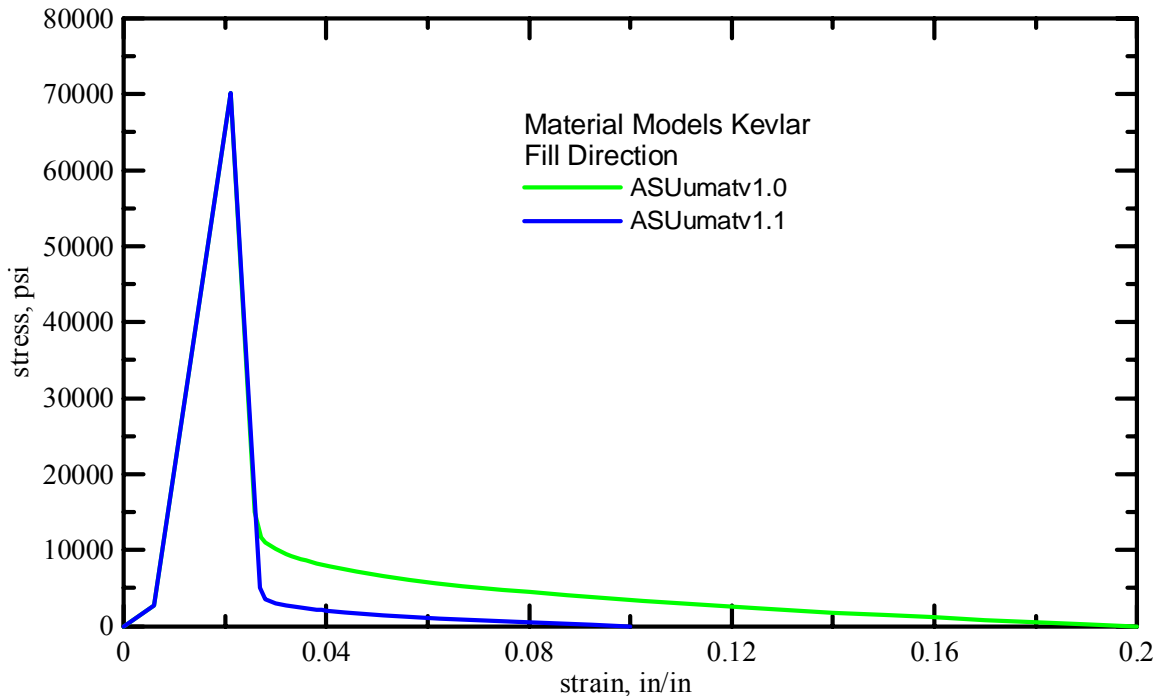


Figure 5.5. Kevlar® 49 warp (11) direction load curves used in ASU material model v1.0 and v1.1

### 5.2.2. Analysis Parameters

The material model discussed above is incorporated into the LS-DYNA finite element program through a user defined material definition (subroutine). Important analysis parameters used in single layer and multi layer FE models in LS-DYNA are listed in Table 5.1 and briefly explained here.

### Contact Type

Automatic contact definition was used to model the contact surfaces in the model. LS-DYNA control card `*CONTACT_AUTOMATIC_SURFACE_TO_SURFACE` was used for this purpose. Since the fabric and the steel ring/projectile have large differences in their respective stiffness and mesh densities, the pinball segment-based contact constraint option was used as recommended by LS-DYNA [LS-DYNA, 2003]. This type



of contact is invoked by supplying a value of 2 for soft variable in the control card as shown in Table 5.1. With this contact option, the contact stiffness is determined based on the time step and nodal masses. Also segment vs. segment contact is checked rather than node vs. segment. After penetrating segments are detected, LS-DYNA designates one of the segments as the master segment and penalty forces are applied normal to that segment. For the contact between fabric and fabric (applicable only for multi layer models) on the ring cutout default method (soft=0) in LS-DYNA is used. This method uses the size of contact segment and its material properties to determine the contact spring stiffness. As this method depends on the material constants and the size of the segments, it works effectively when the material stiffness parameters between the contacting surfaces are of same order of magnitude. Contact between the fabrics on the ring is modeled using pinball segment based contact with soft value of 2 as discussed above. The reason for using this type of contact is that failure of contact definition is observed with soft = 0 during the simulation which accompanied by high negative values of sliding energy. A viscous damping coefficient of 2% of critical was assumed. All other contact parameters were taken as the LS-DYNA default values. All blank values lead to default values being used in the analysis.

#### Coefficient of Friction (FS & FD)

Experimental friction tests of Kevlar<sup>®</sup>49 showed that the coefficient of static and dynamic friction for fabric on fabric was approximately 0.20 [ASU, 2004]. So, a value of 0.2 is used for both coefficient of static friction and dynamic friction between the fabric layers. Since there were no experimental friction tests conducted using Kevlar<sup>®</sup>49 and

steel, the static and dynamic coefficients of friction had to be assumed. Using friction between fabrics as a guide, a value of 0.10 was assumed for both the static and dynamic coefficients of friction between the steel and the fabric

### Shell Theory

The shell element formulation theory used was Belytschko-Tsay with one-point Gaussian integration. The shell normal update option was used and the shell element thickness was kept constant during the analysis. All other shell parameters were taken as the default values.

### Hourglass Properties

Hourglass properties were used for the fabric and the steel elements for each analysis. For the fabric material, the Flanagan-Belytschko stiffness form was used with an hourglass coefficient of 0.10. For the steel material, the Flanagan-Belytschko viscous form was used with an hourglass coefficient of 0.0.

### Time step and accuracy

For each analysis the time step factor used was 0.75. Thus, the actual time step was 75% of the value computed by LS-DYNA. Using this value, no unstable analyses occurred. Second order stress updates and invariant node numbering of shell elements were also used as specified in the \*CONTROL\_ACCURACY card in each analysis as recommended by LS-DYNA for high velocity impact problems.

Table 5.1: Description of important control parameters used in Single layer and Multilayer model developed at ASU

Definition	Single Layer Model	Multilayer Model
Number of FE layers	1	4 fabric layers are represented by 1 FE layer (i.e. 1x4)
<b>HOURGLASS</b>		
<b>fabric</b>		
IHQ	4 (stiffness form hourglass control)	4 (stiffness form hourglass control)
QM	0.1 (hourglass coefficient -default)	0.1 (hourglass coefficient -default)
QB, QW	0.1 (should equal QM)	0.1 (should equal QM)
<b>metal</b>		
<b>HOURGLASS</b>		
IHQ	2 (viscous form hourglass control)	2 (viscous form hourglass control)
QM	0.0 (hourglass coefficient)	0.0 (hourglass coefficient)
IBQ	0 (bulk viscosity type for solids only)	0 (bulk viscosity type for solids only)
QB, QW	0.0 (bending/warping coefficient)	0.0 (bending/warping coefficient)
<b>CONTACT_AUTOMATIC_SURFACE_TO_SURFACE</b>		
SSTYP	3 (Part Id)	3 (Part Id)
FS	0.1 (between steel and fabric)	0.1 (between steel and fabric) 0.2 (between fabric and fabric)
FD	0.1 (between steel and fabric)	0.1 (between steel and fabric) 0.2 (between fabric and fabric)
DT	1.00E+20	1.00E+20
SFS	1.0 (scale factor on penalty stiffness)	1.0 (scale factor on penalty stiffness)
SFM	1.0 (scale factor on penalty stiffness)	1.0 (scale factor on penalty stiffness)
SFST/SFMT	1.0 (default)	1.0 (default)
Card A		
SOFT	2.0 (between steel and fabric)	2.0 (between steel and fabric) 0.0 (between fabrics on ring cutout) 2.0 (between fabrics on the ring)
SOFSCL	0.1 (default)	0.1 (default)
IGAP	1	1
<b>CONTROL_SHELL</b>		
THEORY	2	2
<b>CONTROL_ENERGY</b>		
HGEN	2 (hourglass energy is computed)	2 (hourglass energy is computed)
SLNTEN	2 (sliding energy is computed)	2 (sliding energy is computed)
<b>CONTROL_TIMESTEP</b>		
TSSFAC	0.75	0.75

### 5.2.3. Q A check for simulation

The QA check of simulations can be broadly divided into two parts. First part deals with the checking of model configuration and results against experimental data and second check deals with ensuring numerical stability of simulations.

The geometric models were built using the data reported by NASA-GRC. These models were compared against the experimental test videos available. It was found that although most of the phase II test cases comply with the reported data but the phase I data is questionable. In phase I straight hit of projectile was reported which means the rotational angle about three axes to be zero, however, it was observed that at least five test cases were having non-zero rotational angles these test cases includes LG424, LG427, LG432, LG434 and LG449. Two test cases where the impact angles are different from experimental are shown in Figure 5.6 and Figure 5.7.

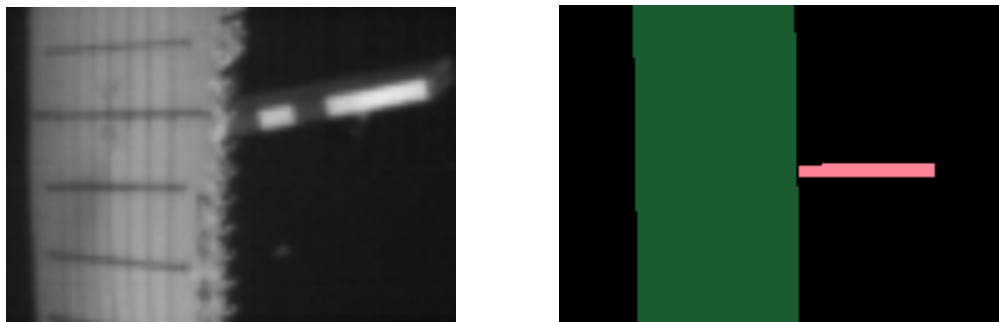


Figure 5.6. Comparison of Experimental and Simulation orientation for LG432

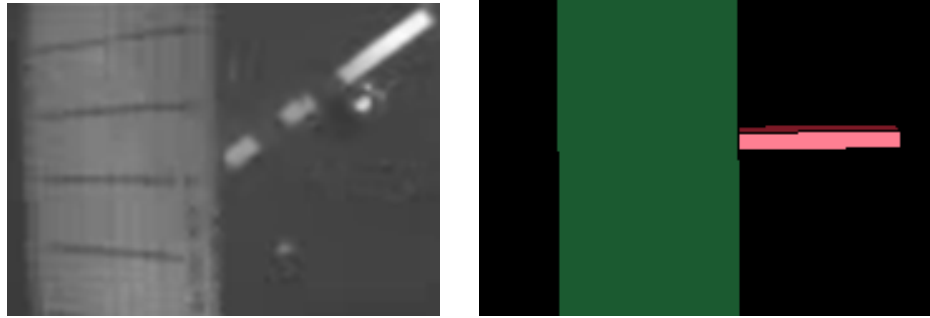


Figure 5.7. Comparison of Experimental and Simulation orientation for LG449

As phase I data has some discrepancies it was analyzed separately from phase II data. The energy absorption predicted by simulation is compared with the energy absorption reported in the experimental plan. A qualitative analysis was also performed to check the failure pattern and deformation before failure of fabric layers.

The numerical stability during the simulation is ensured by conducting following checks. Summary of these tests is shown in Table 5.2.

- 1) Ratio of global kinetic energy/global total energy and global internal energy/global total energy should be less than unity. A ratio of greater than unity indicates the numerical errors.
- 2) Ratio of global hourglass energy/global total energy and global sliding energy/global total energy should be less than 0.1.
- 3) Variation in energy ratio should be less than 0.1 and
- 4) Hourglass energy/total energy for the fabric directly in contact with the projectile should be less than 0.1. To tack hourglass energy of fabric directly in contact with projectile, each layer of fabric is modeled using two parts. One part representing fabric on the ring cutout and other part representing fabric over the solid ring.

Table 5.2: Energy ratios and values used for QA check of simulations

Column Number	Variable Name		Variable Definition	Acceptable limit
1	Test Case		Test Case number	-
2	Fabric Layers		Number of fabric layers in the test case	-
3	Min energy ratio		Minimum ratio of (current total energy)/(initial total energy + external work)	> 0.90
4	Max energy ratio		Maximum ratio of (current total energy)/(initial total energy + external work)	< 1.1
5	Min sliding energy ratio		Minimum ratio of (sliding energy)/(total energy)	> -0.1
6	Max sliding energy ratio		Maximum ratio of (sliding energy)/(total energy)	< 0.1
7	Max kinetic energy ratio		Maximum ratio of (kinetic energy)/(total energy)	< 1.0
8	Max internal energy ratio		Maximum ratio of (internal energy)/(total energy)	< 1.0
9	Hourglass energy ratio	Global	Maximum ratio of (global hourglass energy)/(global total energy)	< 0.1
10		Fabric	Maximum ratio of (hourglass energy)/(total energy) for fabric directly in contact with projectile for single layer model.	< 0.1

### 5.3. Single FE layer ballistic test simulations

#### 5.3.1. Finite Element Model

Shell elements were used to represent the fabric and solid elements were used to represent the steel ring and steel projectiles. The fabric was modeled with a uniform mesh containing 0.25" shell elements. The steel ring was modeled with 0.25" x 0.25" x 1.0" hexagonal elements (1.0" through the ring thickness) since the ring is not of interest with respect to the FE analysis results. One layer of shell elements was used to represent the fabric irrespective of the actual number of fabric layers. Thus for an 8-layer test case, the shell element thickness was taken as the thickness of one fabric layer multiplied by 8, or 0.011" x 8 = 0.088". With this methodology, the friction between the fabric layers is not captured. In the model the center of the shell elements was placed at a distance of one

half the shell element thickness away from the ring facilitating contact between the shell elements and the ring at the start of the analysis.

The fabric model was meshed using two different parts. The fabric directly in contact with penetrator is given separate part id than rest of the fabric. This type of configuration facilitates tracing of energy balance for this area separately. Figure 5.8 shows the typical ring and fabric model used for these simulations.

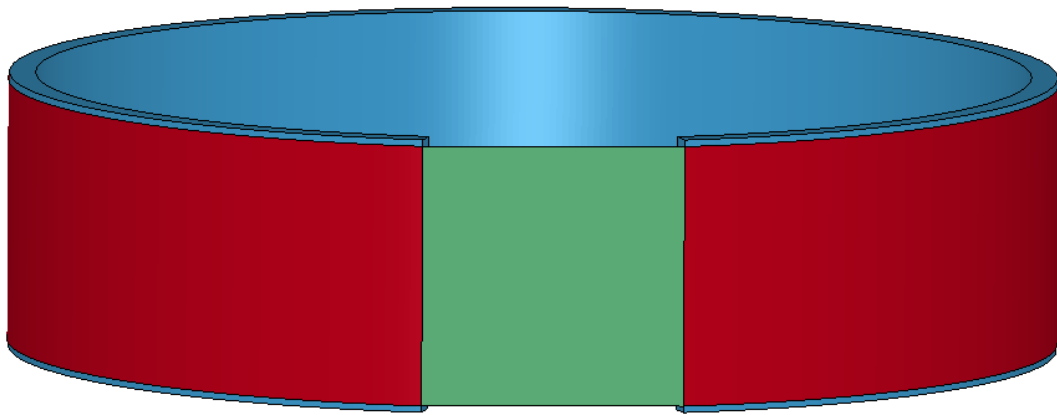


Figure 5.8. Single FE layer ballistic test model

### 5.3.2. Results and Discussion

Table 5.3 shows a comparison between the absorbed energy during experiment and its corresponding LS-DYNA simulation. The absolute % difference values shown in the table were computed based on following formula.

$$\% \text{ Diff.} = (\text{Exp. Absorbed Energy } \%) - (\text{Sim. Absorbed Energy } \%) \quad (5.1)$$

Hence a positive % difference corresponds to the FE simulation under predicting the absorbed energy and a negative % difference corresponds to the FE simulation over predicting the absorbed energy.

Table 5.3: Absorbed energy of fabric for experimental ballistic tests and simulations

File Run	Fabric Layers	NASA TEST						SIMULATIONS						Absolute % difference
		Before Impact		After Impact		Absorbed Energy		Before Impact		After Impact		Absorbed Energy		
		Velocity	Energy	Velocity	Energy	(J)	%	Velocity	Energy	Velocity	Energy	(J)	%	
		(ft/sec)	(J)	(ft/sec)	(J)	(J)	%	(ft/sec)	(J)	(ft/sec)	(J)	(J)	%	%
LG403	4	899	11952	846.5	10597	999	11.3	899.2	11852	864.9	10964	888	7.5	3.8
LG404	8	895.7	11843	820.2	9931	1911	16.1	895.8	11764	802.7	9443	2321	19.7	-3.6
LG405	24	899	11975	495.4	3637	6150	69.6	899.2	11852	0	0	11852	100	-30.4
LG409	8	889.1	11604	807.1	9562	1506	17.6	889.2	11590	797.5	9324	2266	19.6	-2
LG410	4	912.1	12226	866.1	11026	885	9.8	911.7	12183	892.4	11675	508	4.2	5.6
LG411	24	885.8	11474	413.4	2499	8976	78.2	885.8	11503	495.1	3604	7899	68.7	9.6
LG424	8	833.3	10352	744.8	8268	1537	20.1	833.3	10180	716.1	7519	2661	26.1	-6
LG427	24	915.4	12373	607	5440	5113	56	915	12273	599.9	5288	6985	56.9	-0.9
LG429	16	915.4	12307	718.5	7583	3484	38.4	915	12273	672.8	6638	5635	45.9	-7.5
LG432	16	895.7	11925	649.6	6273	5652	47.4	895.8	11764	651.7	6234	5529	47	0.4
LG433	1	390.4	2242	367.5	1986	189	11.4	390.4	2234	274.3	1104	1130	50.6	-39.2
LG434	1	383.9	2162	360.9	1911	185	11.6	383.8	2160	312.4	1431	729	33.8	-22.1
LG444	2	347.8	1778	277.9	1135	474	36.1	347.8	1773	121.7	223	1549	87.4	-51.2
LG449	2	344.5	1743	278.9	1142	443	34.5	344.4	1739	119.3	215	1524	87.6	-53.2
LG594	8	843.9	10147	484.5	3345	6802	67	844.3	10377	368.7	2217	8160	78.6	-11.6
LG609	8	913.7	12110	825.4	9883	2228	18.4	914.3	12169	853.3	10606	1564	12.8	5.5
LG610	8	888.1	11440	809.7	9510	1931	16.9	888.4	11492	789.9	9108	2384	20.7	-3.9
LG611	8	905.7	12348	798.1	9588	2760	22.4	905.8	12026	846.8	10513	1513	12.6	9.8
LG612	8	898.3	12146	822.7	10190	1957	16.1	898.3	11829	803.5	9466	2363	20	-3.9
LG618	8	866.4	10889	558.9	4531	6358	58.4	866.8	10937	470	3386	7552	69	-10.7
LG620	8	893.8	11735	580.8	4954	6780	57.8	894.3	11643	670.7	6647	4995	42.9	14.9
LG655	32	1131.7	19281	830.6	10386	8895	46.1	1131.7	18772	1016.6	15150	3622	19.3	26.8
LG656	32	967.3	14086	469.2	3315	10771	76.5	967.5	13721	626.9	5764	7956	58	18.5
LG657	32	829.7	10363	0	0	10363	100	829.6	10090	0	0	10090	100	0
LG689	8	896.3	12061	655.1	6443	5618	46.6	896.7	11785	697.6	7214	4571	38.8	7.8
LG692	8	885.3	11799	602.6	5466	6333	53.7	885	11480	661.3	6515	4966	43.3	10.4



Table 5.4 shows statistics of the results including the average % difference between the simulations and the experimental tests, the maximum % difference or largest under prediction between the simulations and the experimental tests, the minimum % difference or largest over prediction between the simulations and the experimental tests, and the standard deviation of the % difference between the simulations and the experimental tests for both versions 1.0 and 1.1.

Table 5. 4: Statistics for absorbed energy % difference between simulations and experiments

	ASUumatv1.0			ASUumatv1.1		
	Phase I	Phase II	Overall	Phase I	Phase II	Overall
NUMBER:	14	12	26	14	12	26
AVG:	-13.1%	7.0%	-3.8%	-14.0%	5.3%	-5.1%
MAX:	9.2%	29.5%	29.5%	9.6%	26.8%	26.8%
MIN:	-49.8%	-19.1%	-49.8%	-53.2%	-11.6%	-53.2%
STDEV:	19.1%	15.4%	19.9%	21.5%	11.7%	19.8%

It is interesting to note from Table 5.4 that if all the 26 test cases are considered for the analysis the ASUumatv1.0 is slightly better than ASUumatv1.1 in terms of average difference in results however, if only phase II results are compared then later the version ASUumat1.1 outperformed ASUumatv1.0 both in terms of average difference in energy absorption and standard deviation in the results. It is phase I data which is offsetting overall results in both the versions and since Phase I data under scanner it is more appropriate to compare and judge two material versions based on Phase II data. Further, it was observed that both the versions are having problem with prediction of

energy absorbed for test cases where less than or equal to 2 layers of fabric were used and projectile speed is lesser than 500 ft/sec. Table 5.5 summaries the results from both the versions where fabric layer less than or equal to 2 are used i.e. test cases LG433, LG434, LG444 and LG449.

Table 5.5: Statistics for absorbed energy % difference between simulations and experiments for test cases LG433, LG434, LG444 and LG449

	ASUumatv1.0	ASUumatv1.1
NUMBER:	4	4
AVG:	-33%	-41%
MAX:	-17%	-22%
MIN:	-50%	-53%
STDEV:	18%	14%

So, out of 26 test cases, 4 test cases are poorly performed by both the versions. Table 5.6 shows the statistics of the results without these four test cases mentioned above. It is observed that in the test cases where the number of fabric layers are more than or equal to 4, version 1.1 out performs the version 1.0 for average % difference, max % difference i.e. under prediction and standard deviation in the test results.

Table 5.6 Statistics for absorbed energy % difference between simulations and experiments after removal of test cases LG433, LG434, LG444 and LG449

	ASUumatv1.0	ASUumatv1.1
NUMBER:	22	22
AVG:	2%	1%
MAX:	29%	27%
MIN:	-30%	-30%
STDEV:	15%	12%

### 5.3.3. Q A Check

The QA checks for the energy ratios are shown in Table 5.7. It can be observed that these ratios look good and are well within the range except for 2 test cases out of 26 test cases where hourglass energy is observed to be higher than 10% of total energy. The detailed study of these test cases revealed that these are the special cases where simulations are contained. In these test cases high hourglass energy is observed when projectile velocity becomes near to zero. So, it can be concluded that the energy ratio for single layer models are satisfactory and there is no numerical instability or breakage of contact formulation observed.

Table 5.7 QA check of single FE layer models

Test Case (1)	Fabric Layers (2)	Min energy ratio (3)	Max energy ratio (4)	Min sliding energy ratio (5)	Max sliding energy ratio (6)	Max kinetic energy ratio (7)	Max internal energy ratio (8)	Hourglass energy ratio – Global (9)	Hourglass energy ratio – Fabric (10)
LG403	4	1	1	0	0.0014	1	0.016	0.0009	0.0193
LG404	8	0.9999	1.0001	0	0.0055	1	0.0488	0.0044	0.0179
LG405	24	1	1.0389	0	0.079	1	0.2418	0.1344	0.1544
LG409	8	0.9997	1	0	0.0051	1	0.0469	0.0041	0.0186
LG410	4	0.9999	1	0	0.001	1	0.0091	0.0011	0.0339
LG411	24	0.9988	1	0	0.018	1	0.2087	0.0408	0.0713
LG424	8	0.9993	1.0005	0	0.0072	1	0.0662	0.006	0.0267
LG427	24	0.9978	1	0	0.0143	1	0.1667	0.0475	0.0804
LG429	16	0.9987	1.0001	0	0.0114	1	0.1148	0.0166	0.0311
LG432	16	0.9983	1.0001	0	0.0136	1	0.1212	0.0186	0.0349
LG433	1	0.9986	1.0002	-0.008	0.0057	1	0.2833	0.0144	0.0603
LG434	1	0.9998	1	0	0.0067	1	0.1606	0.009	0.0094
LG444	2	0.9962	1.0003	0	0.0622	1	0.5478	0.0216	0.0168
LG449	2	0.9994	1.0008	0	0.0444	1	0.6823	0.02	0.0547
LG594	8	0.9988	1.1794	0	0.0562	1	0.2218	0.0588	0.0668
LG609	8	0.999	1	0	0.0015	1	0.0332	0.0031	0.025
LG610	8	0.9996	1.0001	0	0.0029	1	0.0458	0.0033	0.02
LG611	8	0.9997	1	0	0.0028	1	0.0305	0.003	0.0303
LG612	8	0.9995	1.0001	0	0.0052	1	0.0497	0.0056	0.0246
LG618	8	0.9999	1.0199	0	0.0413	1	0.1861	0.0533	0.0495
LG620	8	0.9988	1.0047	-0.0006	0.0129	1	0.1089	0.036	0.0383
LG655	32	0.9991	1	0	0.0036	1	0.0478	0.0078	0.0601
LG656	32	0.9961	1	0	0.0302	1	0.1594	0.0673	0.064
LG657	32	1	1.0021	0	0.063	1	0.3518	0.1146	0.3037
LG689	8	0.9985	1.0001	0	0.011	1	0.0773	0.0204	0.0525
LG692	8	0.9962	1.0001	0	0.0096	1	0.082	0.0281	0.0507

#### 5.3.4. Regression Model

In order to analyze different parameters affecting the difference between the simulation and experimental energy absorption, a regression model was developed in which absolute difference between % energy absorbed during experimental and simulation was considered as predictor and four variables i.e. initial velocity, number of fabric layers, impact angle, penetrator type and their interactions were considered as predictor variable. Minitab<sup>®</sup> 14 was used to analyze this model. Table 5.8 shows the different parameters used in regression analysis.

Table 5.8 Variables used in regression analysis

Variable Type	Term	Notation	Description
Predictor	Penetrator Type	PT	0 – Thick Penetrator (Old) 1 – Thin Penetrator (New)
Predictor	Impact Angle	IA	0 – Straight Hit 1 – Oblique Hit
Predictor	# Fabric layers	FL	Represents number of fabric layers
Predictor	Velocity	V	Velocity of penetrator in ft/sec
Response	% Energy absorbed (exp. – Simulation)	DIF	Represents difference in % energy absorbed in experiment – simulation

The final equation of regression is:-

$$\text{DIF} = -80.0 + 0.0895 V + 0.00712 \text{ IA} * V \quad (5.2)$$

This regression model has  $R^2$  of 94.2% and  $R^2$  (adj) of 93.5%. So, over 90% of variability in the data can be explained by the model. Figure 5.9 shows the scatter plot of response variable against predictor variables.

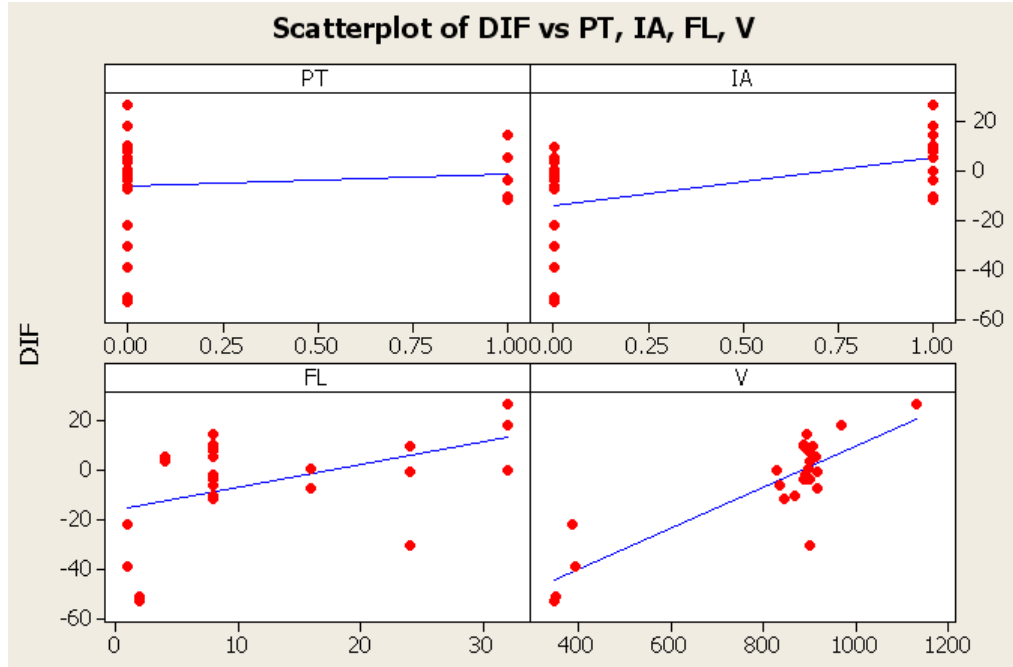


Figure 5.9. Scatter plot for single layer model

Following points can be observed from the regression analysis of single FE layer model of ballistic simulations:-

- The difference between experimental and simulation results is dominated by the velocity of the projectile.
- There is only one test for velocity above 1000ft/sec and test cases at lower velocities (in the range of 300-400 ft/sec) are with only single layer or two layers of fabric.
- The test case at high velocity is under predicted and test cases at lower velocity are over predicted. So, to improve single layer model for the wide range of velocity, there is a need to study strain rate dependence of Kevlar in detail.

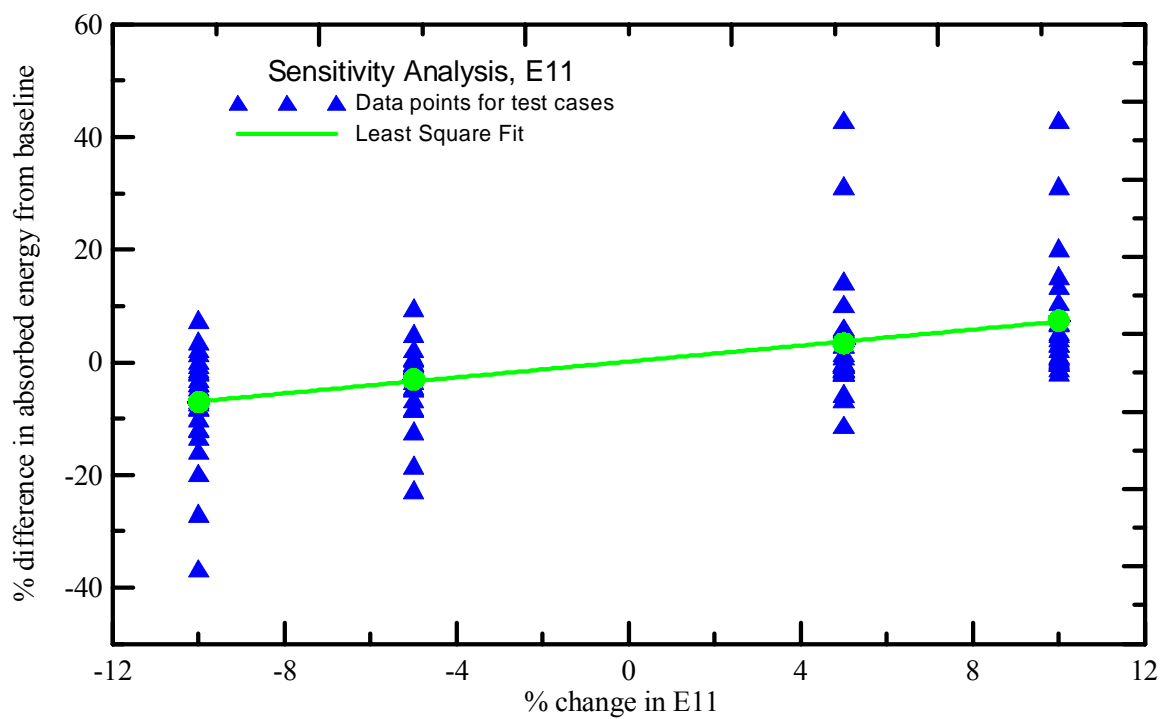
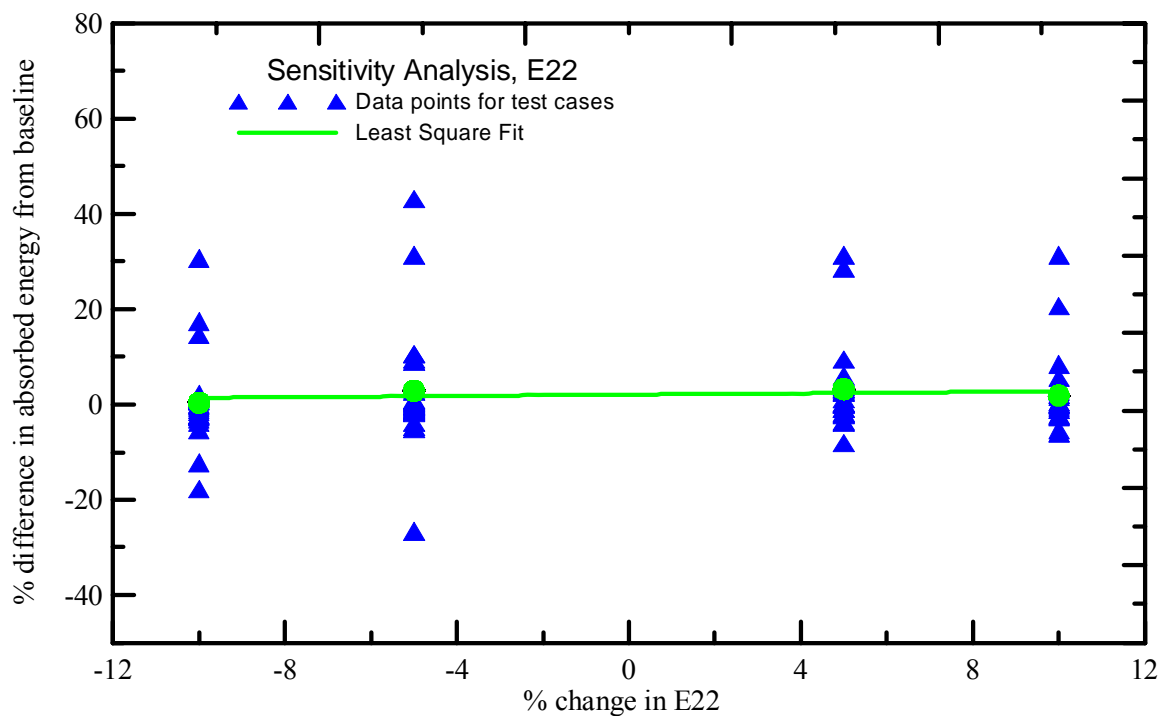
### 5.3.5. Sensitivity Analysis

A sensitivity analysis of the material model was performed to determine the single FE layer model's sensitivity to various input parameters. These parameters included the elastic moduli ( $E_{11}$  and  $E_{22}$ ), the shear moduli ( $G_{12}$ ,  $G_{23}$ , and  $G_{31}$ ), the failure strain, the coefficient of friction and the projectile orientation. For parameters that were taken from experimental results, such as  $E_{11}$  and  $E_{22}$ , the values were adjusted by -10%, -5%, +5%, and +10%. For other parameters that were assumed in the material model, such as coefficient of friction and the failure strain, lower and higher values than the assumed values were used. All 26 test cases were used for the sensitivity analysis.

Reported are the % difference values between the simulations using the actual values and the simulations using the adjusted values. A positive difference indicates a lower absorbed energy using the adjusted value and a negative difference indicates a higher absorbed energy using the adjusted value. For the parameters that were adjusted by a % the average difference values are shown on the plot and are connected by a line to show the general trend.

#### Sensitivity of Material Model to $E_{11}$ and $E_{22}$

The values for  $E_{11}$  and  $E_{22}$  were adjusted by -10%, -5%, -1%, +1%, +5%, and +10% and simulations of all the test cases were run. Figures 5.10 and 5.11 show the results.

Figure 5.10. Sensitivity of material model to  $E_{11}$ Figure 5.11. Sensitivity of material model to  $E_{22}$



### Sensitivity of Material Model to $G_{12}$

The value for  $G_{12}$  was adjusted by -10%, -5%, +5%, and +10% and simulations of all the cases were run. Figure 5.12 shows the results.

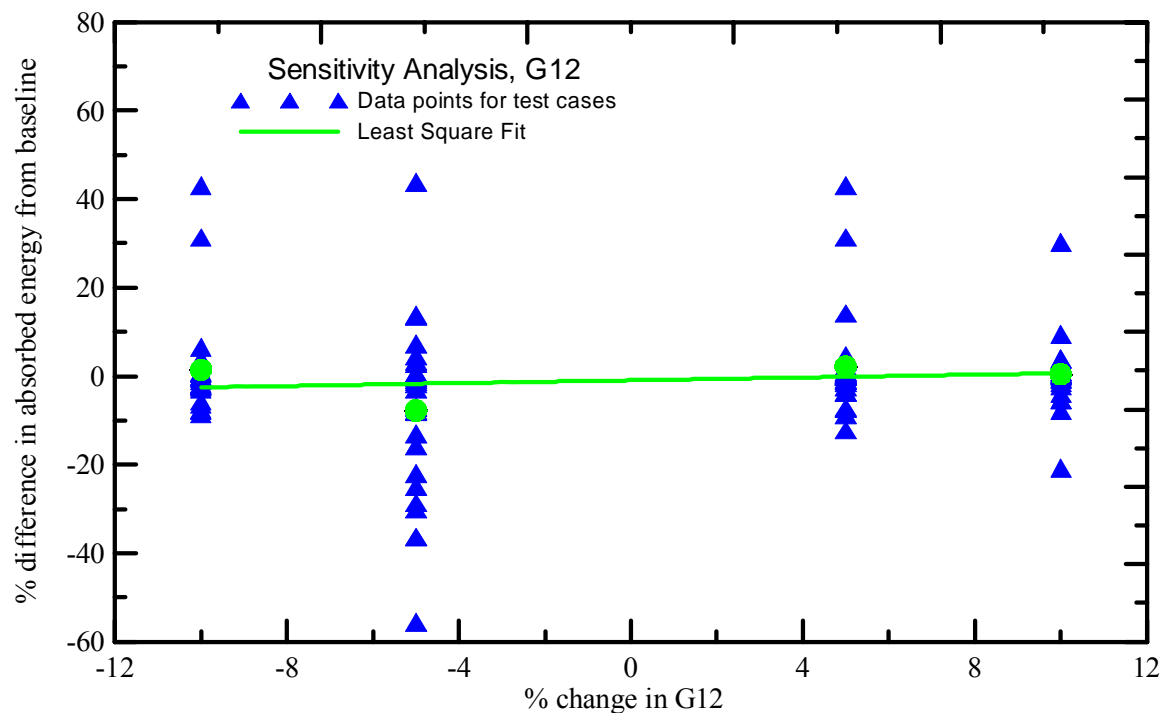


Figure 5.12. Sensitivity of material model to  $G_{12}$

### Sensitivity of Material Model to the Coefficient of Friction

The static and dynamic coefficient of friction for steel on fabric used in the material model was 0.10. Simulations of all the test cases were run using different values – 0.0, 0.05, 0.15, and 0.20. Figure 5.13 shows the results.

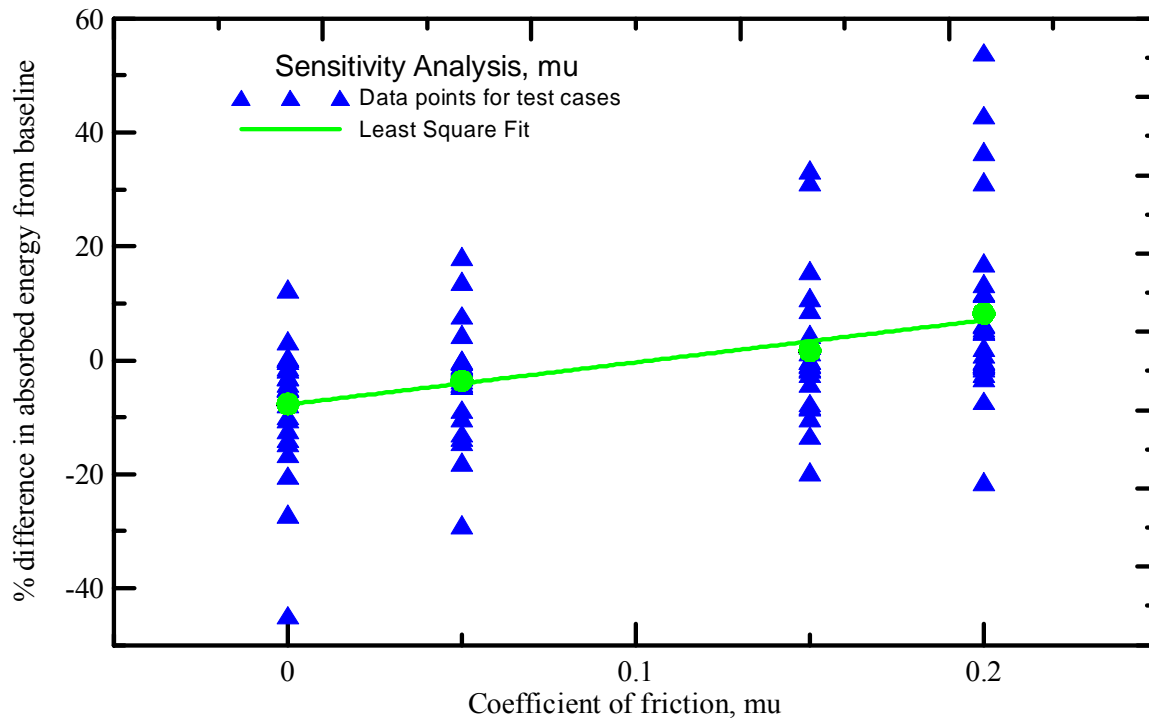


Figure 5.13. Sensitivity of material model to the coefficient of friction

#### Sensitivity of Material Model to the Failure Strain

The failure strain used in the material model was 0.10 for both the warp and fill directions. Simulations of all the test cases were run using alternative values of 0.05 and 0.15 and 0.20. Figure 5.14 shows the results.

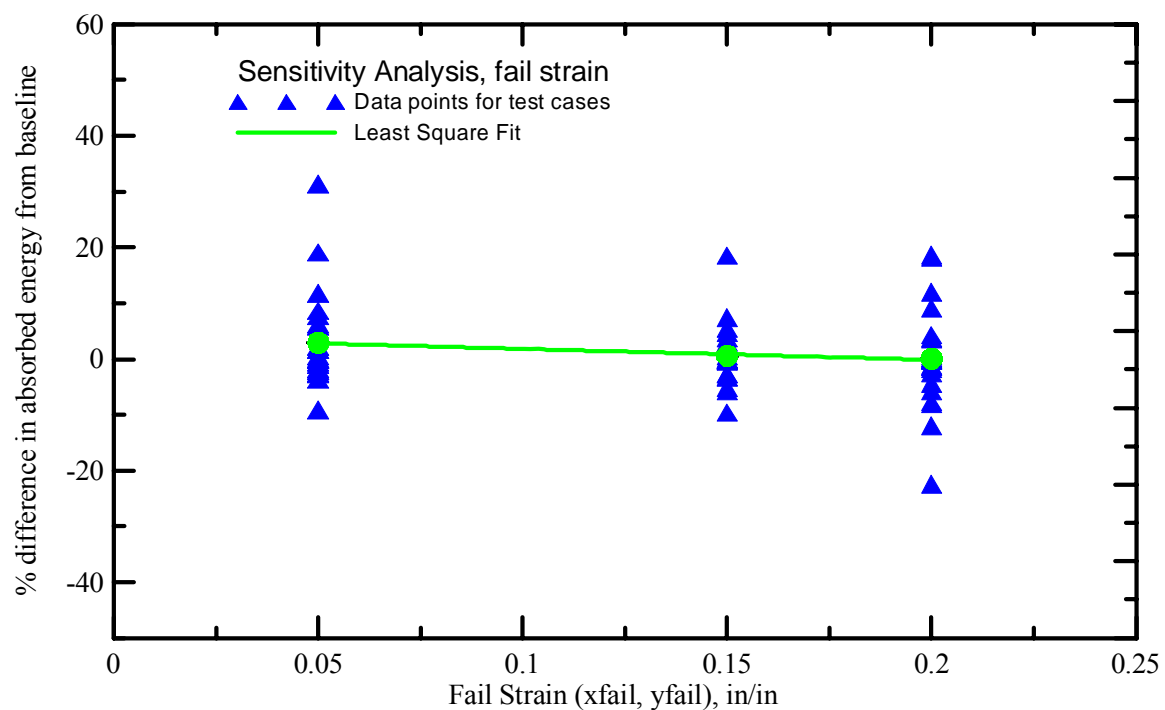


Figure 5.14. Sensitivity of material model to failure strain

#### Sensitivity of Material Model to the $G_{23}$ and $G_{31}$

The out of plane shear modulus ( $G_{23}$  and  $G_{31}$ ) used in the material model was 50,000 psi. Simulations of all the test cases were run using alternative values of 40,000 psi and 60,000 psi. Figure 5.15 shows the results.

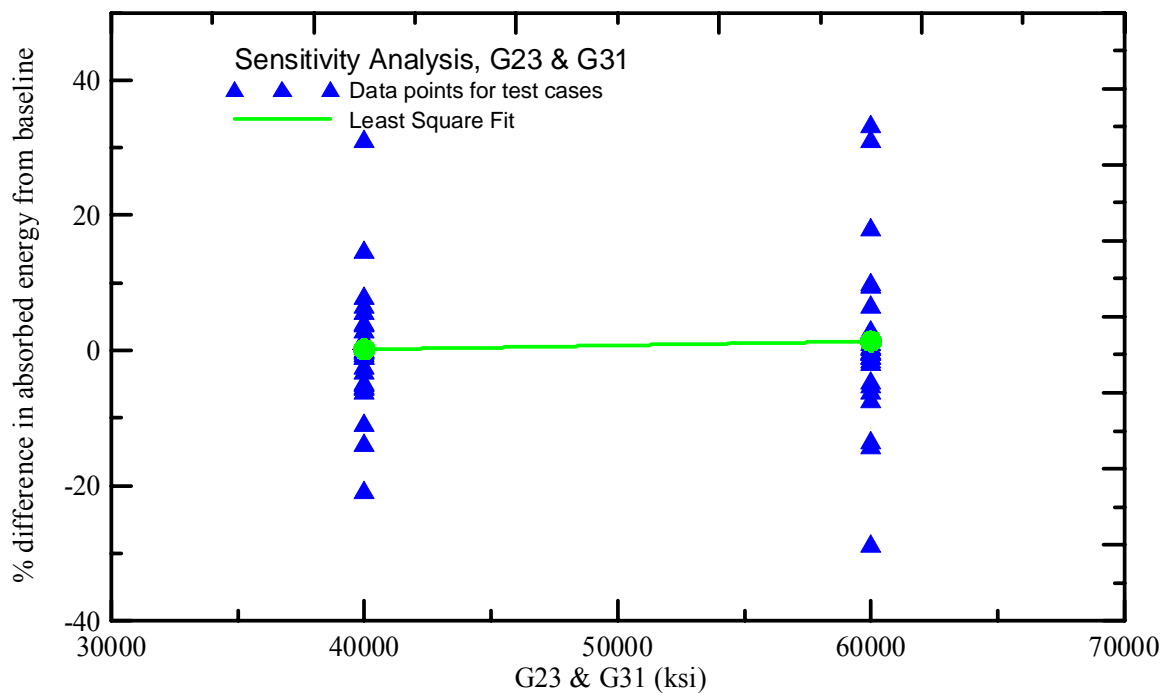
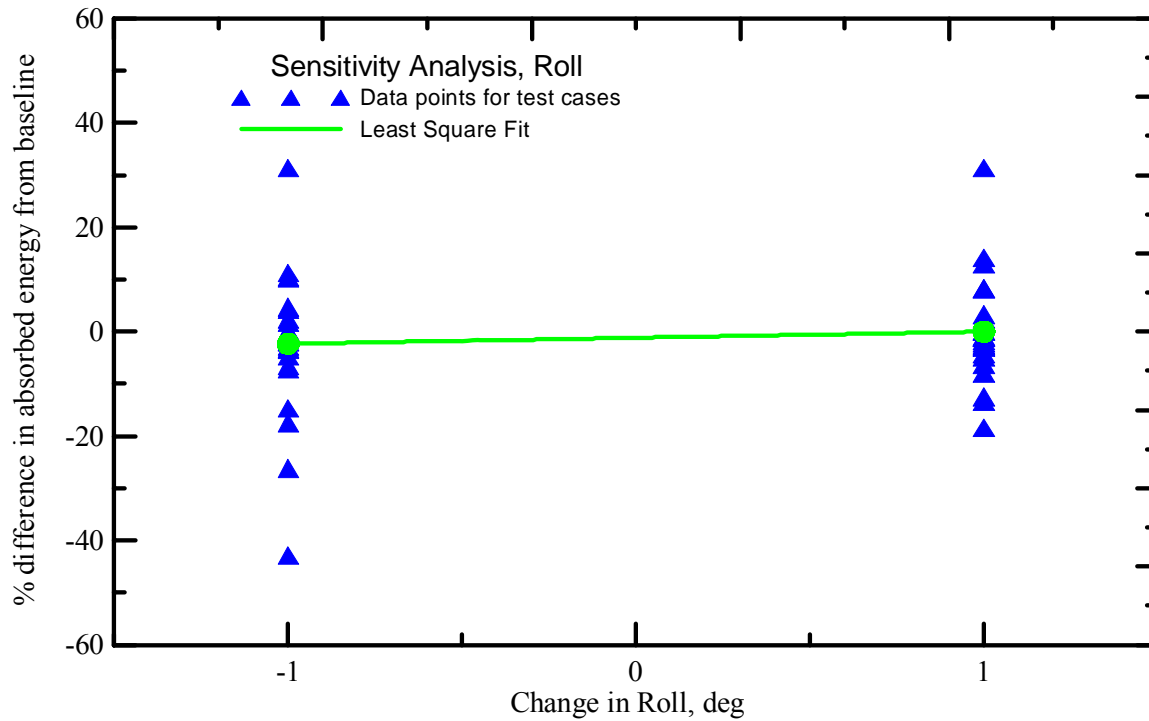
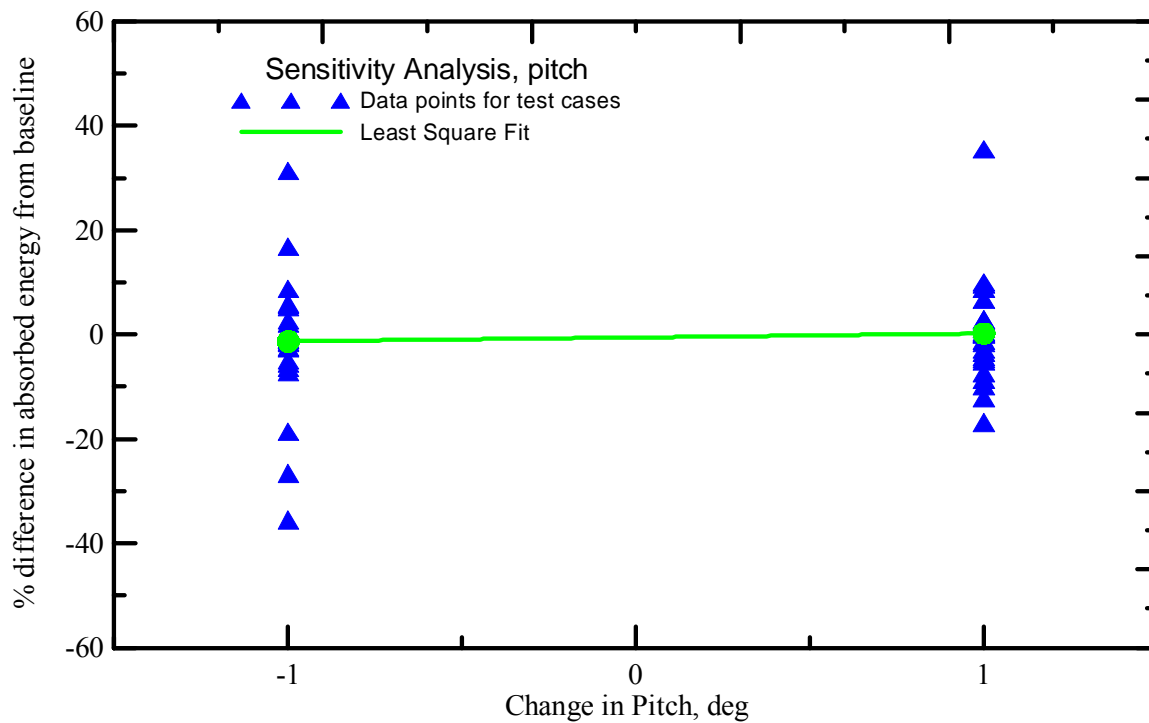


Figure 5.15. Sensitivity of material model to  $G_{23}$  and  $G_{31}$

#### Sensitivity of Material Model to the projectile orientation

The orientation of the projectile along the three axes i.e. roll, pitch and yaw were varied by +1 deg and -1 deg. Figure 5.16 to 5.18 shows the results obtained for roll, pitch and yaw sensitivity respectively.

Figure 5.16. Sensitivity of material model to *Roll*Figure 5.17. Sensitivity of material model to *Pitch*

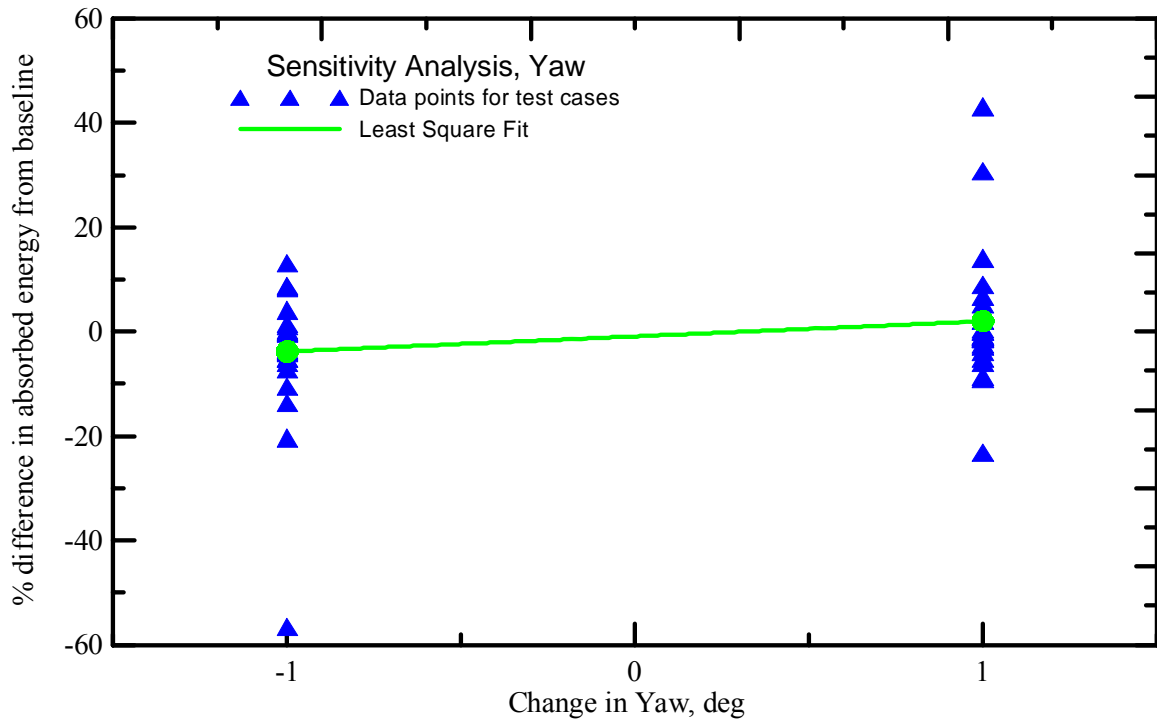


Figure 5.18. Sensitivity of material model to *Yaw*

From sensitivity analysis it can be concluded that the model is very sensitive to warp direction young's modulus ( $E_{11}$ ) and coefficient of friction between steel and fabric. Fail strain used in the model is also has moderate effect on the simulation results however, other parameters like shear modulus and stiffness of fabric in fill direction has very low sensitivity effect. It is interesting to note that these conclusions are based on the average values for 26 test cases, individual test cases vary tremendously in their behavior. Some of the test cases are very sensitive to even shear modulus.

## 5.4. Multi FE layer ballistic test simulation

### 5.4.1. Finite Element Model

Shell elements were used to represent the fabric and solid elements were used to represent the steel ring and steel projectiles. The fabric was modeled with a uniform mesh containing 0.25" shell elements. The steel ring was modeled with 0.25" x 0.25" x 1.0" hexagonal elements (1.0" through the ring thickness) since the ring is not of interest with respect to the FE analysis results. One layer of shell elements was used to represent the four fabric layers. Thus for an 8- fabric layer test case, there will be two finite element layers with shell element thickness of one fabric layer multiplied by 4, or  $0.011" \times 4 = 0.044"$ . With this methodology, the friction between the fabric layers can also be captured.

In the model the center of the shell elements was placed at a distance of one half the shell element thickness away from the ring and one shell element away from adjacent shell layer to facilitating contact between them at the start of the analysis. Figure 5.19 shows the FE mesh of the ring and the fabric for 16 fabric layer (4 FE layer) model.

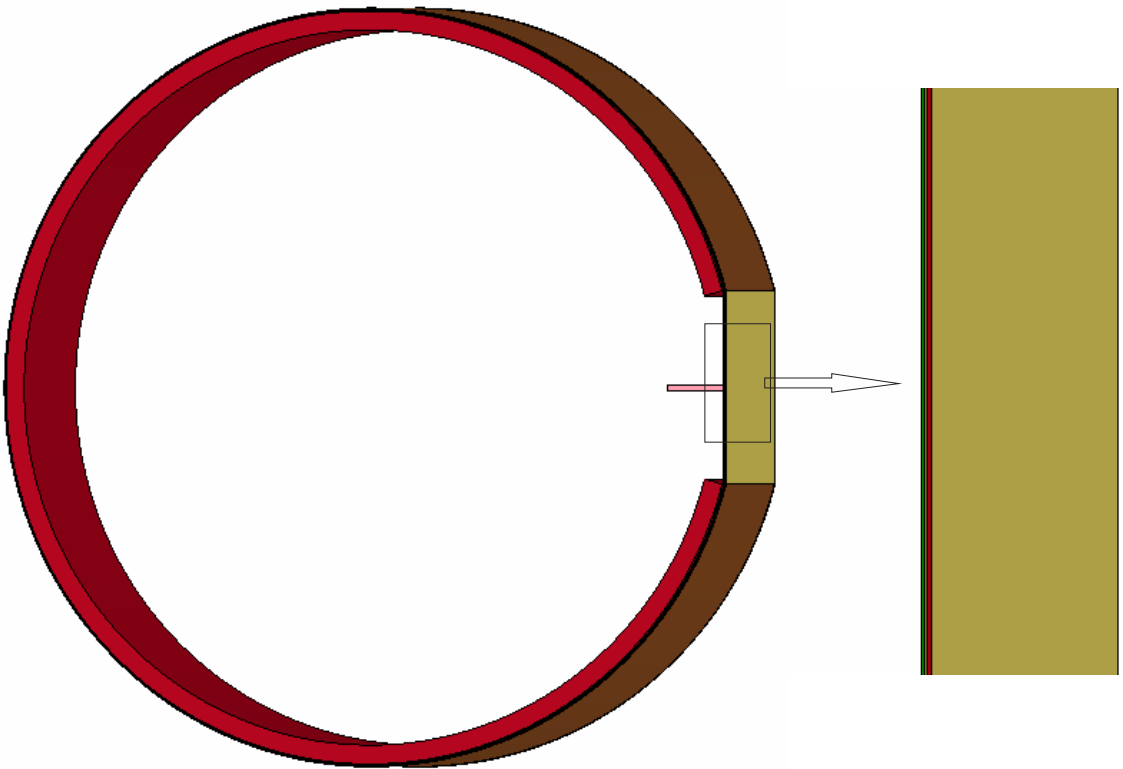


Figure 5.19. Multi FE layer ballistic test model

#### 5.4.2. Results and Discussion

Table 5.9 shows a comparison between the absorbed energy of the fabric for each experimental test case and its corresponding LS-DYNA simulation result. The absolute % difference values shown in the table were computed based on following formula.

$$\% \text{ Diff.} = (\text{Exp. Absorbed Energy } \%) - (\text{Sim. Absorbed Energy } \%) \quad (5.3)$$

Hence a positive % difference corresponds to the FE simulation under predicting the absorbed energy and a negative % difference corresponds to the FE simulation over predicting the absorbed energy.



Table 5.9: Absorbed energy of fabric for experimental ballistic tests and simulations

File Run	Fabric Layers	NASA TEST						SIMULATIONS						Absolute % difference
		Before Impact		After Impact		Absorbed Energy		Before Impact		After Impact		Absorbed Energy		
		Velocity	Energy	Velocity	Energy			Velocity	Energy	Velocity	Energy			
		(ft/sec)	(J)	(ft/sec)	(J)	(J)	(%)	(ft/sec)	(J)	(ft/sec)	(J)	(J)	(%)	
LG404	8	895.7	11843	820.2	9931	1911	16.1	895.8	11764	805.1	9505	2259	19.2	-3.1
LG405	24	899	11975	495.4	3637	6150	69.6	899.2	11852	560.2	4613	7239	61.1	8.5
LG409	8	889.1	11604	807.1	9562	1506	17.6	889.2	11590	795.4	9276	2314	20	-2.4
LG411	24	885.8	11474	413.4	2499	8976	78.2	885.8	11503	526.1	4077	7426	64.6	13.7
LG424	8	833.3	10352	744.8	8268	1537	20.1	833.3	10180	733.6	7891	2289	22.5	-2.4
LG427	24	915.4	12373	607	5440	5113	56	915	12273	647.8	6159	6114	49.8	6.2
LG429	16	915.4	12307	718.5	7583	3484	38.4	915	12273	806.7	9536	2737	22.3	16.1
LG432	16	895.7	11925	649.6	6273	5652	47.4	895.8	11764	679.6	6778	4986	42.4	5
LG609	8	913.7	12110	825.4	9883	2228	18.4	914.3	12169	881.5	11316	853	7	11.4
LG610	8	888.1	11440	809.7	9510	1931	16.9	888.4	11492	802.7	9388	2104	18.3	-1.4
LG611	8	905.7	12348	798.1	9588	2760	22.4	905.8	12026	838.8	10317	1709	14.2	8.1
LG612	8	898.3	12146	822.7	10190	1957	16.1	898.3	11829	799.9	9385	2444	20.7	-4.6
LG618	8	866.4	10889	558.9	4531	6358	58.4	866.8	10937	0	0	10937	100	-41.6
LG655	32	1131.7	19281	830.6	10386	8895	46.1	1131.7	18772	1020.7	15273	3499	18.6	27.5
LG656	32	967.3	14086	469.2	3315	10771	76.5	967.5	13721	447	3184	10537	76.8	-0.3
LG657	32	829.7	10363	0	0	10363	100	829.6	10090	0	0	10090	100	0
LG692	8	885.3	11799	602.6	5466	6333	53.7	885	11480	768.5	8681	2799	24.4	29.3
LG594	8	843.9	10147	484.5	3345	6802	67	844.3	10377	504.5	3766	6611	63.7	3.3
LG689	8	896.3	12061	655.1	6443	5618	46.6	896.7	11785	745.5	8172	3613	30.7	15.9

Table 5.10 shows statistics of the results including the average difference between the simulations and the experimental tests, the maximum difference or largest under prediction between the simulations and the experimental tests, the minimum difference or largest over prediction between the simulations and the experimental tests, and the standard deviation of the difference between the simulations and the experimental tests for multilayer model with version 1.1.

Table 5.10 Statistics for absorbed energy difference between simulations and experiments

	ASUumatv1.1		
	Phase I	Phase II	Overall
NUMBER:	8	12	20
AVG:	5.2%	4.7%	4.7%
MAX:	16.1%	29.3%	29.3%
MIN:	-3.1%	-41.6%	-41.6%
STDEV:	7.4%	18.2%	14.9%

#### 5.4.3. Q A Check

Different energy ratios are shown in Table 5.11. It can be observed that overall these ratios look good and are well within the range except for 2 test cases out of 20 test cases where hourglass energy is observed to be higher than 10% of total energy. The detailed study of these test cases revealed that these cases (LG618 and LG 657) are the special cases where simulations are contained. In these test cases high hourglass energy is observed when projectile velocity becomes near to zero. So, it can be concluded that the energy ratios for multi FE layer models are satisfactory.

Table 5.11 QA check of multi FE layer models

Test Case (1)	Fabric Layers (2)	Min energy Ratio (3)	Max energy ratio (4)	min sliding energy ratio (5)	max sliding energy ratio (6)	max kinetic energy ratio (7)	max internal energy ratio (8)	Hourglass energy ratio								
								Global (9)	1st FE layer (10)	2nd FE layer (11)	3rd FE layer (12)	4th FE layer (13)	5th FE layer (14)	6th FE layer (15)	7th FE layer (16)	8th FE layer (17)
LG404	8	0.9998	1	0	0.004	1	0.047	0.003	0.015	0.024	0	0	0	0	0	0
LG405	24	0.9987	1	-0.011	0.016	1	0.203	0.027	0.042	0.058	0.045	0.035	0.037	0.035	0	0
LG409	8	0.9995	1	0	0.006	1	0.053	0.004	0.021	0.013	0	0	0	0	0	0
LG411	24	0.9987	1.0001	-0.008	0.016	1	0.202	0.024	0.039	0.036	0.039	0.027	0.03	0.027	0	0
LG424	8	0.9995	1	0	0.006	1	0.061	0.005	0.02	0.018	0	0	0	0	0	0
LG427	24	0.9977	1	-0.006	0.012	1	0.149	0.016	0.045	0.041	0.024	0.022	0.023	0.024	0	0
LG429	16	0.9996	1	0	0.009	1	0.052	0.003	0.015	0.021	0.021	0.028	0	0	0	0
LG432	16	0.9989	1.0001	0	0.013	1	0.118	0.014	0.046	0.029	0.023	0.023	0	0	0	0
LG594	8	0.9997	1.0041	-0.001	0.031	1	0.172	0.037	0.038	0.043	0	0	0	0	0	0
LG609	8	0.9999	1	0	0	1	0.006	0	0.022	0.018	0	0	0	0	0	0
LG610	8	1	1	0	0.002	1	0.035	0.003	0.021	0.015	0	0	0	0	0	0
LG611	8	0.9995	1	0	0.004	1	0.032	0.002	0.028	0.033	0	0	0	0	0	0
LG612	8	0.9999	1.0001	0	0.004	1	0.042	0.002	0.018	0.015	0	0	0	0	0	0
LG618	8	1	1.0332	-0.013	0.057	1	0.521	0.079	0.459	0.173	0	0	0	0	0	0
LG620	8	0.9997	1.0021	0	0.026	1	0.115	0.024	0.033	0.022	0	0	0	0	0	0
LG655	32	0.9979	1	0	0.018	1	0.053	0.003	0.099	0.04	0.038	0.018	0.025	0.02	0.022	0.023
LG656	32	0.9996	1.0091	-0.062	0.034	1	0.264	0.032	0.081	0.072	0.106	0.043	0.063	0.068	0.073	0.078
LG657	32	0.9996	1.0144	-0.274	0.027	1	0.506	0.058	0.142	0.115	0.109	0.107	0.154	0.159	0.145	0.157
LG689	8	0.9991	1.0014	0	0.015	1	0.065	0.011	0.024	0.025	0	0	0	0	0	0
LG692	8	0.9995	1.0001	0	0.006	1	0.057	0.01	0.048	0.02	0	0	0	0	0	0

#### 5.4.4. Regression Model

In order to analyze different parameters affecting the difference between the simulation and experimental energy absorption, a regression model was developed in which absolute difference between % energy absorbed during experimental and simulation was considered as predictor and four variables i.e. initial velocity, number of fabric layers, impact angle, penetrator type and their interaction were considered as predictor variables. Minitab<sup>®</sup> 14 was used to analyze this model. Table 5.12 shows the different parameters used in regression analysis and Figure 5.17 shows the scatter plot.

Table 5.12 Variables used in regression analysis

Variable Type	Term	Notation	Description
Predictor	Penetrator Type	PT	0 – Thick Penetrator (Old) 1 – Thin Penetrator (New)
Predictor	Impact Angle	IA	0 – Straight Hit 1 – Oblique Hit
Predictor	# Fabric layers	FL	Represents number of fabric layers
Predictor	Velocity	V	Velocity of penetrator in ft/sec
Response	% Energy absorbed (exp. – Simulation)	DIF	Represents difference in % energy absorbed in experiment – simulation

The final equation of regression is:-

$$\% \text{ DIF} = - 21.9 + 3.29 \text{ FL} + 6.33 \text{ PT} - 0.0818 \text{ FL}^2 \quad (5.4)$$

This regression model has  $R^2$  of 67.9% and  $R^2$  (adj) of 59.1 %. So, over 60% variability in the model is explained by the above equation.

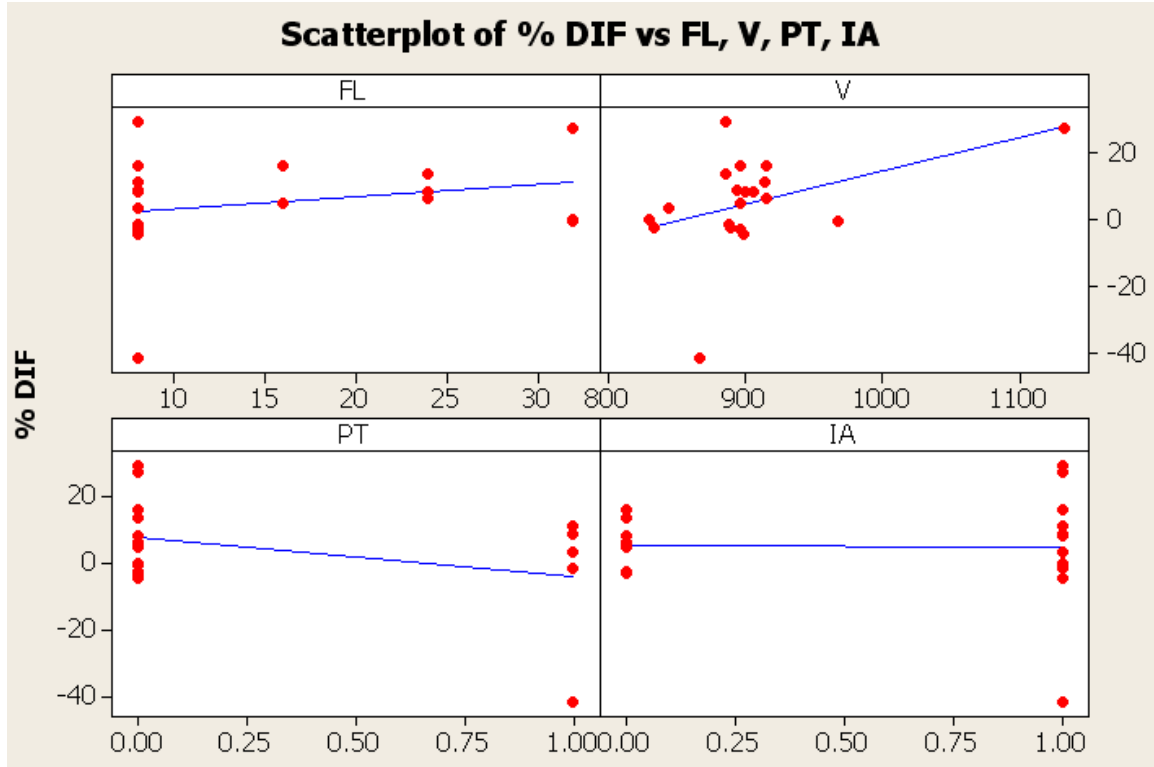


Figure 5.17. Scatter plot for multi layer model

Following observations can be made based on regression model and scatter plot of response variable against the predictor variables

- The model is mainly dominated by number of fabric layers and penetrator type.
- Most of the test cases are near 900ft/sec velocity. There is only one test case with velocity above 1000ft/sec. Initial analysis of the data revealed that this point is very influential as it has high leverage so it was removed from the model building.
- Impact angle has no effect on the difference between simulation and experimental results. So, the multi layer model works equally good for straight hit as well as oblique hit.

#### 5.4.5. Sensitivity Analysis

A sensitivity analysis of the material model was performed to determine the multi FE layer model's sensitivity to various input parameters. These parameters included the elastic moduli ( $E_{11}$  and  $E_{22}$ ), the shear moduli ( $G_{12}$ ,  $G_{23}$ , and  $G_{31}$ ), the failure strain, the coefficient of friction and the projectile orientation. For parameters that were taken from experimental results, such as  $E_{11}$  and  $E_{22}$ , the values were adjusted by -10%, -5%, +5%, and +10%. For other parameters that were assumed in the material model, such as coefficient of friction and the failure strain, lower and higher values than the assumed values were used. All the test cases were used for the sensitivity analysis.

#### Sensitivity of Material Model to $E_{11}$ and $E_{22}$

The values for  $E_{11}$  and  $E_{22}$  were adjusted by -10%, -5%, +5%, and +10% and simulations of all the test cases were run. Figures 5.20 and 5.21 show the results.

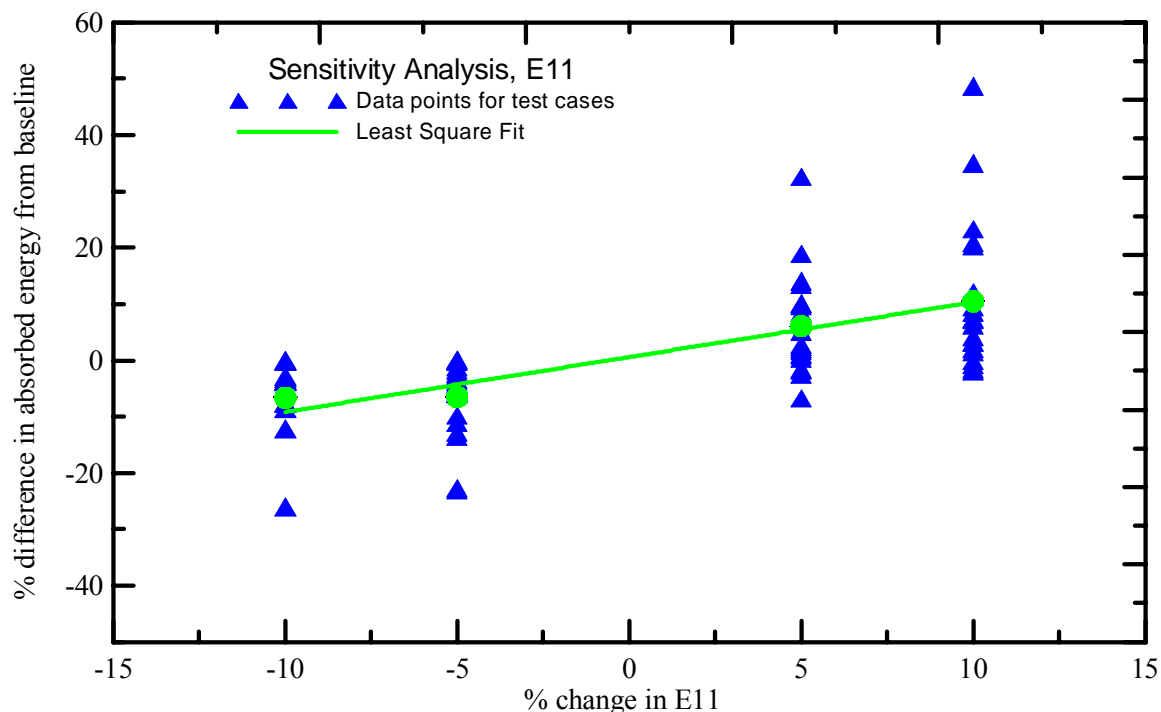


Figure 5.20. Sensitivity of material model to  $E_{11}$

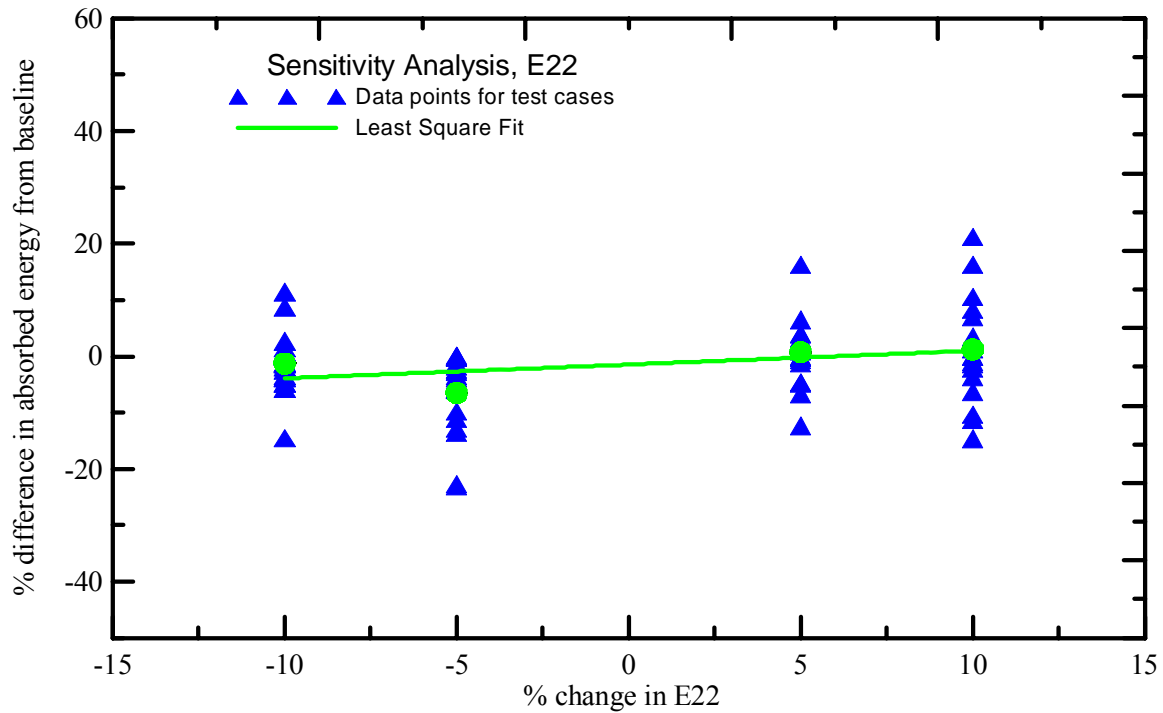


Figure 5.21. Sensitivity of material model to  $E_{22}$

#### Sensitivity of Material Model to $G_{12}$

The value for  $G_{12}$  was adjusted by -10%, -5%, +5%, and +10% and simulations of all the test cases were run. Figure 5.22 shows the results.

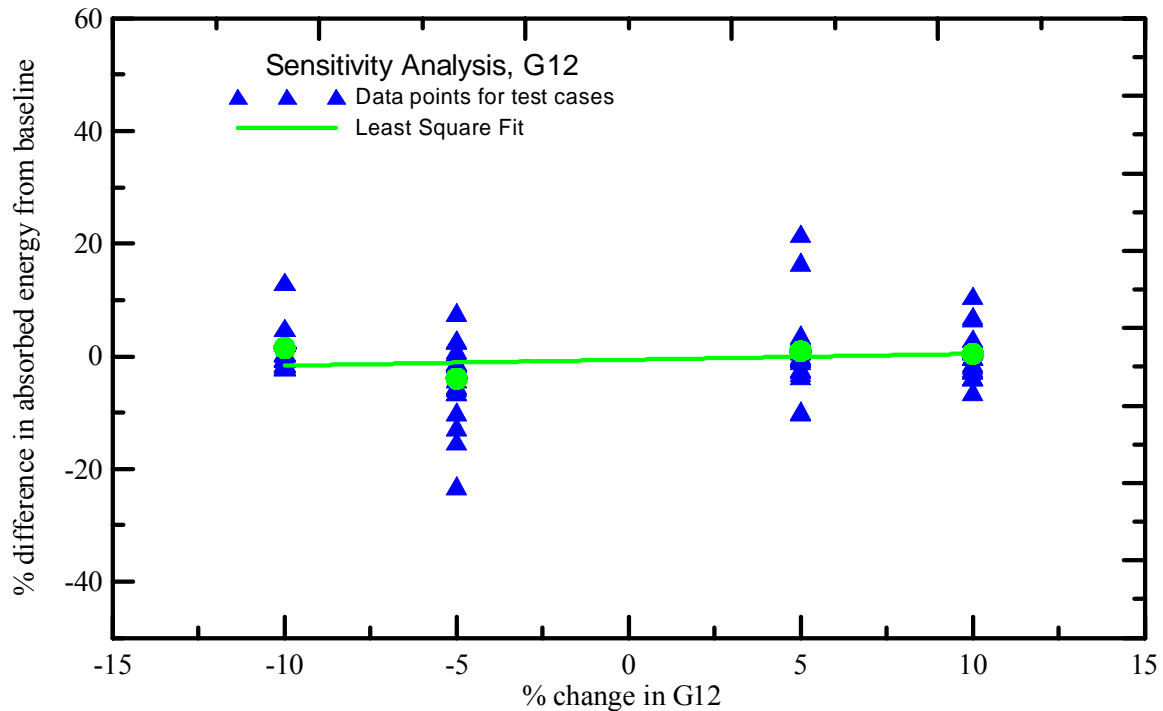


Figure 5.22. Sensitivity of material model to  $G_{12}$

#### Sensitivity of Material Model to the Coefficient of Friction

The static and dynamic coefficient of friction between fabric and fabric was used to be 0.2 while between steel and fabric was used as 0.10. Simulations of all the test cases were run using coefficient of friction between fabric layers as 0.1, 0.15 and 0.25 while coefficient of friction between fabric and steel was used as 0.05, 0.15, and 0.20. Figure 5.23 and Figure 5.24 shows the results.



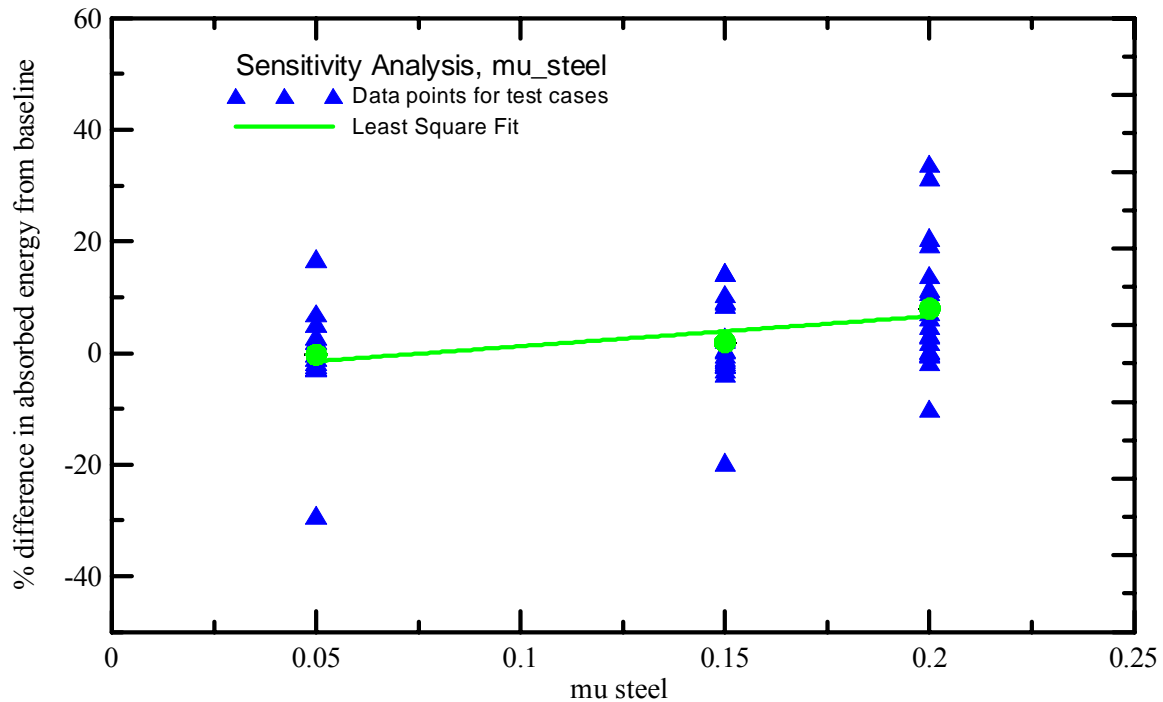


Figure 5.23. Sensitivity of material model to the coefficient of friction

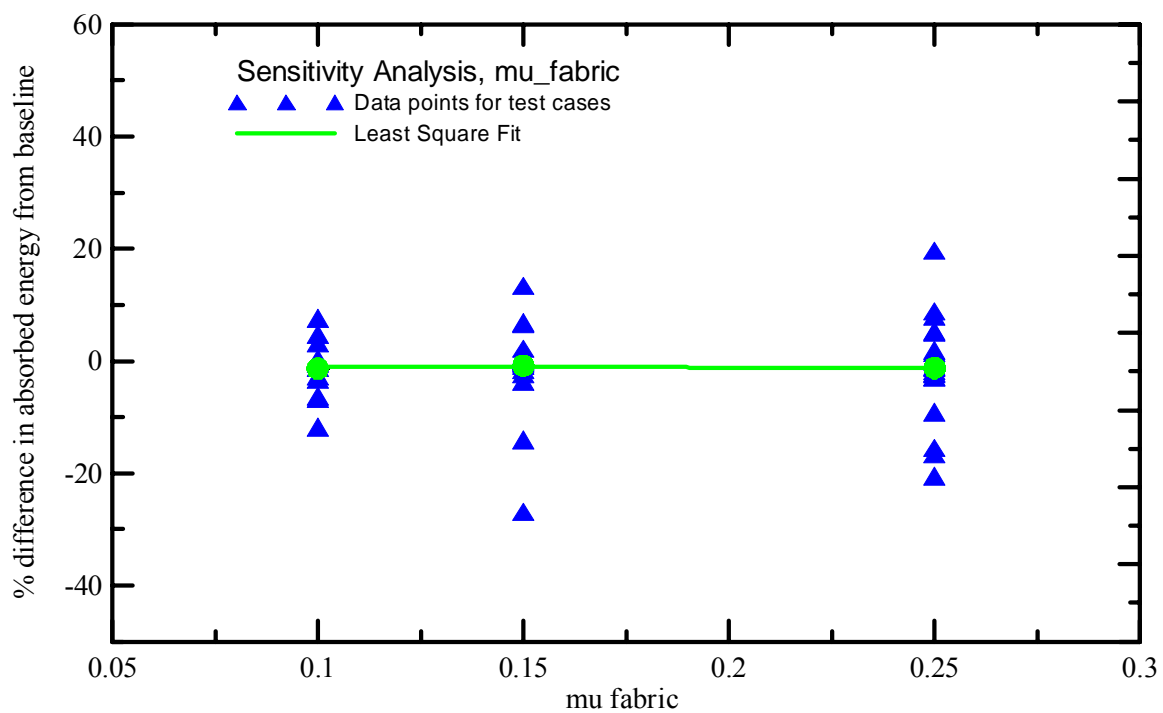


Figure 5.24. Sensitivity of material model to the coefficient of friction

### Sensitivity of Material Model to the Failure Strain

The failure strain used in the material model was 0.10 for both the warp and fill directions. Simulations of all the test cases were run using alternative values of 0.05, 0.15 and 0.2. Figure 5.25 shows the results.

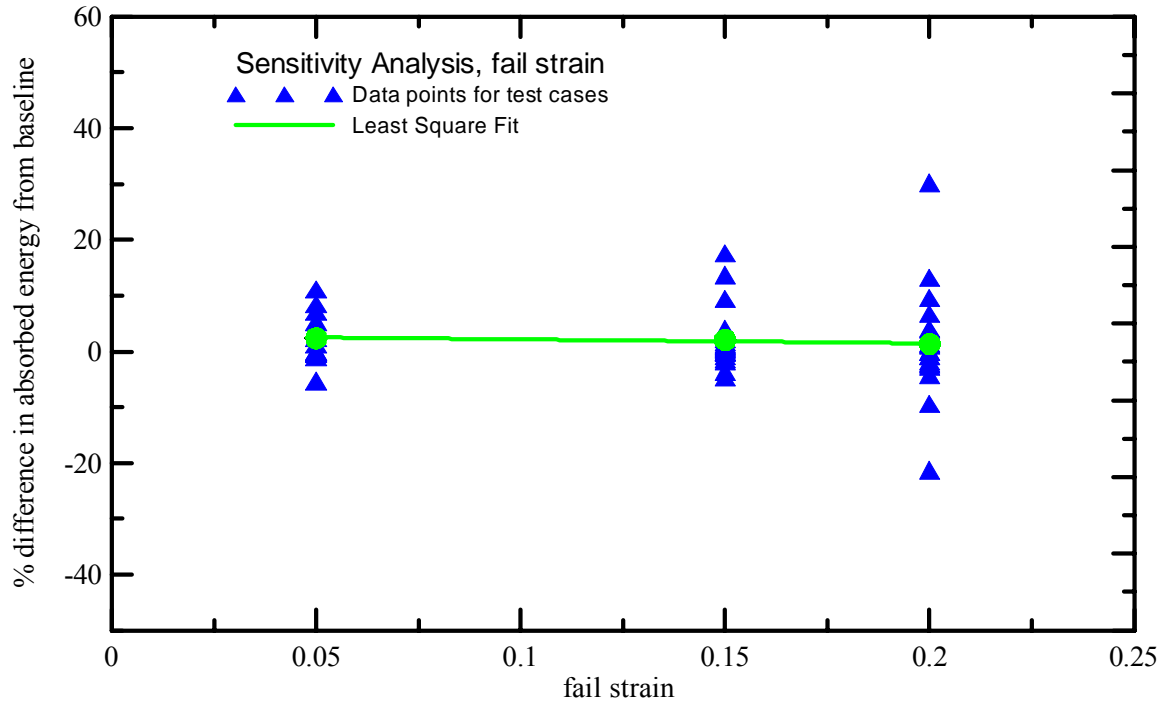


Figure 5.25. Sensitivity of material model to the fail strain

### Sensitivity of Material Model to the $G_{23}$ and $G_{31}$

The out of plane shear modulus ( $G_{23}$  and  $G_{31}$ ) used in the material model was 50,000 psi. Simulations of all the test cases were run using alternative values of 40,000 psi and 60,000 psi. Figure 5.26 shows the results.

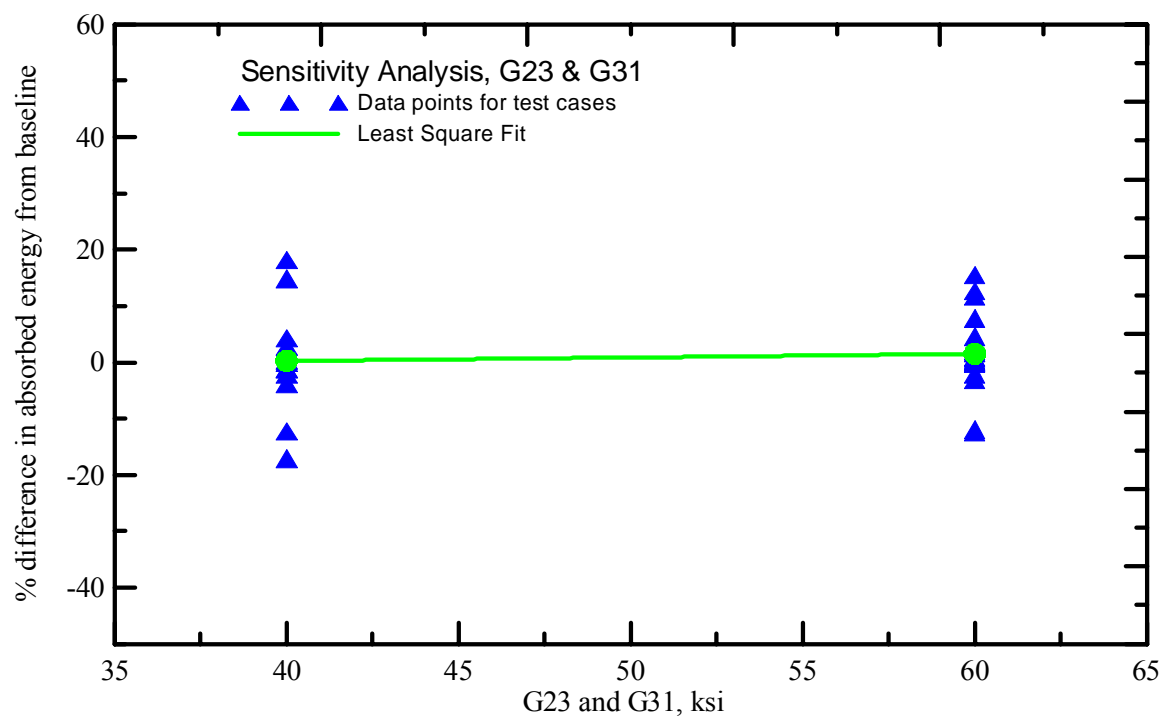


Figure 5.26. Sensitivity of material model to G23 and G31

#### Sensitivity of Material Model to the projectile orientation

The orientation of the projectile along the three axes i.e. roll, pitch and yaw were varied by +1 deg and -1 deg. Figure 5.27 to 5.29 shows the results obtained for roll, pitch and yaw sensitivity respectively.

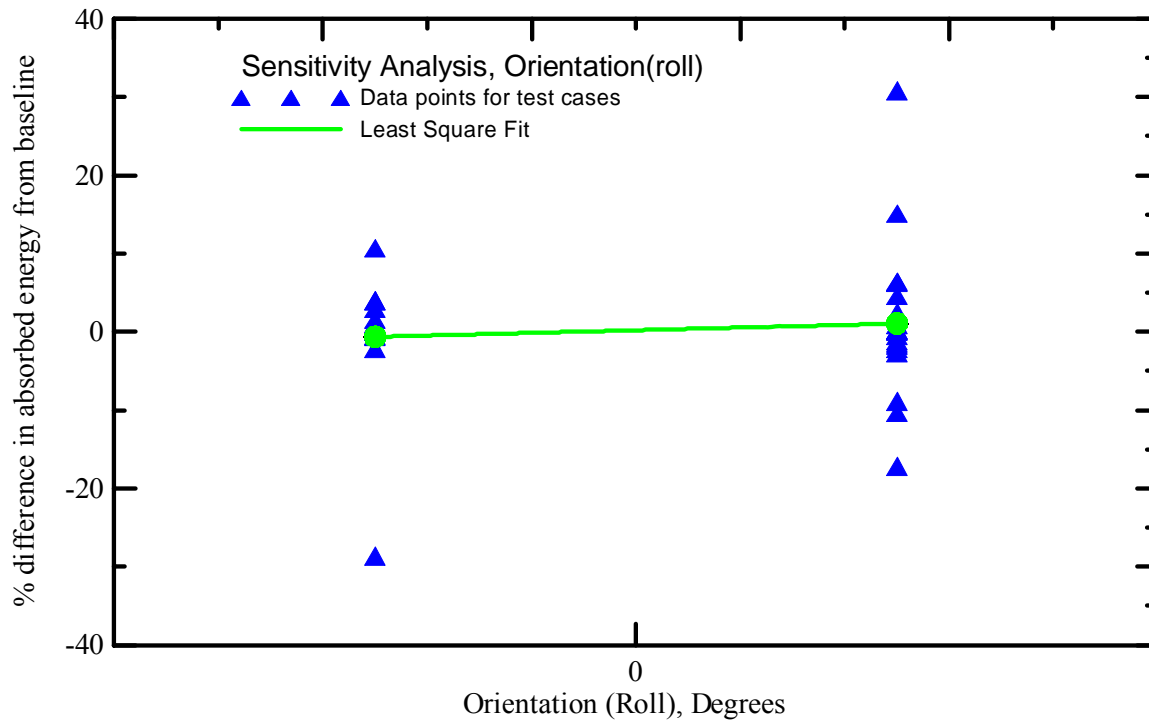


Figure 5.27. Sensitivity of material model to roll

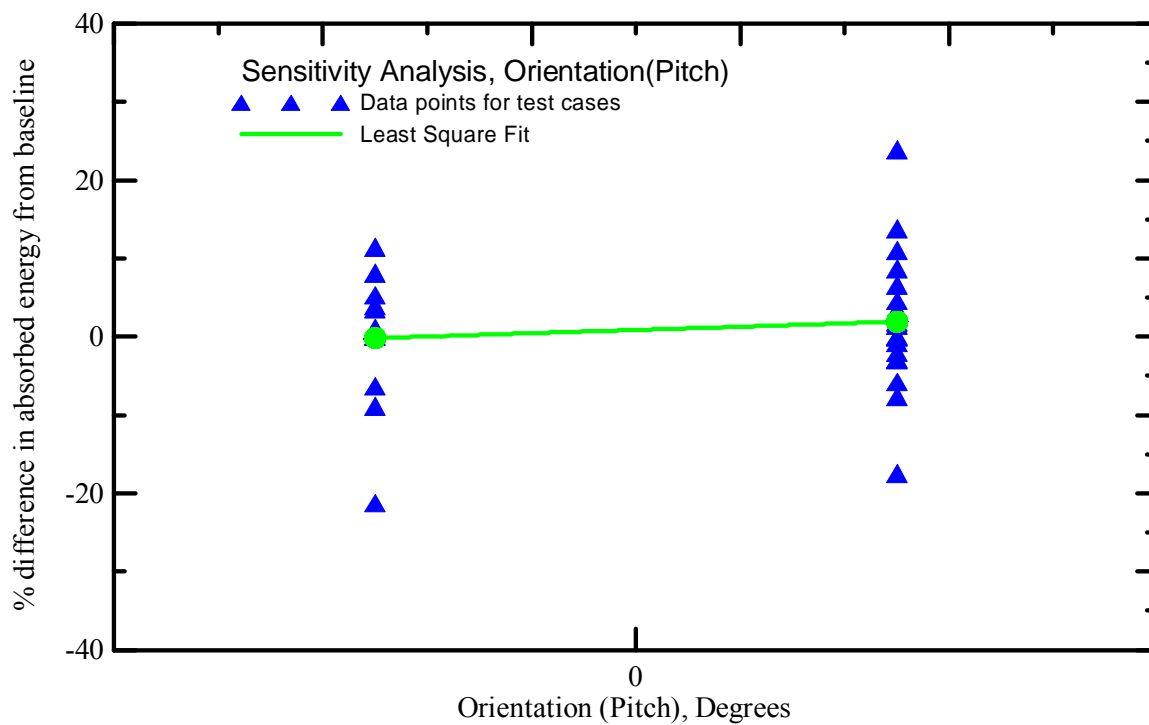


Figure 5.28. Sensitivity of material model to pitch

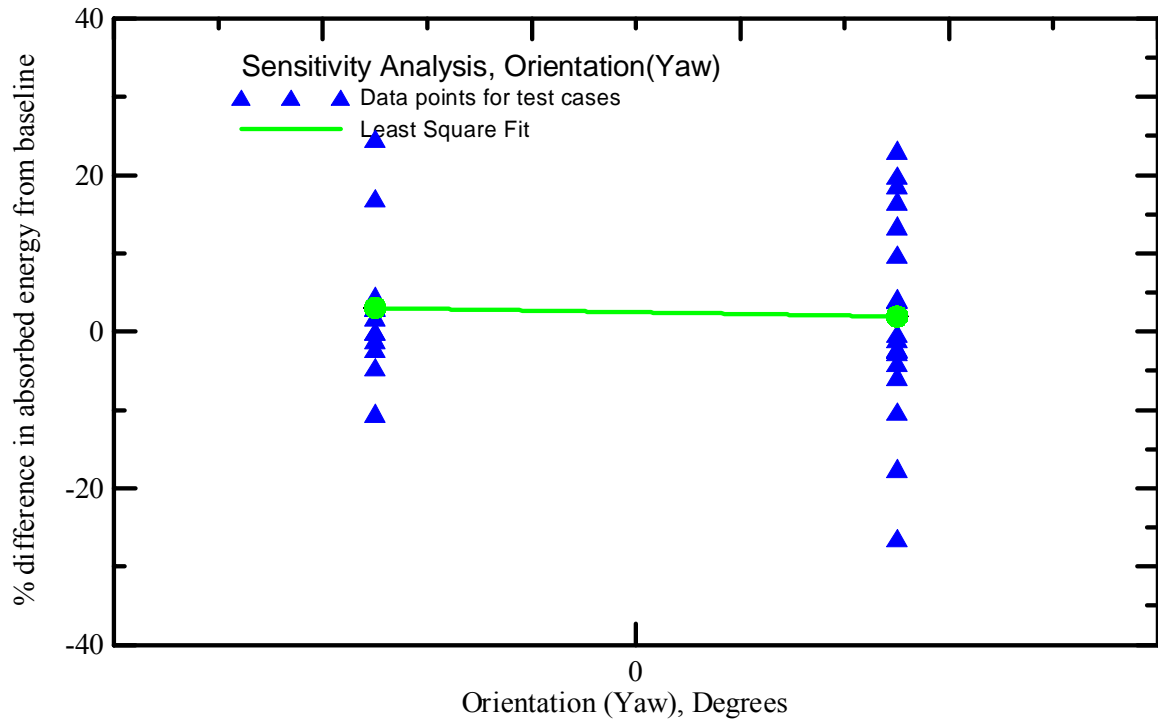


Figure 5.29. Sensitivity of material model to yaw

A ranking of the parameters from the material model's highest sensitivity to lowest sensitivity based on the sensitivity analysis and from general observations during this research is as follows:

1.  $E_{11}$
2.  $E_{22}$
3. Coefficient of Friction between steel and fabric
4.  $G_{12}$
5. Fail strain
6. Coefficient of friction between fabric and fabric
7.  $G_{23}$  and  $G_{31}$

## **6. CONCLUDING REMARKS AND FUTURE WORK**

### 6.1. Conclusion

In this research micromechanical model of Kevlar fabric was developed which is based on the experiments conducted at Arizona State University. Micromechanical model is very helpful tool in understanding the behavior of Kevlar via virtual testing. The continuum model developed in earlier research at ASU was also improved by modifying the failure criteria and verified by simulation of ballistic tests conducted at NASA-GRC. Multi FE layer ballistic test model was developed which is capable of capturing fabric layer interactions.

#### 6.1.1. Micro-mechanical Model

A methodology to build micro-mechanical model of Kevlar fabric was developed. This methodology is general enough to be used for zylon or other fabric materials. This essentially starts with approximating the Kevlar weave geometry using simple geometric shapes like ellipse and sine curves. Optical microscopy was utilized to take images of sectioned fabric potted in epoxy. A program in MATLAB is developed which can be used to digitize these images and provide estimate of parameters associated with geometric functions. Experimental procedure to perform single yarn tensile tests is developed and experiments were performed with gage length varying from 2 in to 17 in. The weibull analysis of this data clearly indicated the effect of gage length on the Kevlar yarn properties. Single yarn tensile tests were used for the estimation of young's

modulus. Other material properties were approximated based on the material geometry, experience and data available in literature. A Kevlar yarn constitutive model is developed in FORTRAN which is based on quasi-static tensile tests, implements non-linearity in the material behavior, includes strain rate effect and implements a failure criteria. This model is general enough to be used with other fabric materials. The developed constitutive model is implemented in the explicit finite element code LS-DYNA as a user-defined material definition. The developed material model is validated by comparing the finite element simulation results against results from experimental quasi-static tests.

The developed micro-mechanical model of Kevlar can be used for virtual testing and can be very helpful in understanding the Kevlar behavior under different loading conditions. The capability of this model to capture yarn to yarn interaction makes it very useful in understanding the effect of friction between yarns on behavior of fabric. The simulation results of single yarn tensile tests and swatch tensile tests are verified within the experimental error and FE solid element shortcomings.

#### 6.1.2. Continuum Model

The continuum model developed in prior research at ASU (ASUumatv1.0) was improved by modifying failure criteria (ASUumatv1.1). The material model was validated by comparing the Finite Element simulation results with experimental results. Two different modeling configurations were studied. In first configuration only one FE layer was used to represent different number of fabric layers while in second methodology one FE layer is used to represent four fabric layers. The overall results

matched with experimental tests except test cases with low velocity and less number of fabric layers.

Detailed study of experimental data vis-à-vis available videos of experiments conducted at NASA-GRC during Phase I indicated that there is discrepancy in reported projectile orientation for test cases LG 424, LG 427, LG 432, LG 434 and LG 449. It was found that in Phase I projectile orientation was not computed for any of the test case as it was done in Phase II. So, the phase I experimental data is questionable.

The simulation results from these two different continuum models showed that although both the models predicted almost equally well taking combined phase I and phase II test cases however v1.1 did better job than v1.0 if only phase II test cases were considered. The average error in energy prediction with v1.0 is 7.0% with standard deviation of 15.4% while v1.1 predicts with average error of 5.3% with standard deviation of 11.7%. The multi FE layer models also performed well. The average difference between energy absorption reported during experiment and simulation is 4.9% with standard deviation of 14.6%. The multi layer model is able to capture the frictional effect between different fabric layers and can be proved to be helpful tool in predicting optimum number of fabric layers required for particular configuration.

To check the numerical instability in the model a methodology was adopted to trace the variation of different energy values during the simulation. These checks ensured the numerical stability during the simulation.



## 6.2. Future Work

In the current multi FE layer model four fabric layer were represented by single FE layer. Although this methodology seems to be better than using single FE layer for all the fabric layers in the model there is scope of taking this model building method a step further by representing one FE layer for each fabric layer. Further, The NASA ballistic tests involved some level of rotational velocities in the projectile which was not considered in the current methodology. Since, some of the test cases are very sensitive to the projectile orientation, the rotational velocity expected to affect overall response of the material model. Finally there is need to get more test cases with spectrum of velocity range to see the effect of projectile velocity on the response.

## REFERENCES

1. ABAQUS, "Theory Manual," ABAQUS, Inc., Pawtucket RI, 2006.
2. Zack, K. S., "The development of a fabric material model for use in modeling engine containment systems," MS thesis, Arizona State University, March 2007.
3. Duan, Y., Keefe, M., Bogetti, T.A., Cheeseman, B.A., "Modeling friction effects on the ballistic impact behavior of a single-ply high-strength fabric," *International Journal of Impact Engineering*, 2005, 31 : 996-1012.
4. Cheng, M., Chen, W., Weerasooriya, T., "Experimental investigation of the transverse mechanical properties of a single Kevlar KM2 fiber," *International Journal of Solid and Structures*, 2004, 41 : 6215-6232.
5. Bala, S., "Contact Modeling in LS-DYNA", FEA information International News, 2001, 8-16.
6. Baucom, J.N., Zikry, M. A., "Evolution of failure Mechanisms in 2D and 3D woven composite systems under quasi-static perforation," *Journal of composite materials*, 2003, 37: 1651-1674.
7. Arizona State University, "FAA development of reliable modeling methodologies for fan blade out analysis: Friction Tests," unpublished, November 2004.
8. Arizona State University, "FAA development of reliable modeling methodologies for fan blade out analysis: Shear modulus test using picture frame tests," unpublished, 2005.
9. Barbero, E.J., Lonetti, P., and Sikkil, K.K., "Finite element continuum damage modeling of plain weave reinforced composites," *Comp Part B* 2006, 37: 137-47.
10. Barbero, E.J., et al., "Finite element modeling of plain weave fabrics from photomicrograph measurements," *J Comp Stru* 2006, 73(1): 41-52.
11. Belytschko, T., and Hughes, T.J.R., *Computational Methods for Transient Analysis*, Elsevier Science Publishing Company, New York, New York, 1983.
12. Belytschko, T., Liu, W. K. and Moran, B., *Nonlinear Finite Elements for Continua and Structures*, J. Wiley and Sons, New York, New York, 2000.
13. Cheng, M., Chen, W., and Weerasooriya, T., "Mechanical properties of Kevlar KM2 single fiber," *J Engng Mat Tech* 2005, 127(2): 197-203.

14. Gu, B., "Analytical modeling for the ballistic perforation of planar plain-woven fabric target by projectile," *Comp Part B* 2003, 34: 361-71.
15. Iannucci, L., and Willows, M.L., "An energy based damage mechanics approach to modeling impact onto woven composite materials-Part I: Numerical models," *Comp Part A* 2006, 37(11): 2041-56.
16. Iannucci, L., and Willows, M.L., "An energy based damage mechanics approach to modeling impact onto woven composite materials-Part II: Experimental and numerical results," *Comp Part A* 2007, 38(2): 540-54.
17. Ishikawa, T., and Chou, T.W., "Stiffness and strength behavior of woven fabric composites," *J Compos Mater* 1982, 17:3211-220.
18. Ishikawa, T., and Chou, T.W., "Elastic behavior of woven hybrid composites," *J Compos Mater* 1982, 16:2-19.
19. Ishikawa, T., and Chou, T.W., "One-dimensional micromechanical analysis of woven fabric composites," *AIAA Jr* 1983, 21(12):1714-21.
20. Zhou, Y., Jiang, D., Xia, Y., "Tensile mechanical behaviour of T300 and M40J fiber bundles at different strain rate," *Journal of material science*, 2001, 919-922.
21. Zhang, Y., Wang, X., "Weibull analysis of the tensile behavior of fibers with geometrical irregularities", *Journal of material science*, 2002, 1401-1406.
22. Jiang, Y., Tabiei, A., and Simitzes, G.J., "A novel micromechanics-based approach to the derivation of constitutive equations for local/global analysis of plain-weave fabric composite," *J Compos Sci Tech* 2000, 60: 1825-33.
23. Johnson, A.F., and Simon, J., "Modeling fabric reinforced composites under impact loads," *EUROMECH 400: Impact and Damage Tolerance Modeling of Composite Materials and Structures Imperial College of Science Technology and Medicine*, London, 1999.
24. Kollegal, G.M., and Sridharan, S., "Strength prediction of plain woven fabrics," *J Compos Mater* 2000, 34(3): 240-57.
25. Kollegal, M., Chatterjee, S.N., and Flanagan, G., "Progressive failure analysis of plain weaves using damage mechanics based constitutive laws," *J Damage Mech* 2001, 10:301-23.

26. Krishnan, K., "Using Virtual Testing for Topology Optimization", M.S. Thesis, Department of Civil & Environmental Engineering, Arizona State University, May 2007.
27. Lim, C.T., Shim, V.P.W., and Ng, Y.H., "Finite-element modeling of the ballistic impact of fabric armor," *Int J Impact Engng* 2003, 28: 13-31.
28. LS-DYNA, "Theoretical Manual," Livermore Software Technology Corp., Livermore CA, 1998.
29. LS-DYNA, "Keyword User's Manual: Version 971," Livermore Software Technology Corp., Livermore CA, 2003.
30. Naik, N.K., and Ganesh, V.K., "Failure behavior of plain weave fabric laminates under on-axis uniaxial tensile loading: I-Laminate geometry," *J Compos Mater* 1996, 30(16): 1748-78.
31. Naik, N.K., and Ganesh, V.K., "Failure behavior of plain weave fabric laminates under on-axis uniaxial tensile loading: II-Analytical predictions," *J Compos Mater* 1996, 30(16): 1779-1822.
32. Naik, N.K., and Ganesh, V.K., "Failure behavior of plain weave fabric laminates under on-axis uniaxial tensile loading: III-Effect of fabric geometry," *J Compos Mater* 1996, 30(16): 1823-1856.
33. Peng, X.Q., and Cao, J., "Numerical determination of mechanical elastic constants of textile composites," 15<sup>th</sup> Annual Technical Conference of the American Society for Composites, College Station, TX, 2000.
34. Rodriguez, J., et al., "High strain rate properties of aramid and polyethylene woven fabric composites," *Comp Part B* 1996, 27B: 147-54.
35. Roylance, D., et al., "Numerical modeling of fabric impact," Proceedings of the National Meeting of the American Society of Mechanical Engineers (ASME), San Francisco, CA, 1995.
36. Scida, D., et al, "A micromechanics model for 3D elasticity and failure of woven-fibre composite materials," *J Compos Sci Tech* 1999, 59:505-17.
37. Sharda, J., "Experimental methods and numerical simulation of fabrics for engine containment systems," M.S. Thesis, Department of Civil Engineering, Arizona State University, August 2002.

38. Shim, V.P.W., Tan, V.B.C., and Tay, T.E., "Modeling deformation and damage characteristics of woven fabric under small projectile impact," *Int J Impact Engng* 1995, 16(4): 585-605.
39. Shim, V.P.W., Lim, C.T., and Foo, K.J., "Dynamic mechanical properties of fabric armour," *Int J Impact Engng* 2001, 25: 1-15.
40. Söderberg, A., and Sellgren, U., "Modeling of strain hardening and strain rate hardening of dual phase steels in finite element analysis of energy-absorbing components," NAFEMS World Congress 2005, No. 69.
41. Srirengan, K., Whitcomb, J., and Chapman, C., "Modal technique for three-dimensional global/local stress analysis of plain weave composites," *J Comp Stru* 1997, 39: 145-56.
42. Tabiei, A., and Jiang, Y., "Woven fabric composite material model with material nonlinearity for nonlinear finite element simulation," *J Solids Structures* 1999, 36: 2757-71.
43. Tabiei, A., and Yi, W., "Comparative study of predictive methods for woven fabric composite elastic properties," *J Comp Stru* 2002, 58: 149-64.
44. Tabiei, A., and Ivanov, I., "Computational micro-mechanical model of flexible woven fabric for finite element impact simulation," 7<sup>th</sup> International LS-DYNA Users Conference, 2002, 8-15-8-40.
45. Tanov, R., and Tabiei, A., "Computationally efficient micro-mechanical woven fabric constitutive," *J Models Appl Mech* 2001, 68(4): 553-60.
46. Vandeurzen, Ph., Ivens, J., and Verpoest, I., "A three-dimensional micromechanical analysis of woven-fabric composites: I. Geometric analysis," *J Compos Sci Tech* 1996, 56: 1303-15.
47. Vandeurzen, Ph., Ivens, J., and Verpoest, I., "A three-dimensional micromechanical analysis of woven-fabric composites: II. Elastic analysis," *J Compos Sci Tech* 1996, 56: 1317-27.
48. Xia, Y., and Wang, Y., "The effects of strain rate on the mechanical behavior of Kevlar fibre bundles: an experimental and theoretical study," *Comp Part A* 1998, 29A: 1411-15.
49. Xia, Y., Wang, Y., "Experimental and theoretical study on the strain rate and temperature dependence of mechanical behavior of Kevlar fibre," *Comp Part A* 1999, 30: 1251-57.

50. Xue, P., Xiongqi, P., and Cao, J., "A non-orthogonal constitutive model for characterizing woven composites," *Comp Part A* 2003, 34: 183-93.
51. Mattiassan, K., Barnspang, L., Samuelsson, A., "Solution of quasi-static, force-driven problems by means of a dynamic-explicit approach and an adaptive loading procedure," *Engineering computations*, vol.13, 1996.
52. Chung, W.J., Cho, J.W., Belytschko, T., "On the dynamic effects of explicit FEM in sheet metal forming analysis", *Engineering Computations*, Vol 15 No. 6, 1998 pp 750-776.
53. Santosa, S.P., Wierzbicki, T., Hanssen, A.G., Langseth, M., "Experimental and numerical studies of foam-filled sections", *International journal of impact engineering* 24, 2000, 509-534.
54. Kim, J., Kang, S.J., Kang, B.S., "A comparative study of implicit and explicit FEM for the wrinkling prediction in the hydroforming process", *International journal of advanced manufacturing technology*, 2003, 22: 547-552.
55. Amaniampong, G., Burgoyne, C.J., "Statistical variability in the strength and failure strain of aramid and polyester yarns", *Journal of materials science*, 1994, 29 : 5141-5152.

## **APPENDIX A**

**KEVLAR® 49 YARN MATERIAL CONSTANTS USED IN MATERIAL MODEL**

Table A.1. Kevlar® 49 material constants used in material model

Material Constant	UMAT Notation	Symbol	Value
Longitudinal Stiffness in Elastic Region (psi 10 <sup>6</sup> )	Ex	$E_{11}$	7.43
Transverse Stiffness in Elastic Region (psi 10 <sup>6</sup> )	Ey	$E_{22}$	0.037
Transverse Stiffness in Elastic Region (psi 10 <sup>6</sup> )	Ez	$E_{33}$	0.037
Crimp Stiffness Factor	Ecrfac	$E^{crp}$	0.0
Post-peak Linear Region Stiffness Factor	Esoftfac	$E^{soft}$	-3.5
Unloading/Reloading Stiffness Factor	Eunlfac	$E^{unl}$	1.0
Compressive Stiffness Factor	Ecompfac	$E^{comp}$	0.005
Shear Stiffness ( $G_{23}$ ) (psi 10 <sup>6</sup> )	Gyz	$G_{23}$	0.05
Shear Stiffness ( $G_{31}$ ) (psi 10 <sup>6</sup> )	Gzx	$G_{31}$	3.48
Shear Stiffness ( $G_{12}$ ) (psi 10 <sup>6</sup> )	Gxy	$G_{12}$	3.48
Poission's ratio in xy plane	pratioxy	$\nu_{12}$	0.0
Poission's ratio in yz plane	pratioyz	$\nu_{23}$	0.0
Poission's ratio in zx plane	pratiozx	$\nu_{31}$	0.0
Crimp Strain (in/in)	ecrpx	$\varepsilon_{11}^{crp}$	0.0
Strain at Peak Stress (in/in)	emaxx	$\varepsilon_{11}^{\max}$	0.024
Stress at Post-peak Non-linearity (psi 10 <sup>6</sup> )	sigpost	$\sigma^*$	0.02
Failure Strain (in/in)	efailx	$\varepsilon_{11}^{fail}$	0.20
Cowper-Symonds Factor for Stiffness (ms <sup>-1</sup> )	C(E)	$C_E$	0.005
Cowper-Symonds Factor for Stiffness (ms <sup>-1</sup> )	P(E)	$P_E$	40.0
Cowper-Symonds Factor for Strain (ms <sup>-1</sup> )	C(e)	$C_\varepsilon$	0.005
Cowper-Symonds Factor for Strain (ms <sup>-1</sup> )	P(e)	$P_\varepsilon$	40.0
Post-peak Non-linear Region Factor	dfac	$dfac$	0.20



**APPENDIX B**

FLOW DIAGRAM AND GENERAL ALGORITHM FOR SUBROUTINE

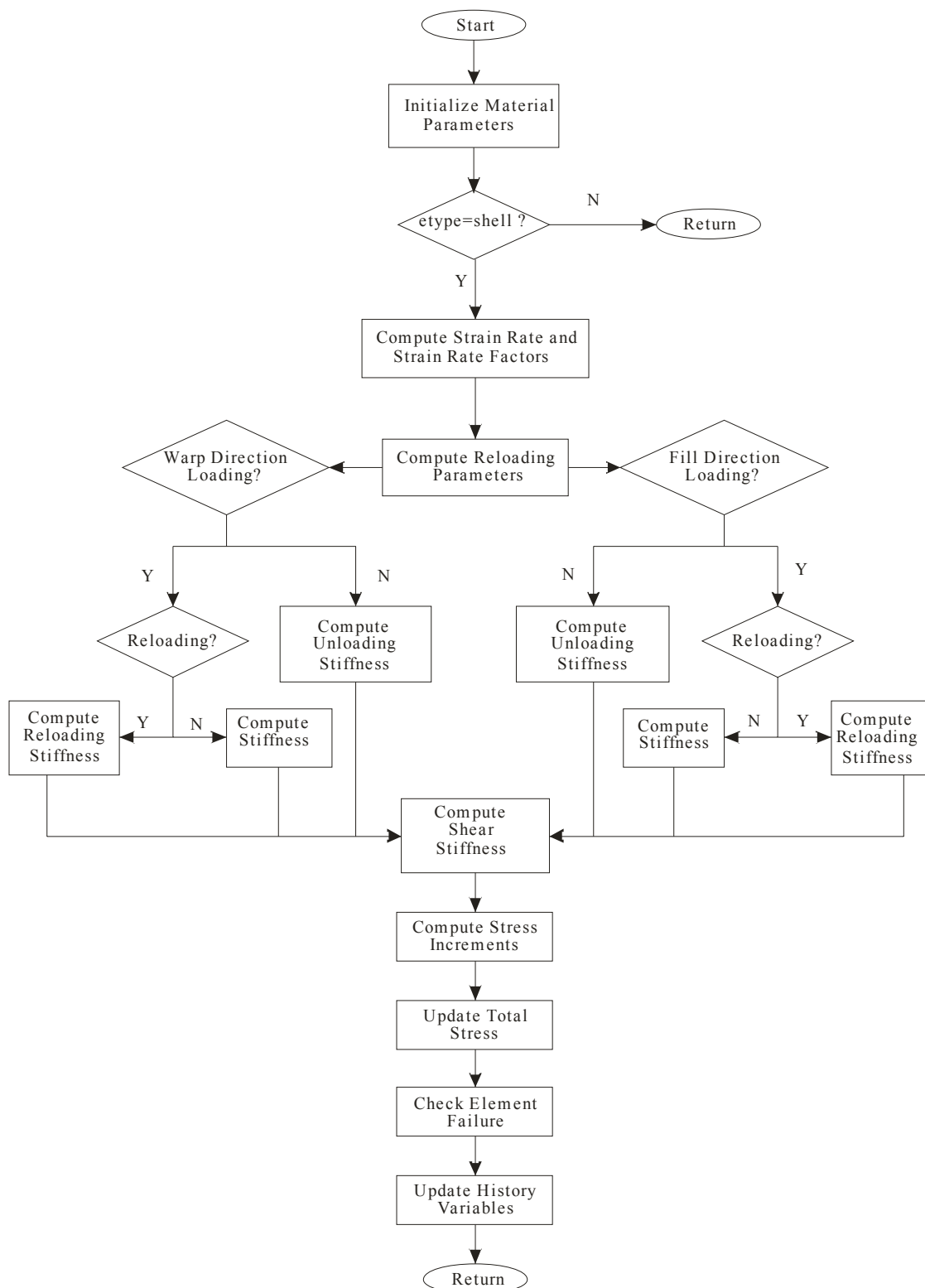


Figure B.1. Flow diagram for UMAT subroutine

## General Algorithm

### Step 1. Obtaining Material Parameters, Previous Step Data, and Current Step Data

In this step the material parameters are obtained from the material card specified in the LS-DYNA input deck. Also, other parameters which are passed to the UMAT such as the current strain increment, the previous total stress, and history variables are obtained. Any additional parameters which are required in the subroutine are computed. The current strain is also computed in this step.

### Step 2. Strain Rate Computations

The current strain rate in both material directions is estimated as

$$\dot{\epsilon}_{11} = \frac{\epsilon_{11}^t - \epsilon_{11}^{t-\Delta t}}{\Delta t} \quad (\text{B.1})$$

$$\dot{\epsilon}_{22} = \frac{\epsilon_{22}^t - \epsilon_{22}^{t-\Delta t}}{\Delta t} \quad (\text{B.2})$$

where  $\epsilon^t$  is the strain at the current time step in each respective direction,  $\epsilon^{t-\Delta t}$  is the strain at the previous time step in each respective direction, and  $\Delta t$  is the current time increment.

The adjusted elastic stiffness values and strain to peak stress values are then computed as

$$E_{11}^{adj} = E_{11} \left( 1 + \frac{\dot{\epsilon}_{11}}{C_E} \right)^{\frac{1}{P_E}} \quad (\text{B.3})$$

$$E_{22}^{adj} = E_{22} \left( 1 + \frac{\dot{\epsilon}_{22}}{C_E} \right)^{\frac{1}{P_E}} \quad (\text{B.4})$$

$$\varepsilon_{11}^{\max(adj)} = \varepsilon_{11}^{\max} \left( 1 + \frac{\dot{\varepsilon}_{11}^{\max}}{C_{\varepsilon}} \right)^{\frac{1}{P_{\varepsilon}}} \quad (B.5)$$

$$\varepsilon_{22}^{\max(adj)} = \varepsilon_{22}^{\max} \left( 1 + \frac{\dot{\varepsilon}_{22}^{\max}}{C_{\varepsilon}} \right)^{\frac{1}{P_{\varepsilon}}} \quad (B.6)$$

where  $E$  is the static elastic stiffness in each respective direction,  $E^{adj}$  is the adjusted elastic stiffness in each respective direction,  $\dot{\varepsilon}$  is the strain rate in each respective direction,  $\dot{\varepsilon}^{\max}$  is the maximum strain rate experienced by the element in each respective direction, and  $C_E$ ,  $P_E$ ,  $C_{\varepsilon}$ ,  $P_{\varepsilon}$  are Cowper-Symonds  $C$  and  $P$  factors describing the strain rate effects on the material properties.

### Step 3. Compute Reloading Parameters

In this step reloading strain values are computed. These values are required so if the element integration point had previously unloaded during its history the subroutine can track the strain value where unloading had begun.

### Step 4. Compute the Stiffness in the Warp Direction

In this step the stiffness value  $E_{11}$  is determined based on the stress-strain history, the current strain increment, the total strain, and the strain rate.

#### Step 4.1. Check for Loading/Unloading

If strain increment is positive – loading, go to Step 4.1.1.a. Else strain increment is negative – unloading, go to Step 4.1.1.b.

Step 4.1.1.a. Determine Which Region Element Integration Point Is In

crimp region?, elastic region?, post-peak linear region?, post-peak non-linear region?, reloading? transitioning? Compute the appropriate stiffness value ( $E_{11}$ )

Step 4.1.1.b. Determine Which Region Element Integration Point Is In

Unloading region? compression region? transitioning? Compute the appropriate stiffness value ( $E_{11}$ )

Step 5. Compute the Stiffness in the Fill Direction

In this step the stiffness value  $E_{22}$  is determined based on the stress-strain history, the current strain increment, the total strain, and the strain rate.

Step 5.1. Check for Loading/Unloading

If strain increment is positive – loading, go to Step 5.1.1.a. Else strain increment is negative – unloading, go to Step 5.1.1.b.

Step 5.1.1.a. Determine Which Region Element Integration Point Is In

crimp region?, elastic region?, post-peak linear region?, post-peak non-linear region?, reloading? transitioning? Compute the appropriate stiffness value ( $E_{22}$ )

Step 5.1.1.b. Determine Which Region Element Integration Point Is In

Unloading region? compression region? transitioning? Compute the appropriate stiffness value ( $E_{22}$ )

### Step 6. Compute the Shear Stiffness ( $G_{12}$ )

In this step the shear stiffness value ( $G_{12}$ ) is determined based on the current engineering shear strain ( $\gamma_{12}$ ).

$$\text{If } |\gamma_{12}| < 0.35 \quad G_{12} = 1(10^3) \text{ psi} \quad (\text{B.7})$$

$$\text{Else If } 0.35 < |\gamma_{12}| < 0.50 \quad G_{12} = 8(10^3) \text{ psi} \quad (\text{B.8})$$

$$\text{Else If } 0.50 < |\gamma_{12}| < 0.57 \quad G_{12} = 40(10^3) \text{ psi} \quad (\text{B.9})$$

$$\text{Else If } |\gamma_{12}| > 0.57 \quad G_{12} = 300(10^3) \text{ psi} \quad (\text{B.10})$$

### Step 7. Compute the Stress Increments

$$\Delta\sigma_{11} = \Delta\varepsilon_{11}E_{11} \quad (\text{B.11})$$

$$\Delta\sigma_{22} = \Delta\varepsilon_{22}E_{22} \quad (\text{B.12})$$

$$\Delta\sigma_{33} = 0.0 \quad (\text{B.13})$$

$$\Delta\sigma_{12} = \Delta\gamma_{12}G_{12} \quad (\text{B.14})$$

$$\Delta\sigma_{23} = \Delta\gamma_{23}G_{23} \quad (\text{B.15})$$

$$\Delta\sigma_{31} = \Delta\gamma_{31}G_{31} \quad (\text{B.16})$$

### Step 8. Update the Total Stress

$$\sigma_{11} = \sigma_{11}^{old} + \Delta\sigma_{11} \quad (\text{B.17})$$

$$\sigma_{22} = \sigma_{22}^{old} + \Delta\sigma_{22} \quad (\text{B.18})$$

$$\sigma_{33} = \sigma_{33}^{old} + \Delta\sigma_{33} \quad (\text{B.19})$$

$$\sigma_{12} = \sigma_{12}^{old} + \Delta\sigma_{12} \quad (\text{B.20})$$

$$\sigma_{23} = \sigma_{23}^{old} + \Delta\sigma_{23} \quad (\text{B.21})$$

$$\sigma_{31} = \sigma_{31}^{old} + \Delta\sigma_{31} \quad (\text{B.22})$$

#### Step 9. Check Element Failure

In this step element failure is checked. If the current strain in the warp or fill directions (11 and 22) is greater than the failure strain the element has failed. Set failure indicator to specify element deletion.

#### Step 10. Update History Variables

In this step any history variables which are required in the next step are updated. These include the current total strains, the current strain increments, the reloading strains, and the current strains to peak stress.

#### Step 11. End Subroutine